

Densification of zirconia-based anti-corrosion coatings for application in waste-to-energy plants

Dissertation

der Fakultät für Geowissenschaften

der Ludwig-Maximilians-Universität München

zur Erlangung des akademischen Grades

doctor rerum naturalium

(Dr. rer. nat.)

Vorgelegt von

Dirk Müller

München, 14.09.2016

1. Gutachter: Professor Dr. Soraya Heuss-Aßbichler
(Ludwig-Maximilians-Universität München)
2. Gutachter: Professor Dr. Klaus G. Nickel
(Eberhard Karls Universität Tübingen)

Datum der Disputation: 06.02.2017

“The future holds the power for dreams.”

Schiller

Summary

Corrosion of functional parts (e.g. boiler tubes) within waste-to-energy (WTE) plants significantly reduces their efficiency with respect to maintenance costs. Currently, nickel-based alloy claddings, several millimeters thick, are the state of the art as anti-corrosion coating. Another approach is to utilize thermally sprayed multilayer coatings with a zirconia-based top-coat, e.g. yttria-stabilized zirconia (YSZ). Lab-scale experiments and in-situ tests within a WTE plant were conducted by using a multilayer coating of a nickel-based bond-coat and an YSZ top-coat, applied onto a steel substrate. For lab-scale experiments WTE plant operation conditions were simulated within a tube furnace through an atmosphere of $\text{N}_2\text{-HCl-O}_2$, enriched with additional volatile gas phases emerging out of an equimolar $\text{KCl-K}_2\text{SO}_4\text{-ZnCl}_2\text{-ZnSO}_4$ salt mixture, which was placed beneath the sample in the high temperature zone of the furnace at 500 - 700 °C. Under an atmosphere composition of N_2 - 2.1 vol.-% HCl - 0.9 vol.-% O_2 , a partially reduced porosity of the zirconia top-coat can be achieved, where former pores are filled up with zirconia. The addition of ZrO_2 powder into the salts and the use of additional sodium salts enhance the densification of the zirconia top-coat. The zirconia top-coat of the in-situ experiments at 450 °C and 700 °C also show a partial densification, whereas the pores are filled up with newly formed metal (chromium, nickel, iron) oxides. Since the formation of low-melting eutectic salt melts on the surface of those boiler tubes is a common process within WTE plants, the performance of YSZ under these conditions was evaluated, too. Multilayer-coated samples were impregnated by a salt solution and heat treated under various mixtures of argon, nitrogen, gaseous hydrochloric acid, sulfur dioxide and / or oxygen at 700 °C. No densification was observable, but an element migration of mainly iron from the steel substrate into the coating and nickel and chromium from the bond-coat into the steel. Furthermore, YSZ beads were embedded in an equimolar mixture of $\text{KCl-K}_2\text{SO}_4\text{-ZnCl}_2\text{-ZnSO}_4$. At temperatures of 600 °C and 700 °C under an atmosphere of N_2 - 2.55 vol.-% HCl - 0.45 vol.-% O_2 , a dissolution and recrystallization of the zirconia was observed. Both processes, the densification of the zirconia top-coat after a heat treatment under an HCl-O_2 -bearing atmosphere and the ability of a zirconia recrystallization within salt melts enables the zirconia-based coating to act as a barrier against aggressive gases, hence, to represent a possible anti-corrosion coating for steel tubes within WTE plants.

Content

Summary	1
Copyright information	3
1 Introduction	5
1.1 History of waste incineration	6
1.2 Layout of waste-to-energy plants	7
1.3 Corrosion in waste-to-energy plants	7
1.3.1 Corrosion phenomena	9
1.3.1.1 Active oxidation	10
1.3.1.2 Hot corrosion	12
1.4 Corrosion protection	13
2 Corrosion of zirconia ceramics	15
2.1 Zirconia under chlorine-bearing atmospheres	15
2.2 Zirconia under aggressive melts	16
2.3 Corrosion prevention by densification of thermally sprayed zirconia coatings – state of the art	19
3 Experimental	21
3.1 Samples	21
3.1.1 Gas phase and gas phase – salt melt experiments	21
3.1.2 Salt melt experiments	22
3.1.3 Waste-to-energy plant test probes	22
3.2 Experimental setup for lab-scale experiments	24
3.2.1 Gas phase experiments	24
3.2.2 Combined gas phase and salt melt experiments	24
3.2.3 Salt melt experiments	24
3.3 In-situ test facility	29
3.4 Sample preparation and analytical methods	31
3.4.1 Sample preparation for electron-probe micro-analyses (EPMA)	31
3.4.2 Electron-probe micro-analyzer (EPMA)	31
3.4.3 X-ray diffraction (XRD)	31
3.4.4 X-ray fluorescence (XRF)	32
3.4.5 Raman spectroscopy	32
3.4.6 Fourier transformed infrared (FT-IR) spectroscopy	32

3.4.7	Weighing	32
3.4.8	Inductively coupled plasma optical emission spectrometry (ICP-OES)	32
4	Results and discussion of lab-scale experiments	33
4.1	Gas phase experiments	33
4.1.1	Experiments with the old experimental setup	36
4.1.2	Experiments with the new experimental setup	41
4.2	Combined gas phase and salt melt experiments	51
4.3	Proposed densification process in gas phase experiments	61
4.4	Salt melt experiments	63
4.4.1	Dissolution and recrystallization phenomena	63
4.4.1.1	Investigation of the beads	63
4.4.1.2	Investigation of the residual powder	67
4.4.1.3	Investigation of the residual salt melt	69
4.5	Proposed dissolution and recrystallization process in salt melt experiments	71
5	In-situ tests	75
5.1	In-situ test of an uncooled test probe at 700 °C	75
5.2	In-situ test of a cooled test probe at 450 °C	78
5.3	Discussion of in-situ tests	79
6	Conclusion	81
7	Outlook	83
	References	85
	Figures	95
	Tables	97
	Acknowledgment	99
	Curriculum Vitae	Fehler! Textmarke nicht definiert.
	Declaration of authorship	101

Copyright information

Parts of this dissertation are based on publications and MSc theses that were done in the framework of the research project “TS-Protect”. The following list gives an overview of the work incorporated in this dissertation, including the contribution of the co-authors.

Peer-reviewed publications:

Müller, D. & Heuss-Aßbichler, S., 2016. Behavior of yttria-stabilized zirconia in the presence of molten salts: Part 1 - Dissolution and recrystallization phenomena, *Journal of the European Ceramic Society*, 36, 3495-3503.

Soraya Heuss-Aßbichler: Discussion and interpretation of the experimental results.

Müller, D., Wöllmer, S., Aßbichler, D., Murer, M. J., Heuss-Aßbichler, S., Rieger, K., Hill, H., Härtel, C. & Masset, P. J., 2016. High temperature corrosion studies of a zirconia coating: Implications for waste-to-energy (WTE) plants, *Coatings*, 6, 36.

Silke Wöllmer: Preparation of lab-scale experiment samples and in-situ test probes. Performance of in-situ experiments. Discussion and interpretation of the experimental results.

Donja Aßbichler: Performance of XRF analysis. Discussion and interpretation of the experimental results.

Martin J. Murer & Konrad Rieger: Layout of and conditions within a waste-to-energy plant. Discussion and interpretation of the experimental results.

Soraya Heuss-Aßbichler: Discussion and interpretation of the experimental results.

Horst Hill & Carsten Härtel: Material composition and characteristics.

Patrick J. Masset: Discussion and interpretation of the experimental results.

MSc theses:

Breitschwerdt, S., 2015. Comparison of analytical methods to determine the porosity of ceramic coatings, MSc thesis, LMU Munich.

Steinmetz, L., 2015. Investigation of Corrosion Resistance of Solvothermally Treated Samples under Defined Gas Atmospheres, MSc thesis, LMU Munich.

1 Introduction

Parts of this chapter are modified after Müller & Heuss-Aßbichler (2016) and Müller and coworkers (2016).

A major problem for the operation of waste-to-energy (WTE) plants is the corrosion of mainly metallic functional parts, like boiler tubes. Aggressive gases of chlorine and sulfur containing species, emerging from the combustion of solid municipal and industrial waste, have a high corrosion potential for steel tubes. This corrosion causes a thinning of the steel tubes, which can reach values of up to 1 mm per 1000 hours of operation (Spiegel et al. 2013). Consequently, this results in high maintenance costs, decreasing the efficiency of the WTE plant. Current corrosion protection is based on refractory brick linings within the combustion chamber and weld-overlays of nickel-based alloys with thicknesses of several millimeters (~2-3 mm) for e.g. membrane walls and superheater tubes. Especially the costs for weld-overlays are very high, in comparison to the brick lining (3000-5000 €/m² versus 1500 €/m²). Therefore, recent research activities are focused on more cost efficient coatings with comparable or even improved anti-corrosion properties, to be used on steel tubes in WTE plants. A multilayer coating consisting of a nickel-based bond-coat and a zirconia ceramic top-coat is supposed to be a promising candidate to act as anti-corrosion coating. A first test of this material combination within a WTE plant showed an improved corrosion resistance (Bendix et al. 2008). Notably, a modified area of YSZ at the border between bond- and top-coat was observed, which exhibited significantly reduced porosity. This observation suggests a densification process of the YSZ ceramic and, therefore, better wear and corrosion resistance. It seemed possible to develop a protecting layer for the underlying metallic substrate to improve its wear resistance and prevent further corrosion. This phenomenon was supposed to be based on a solvothermal transport of the zirconium via a vapor flux. In lab-scale experiments, under simulated waste incineration conditions, this densification of the zirconia has been reproduced successfully by an introduction of zirconium into the gas flow. Various tests were performed to analyze the mechanical and thermal shock resistance of the modified samples. They evidenced an improved adhesive strength between the ceramic top-coat and the metallic bond-coat (Fehr et al. 2012, Masset et al. 2013, Ye 2016).

In general, zirconium is not a common element within the flue gas of a WTE plant. This raises the question how the densification process observed within the YSZ top-coat of prior lab-scale experiments can occur when the material is exposed to WTE plant conditions. Therefore, lab-scale experiments with YSZ-coated samples under a synthetic atmosphere of nitrogen, gaseous hydrochloric acid and oxygen without additional zirconium introduced into the gas flow were performed. Decreasing temperatures from 1000 °C in the combustion chamber of a WTE plant down to 200 °C after the heat exchanger leads to condensation of salts on the surface of the coated steel tubes (Spiegel 1999). Since mixtures of these heavy metal containing salts are characterized by low eutectic melting points (Spiegel 1999), the interaction of salt melts in combination with the aforementioned synthetic atmosphere (N₂-HCl-O₂) with the zirconia ceramic at

elevated temperatures is of special interest, as well. To elucidate the behavior of YSZ under operation conditions of WTE plants the interaction of salt solution impregnated YSZ-coated samples under air as well as chlorine and sulfur containing atmospheres at 700 °C was investigated. Additionally, experiments with 5 wt.-% Y_2O_3 stabilized zirconia beads, embedded within a pure salt mixture of KCl - K_2SO_4 - $ZnCl_2$ - $ZnSO_4$ under chlorine containing atmospheres at 600–700 °C were conducted. Furthermore, YSZ-coated test probes were placed within a WTE plant, in order to examine the densification process under true operational conditions and to evaluate the applicability of the zirconia-based multilayer coating in WTE plants.

Within the framework of this research project “TS-Protect”, the mobility and transport mechanism of zirconium in nature was also investigated, which was done by Donja Abichler. The main focus of her studies was on sanidine rich volcanic rocks, which are known to contain high-field-strength element (HFSE) minerals, like baddeleyite (ZrO_2) or zircon ($ZrSiO_4$). Since these minerals often appear in a euhedral shape, it can be assumed that they formed from a vapor phase. The similarity of the supposed transport mechanisms of zirconium in nature and in lab-scale experiments has the potential to learn from nature how to improve the technical application.

1.1 History of waste incineration

The historical development of an organized treatment of waste by incineration dates back to the Roman Empire (Vehlow n.a.). During medieval times most of the knowledge vanished, leading to an uncontrolled dumping of waste in the landscape. During the 19th century, heavy cholera epidemics raged throughout Europe, affecting vast parts of the population. Besides the heavy odor pollution of uncontrolled waste dumps, health issues caused an increasing awareness of public cleanliness. In particular, since physicians and scientists, like Louis Pasteur and Robert Koch, proved the link between hygiene and diseases, an ordered treatment of waste has moved into focus of public interest. New achievements in engineering opened up the possibility for an industrial treatment of municipal solid waste, leading to the construction of the first waste incineration plant in England in 1876. Due to the positive experiences, the first waste incineration plant in Germany was built in 1892 in Hamburg. Such plants of the first generation were not very popular due to the unpleasant odor. That is why some of them were shut down after a short time of operation. Finally, technological advances in the field of engineering in combination with an increasing amount of waste led to the development of WTE plants (Bilitewski & Härdtle 2013). Their operating principle is based on the production of water steam (caused by the heat of the combustion) to produce electricity and supply industry and households with steam, to be used as industrial process steam or as a heat source. Nowadays, thermal treatment of waste is the major procedure to handle municipal and industrial solid waste in the industrial countries. Right now, 68 WTE plants are in service in Germany, with a combined annual capacity of 19.6 million tons (Umweltbundesamt – UBA 2016).

1.2 Layout of waste-to-energy plants

In principle, a WTE plant is comparable to a coal-fired power plant, but using solid waste as fuel. Therefore, it can be seen as a big steam boiler, converting the exhaust heat of the combustion to energy. This energy transformation is based on the production of steam, which is continuously heated up by circulating through steel tubes located at various areas of different flue gas temperature within the plant: economizer → vaporizer → superheater. The following description refers to the layout of the WTE plant in Schwandorf, Germany (Zweckverband Müllverwertung Schwandorf – ZMS), which represents also the in-situ test facility for various experiments described herein. The focus is especially on the heat exchange steam tubes, since the investigation of their coating is topic of this work.

The WTE plant in Schwandorf consists of four separate combustion lines with a total annual waste throughput of 450.000 t/a. It uses a horizontal grate system to burn municipal and industrial solid waste. A preheating of the water up to 220 °C happens within the economizer, located at the so called “tail end” of the WTE plant (Fig. 1-1). This area has the lowest temperature of the flue gas, before it enters the flue gas cleaning facility. Afterwards the preheated water moves to the vaporizer, where it is converted to steam. This part consists of membrane walls of the first pass (combustion chamber) as well as the second and third pass. Finally the steam reaches the superheater. Within the superheater section, the steam is heated to 410 °C at a pressure of 72 bar.

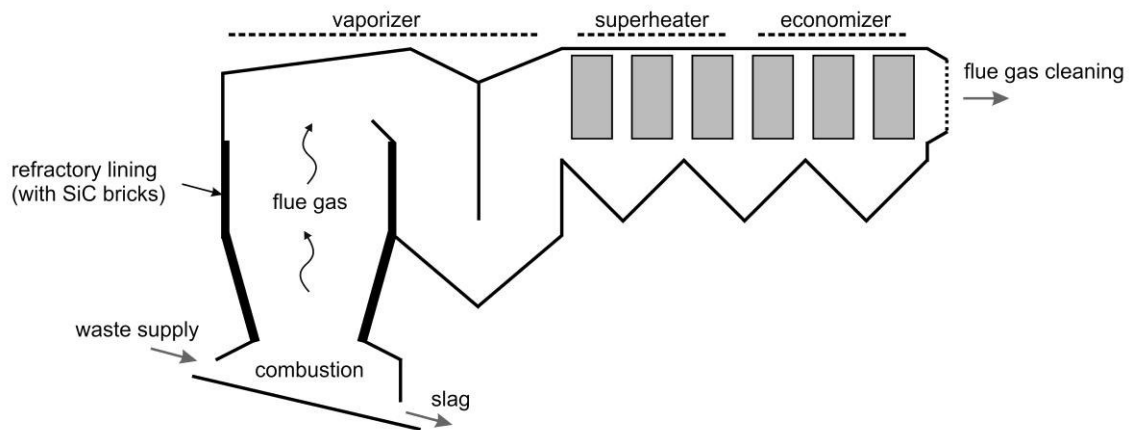


Fig. 1-1: Schematic layout of a WTE plant.

1.3 Corrosion in waste-to-energy plants

Since the early 1960s, corrosion phenomena of metal-based, functional parts (e.g. superheater tubes) within WTE plants have moved into the focus of scientific interest. The investigations at the WTE plant near Flingern, Germany in the late 1970s represented a big step forward: In order to increase the efficiency, WTE plants need to be operated at high temperatures and steam pressures. Based on empirical monitoring of corrosion processes within the WTE plant in Flingern, a diagram was generated, showing different

corrosion regimes in relation to the flue gas temperature and the steam tube surface temperature (Fig. 1-2). Ongoing research led to the development of an extended diagram, introducing the flow velocity of the flue gas (Warnecke 2003) and later on the chemical composition of the flue gas, especially the chlorine content (Warnecke 2014). A higher flue gas velocity and / or a higher content of chlorine lead to heavier corrosion. Recent studies bring the role of heat flow (within metallic parts) on the corrosion more to the fore (Magel et al. 2012). It was shown that an increased heat flow will also lead to an enhanced corrosion (AleBio 2014).

Depending on the fuel of the plant, the intensity and characteristics of the corrosion vary in a wide range. Municipal and industrial solid waste represents heterogeneous mixtures of different chemical compositions. This highly variable chemical composition of the fuel can cause temporary extreme conditions, regarding the distribution of chemical compounds, temperature and gas flow patterns within the plant (Spiegel et al. 2013). This can initiate an enhanced, local corrosion attack which accelerates the degradation of the metallic parts even under average operation conditions of the plant. The main corrosive species are volatile chlorides, e.g. alkaline and heavy metal chlorides, together with gaseous chlorine, oxygen and sulfur oxides (SO_x), summarized in Fig. 1-3.

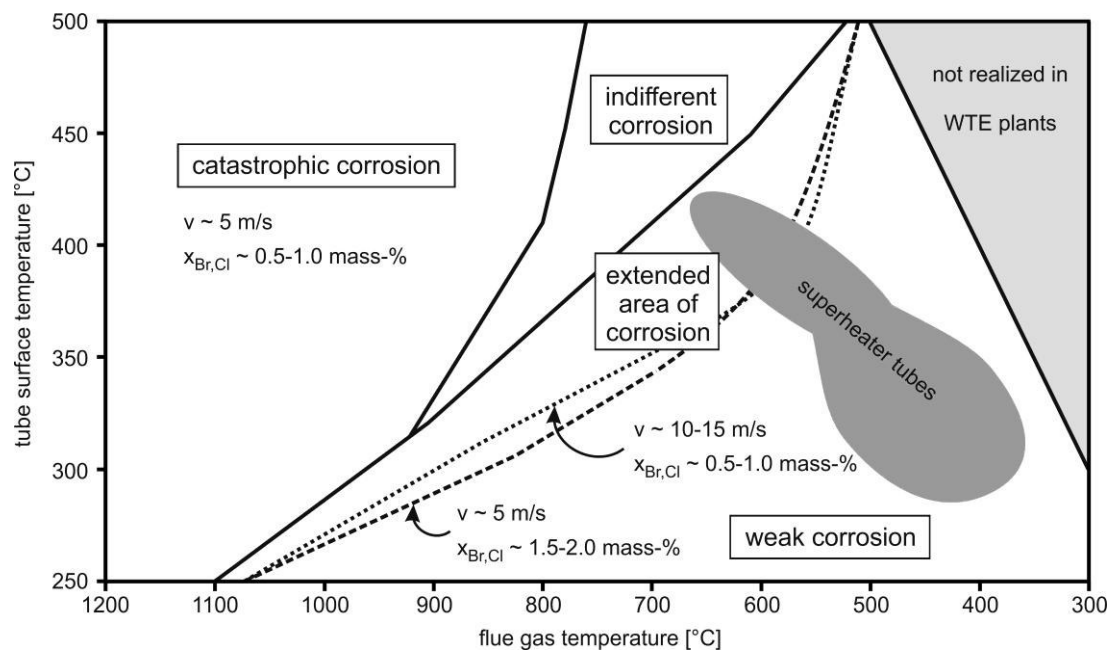


Fig. 1-2: Extended Flingern's corrosion diagram. After Warnecke (2003) and Warnecke (2014).

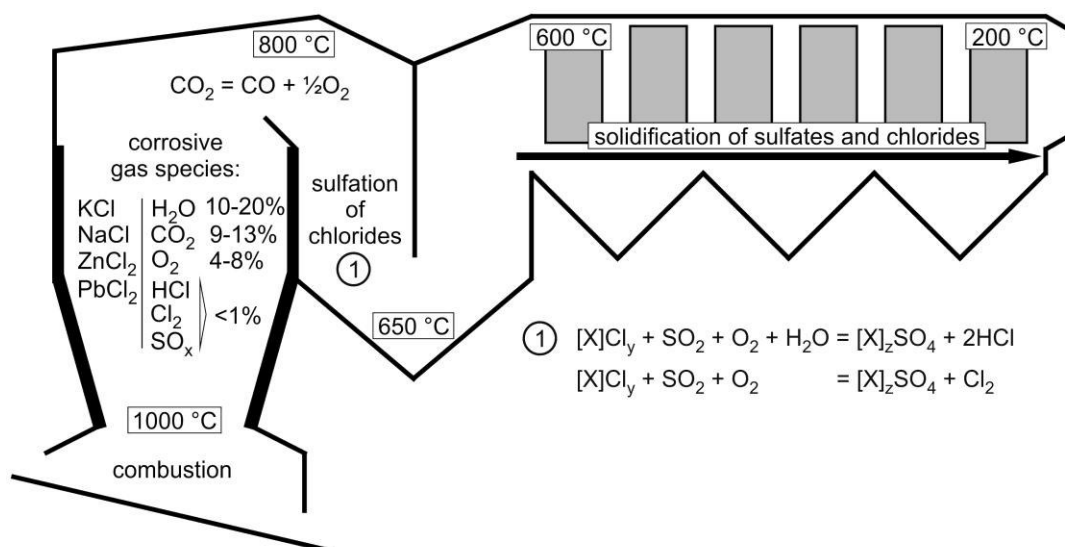


Fig. 1-3: Schematic layout of a waste-to-energy plant. Varying temperatures and corresponding gas compositions in combination with related chemical reactions are mentioned. Compiled after Belevi (2000) and Deuerling et al. (2009).

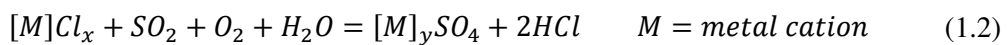
1.3.1 Corrosion phenomena

Corrosion phenomena can be distinguished in chemical and physical corrosion. Chemical corrosion deals with the interaction of gaseous or condensed phases with the metallic substrates. Depending on the local atmosphere, aerosol content and temperature, mainly three different chemical corrosion phenomena can be distinguished: (a) passive oxidation, (b) active oxidation and (c) hot corrosion. Passive oxidation describes the growth of an oxide layer (e.g. Fe₂O₃) in an oxidizing atmosphere. The resulting layer retards further oxidation of the underlying metallic substrate and can, therefore, be seen as a protective coating. The flue gases, resulting from the incineration of solid waste, do not only contain oxygen but also chlorine and sulfur containing species. Especially chlorine is able to penetrate metal oxide layers, enabling an interaction with the underlying metallic substrate. This process leads to a self-enhancing corrosion of the metal, called active oxidation. At decreasing temperatures, volatile chlorides will condensate and react with SO_x to form low-melting salt mixtures (see Fig. 1-3 – sulfation of chlorides). The dissociation of the salts leads to an acid-base chemistry within the melt, which can cause a fluxing of the substrate material, called hot corrosion. These processes described above generally occur at flue gas temperatures above 500 °C. This includes areas from the combustion chamber in the first pass to the front section of the superheater (see Fig. 1-1 and Fig. 1-3). Due to the importance of these phenomena, the process of active oxidation and hot corrosion are presented in more detail. Physical corrosion describes mechanical erosion of the tube surface by the impact of smaller particles, transported within the flue gas. Since physical corrosion is not the main topic of this work, it will not be discussed in detail.

1.3.1.1 Active oxidation

In contrast to passive oxidation, active oxidation is accompanied by the formation of a gaseous phase. This process was theoretically discussed by Wagner (1958) for the behavior of silicon under oxygen-bearing atmospheres at 1410 °C, leading to the formation of solid SiO₂ and / or gaseous SiO in dependence of the oxygen partial pressure. Later on, this reaction was intensively studied for SiC ceramics with respect to its technical application as e.g. wear resistant material or semiconductor (Presser & Nickel 2008, Jacobson & Myers 2011). In 1987, this process was named as active oxidation for the first time by Lee & McNallan (1987), who investigated the interaction of chlorine-oxygen atmospheres with nickel.

Besides the large-scale corrosion investigations at the WTE Flingern, the effect of chlorine-induced corrosion on metal substrates became a scientific topic for lab-scale experiments. Hauffe & Hinrichs (1970) investigated the interaction of chlorine and chlorine-oxygen atmospheres with nickel. In the presence of higher oxygen concentrations at temperatures between 750 – 800 °C, they observed a heavy corrosion of the nickel substrate, leading to a porous scale. Due to the high reaction rate of this surface destruction they called it “*Verbrennungsreaktion*” (burning / ignition reaction). Later on, the variety of studied substrates was successively extended to different metal alloys (Fe-Ni (Ihara et al. 1982), Fe-Ni-Cr (Elliott et al. 1985), Co-Ni-Cr (Oh et al. 1986)). In general, all studies describe a heavy corrosion under chlorine-oxygen atmospheres at higher temperatures, resulting in a porous scale of metal oxide(s). Grabke and coworkers (1995) observed similar corrosion phenomena on the surface of metallic substrates within WTE plants. Due to the presence of chlorine and oxygen in combustion gases from incinerated solid waste, they adopted the term active oxidation for similar corrosion processes occurring within WTE plants. Two different sources for the gaseous chlorine can be distinguished. (a) It can be formed during the combustion of the waste, emerging as molecular chlorine (Cl₂) or gaseous hydrochloric acid (HCl). Following Equation 1.1, gaseous hydrochloric acid can react with oxygen to form molecular chlorine and water. This reaction is in equilibrium at 593.48 °C, while for lower temperatures chlorine and water are the thermodynamically stable phases and hydrochloric acid and oxygen for temperatures above 593.48 °C. (b) Based on the presence of gaseous sulfur dioxide, hydrochloric acid (Equ. 1.2) or molecular chlorine (Equ. 1.3) can be formed as a consequence of the sulfation of chlorides. (Due to different valance states of the possible metal cations (e.g. Na⁺, K⁺, Zn²⁺, Pb²⁺), Equation 1.2 and 1.3 need to be equaled for the respective cation.)



The process of active oxidation is initiated through a penetration of the primary formed oxide scale by chlorine species (Fig. 1-4), leading to an increased chlorine partial pressure (p_{Cl_2}) at the scale - substrate interface. In Fig. 1-5 the phase stability diagrams for the systems Ni-Cl₂-O₂, Fe-Cl₂-O₂ and Cr-Cl₂-O₂ at temperatures of 450 °C and 700 °C are shown. At a constant oxygen partial pressure (p_{O_2}) and increasing p_{Cl_2} , the pure metal (as well as the metal oxide) will be transformed into its chloride equivalent following Equation 1.4. (Due to different valance states of the possible metal cations (Ni²⁺, Fe²⁺, Fe³⁺, Cr³⁺), Equation 1.4 need to be equaled for the respective cation.)



The chlorination of pure metals strongly depends on the temperature. While for the transformation of metal oxides to metal chlorides, the p_{Cl_2} is the major parameter. Once formed at the scale – substrate interface, those highly volatile metal chlorides will transform into their gaseous equivalent and subsequently diffuse along open pores and cracks through the scale. At regions with higher p_{O_2} values, they will consequently oxidize, forming a porous metal oxide scale, following Equation 1.5. (Due to different valance states of the possible metal cations (Ni²⁺, Fe²⁺, Fe³⁺, Cr³⁺), Equation 1.5 need to be equaled for the respective cation.)



The released chlorine, together with the primary chlorine from the combustion gas, can again move to the scale - substrate interface to react with the steel (Fig. 1-4). This cycle represents a self-enhancing system, leading to massive corrosion of metallic parts within WTE plants (Grabke et al. 1995).

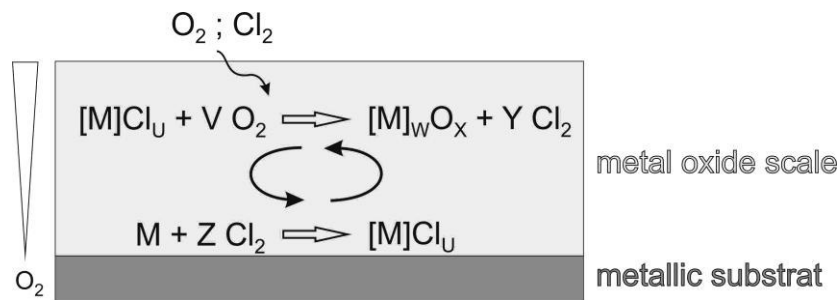


Fig. 1-4: Sketch of the active oxidation process on the surface of oxidized metal substrates. M – metal cations (e.g. Ni²⁺, Fe²⁺, Fe³⁺, Cr³⁺); U, V, W, X, Y, Z – integers, depending on the valance states of the possible metal cations.

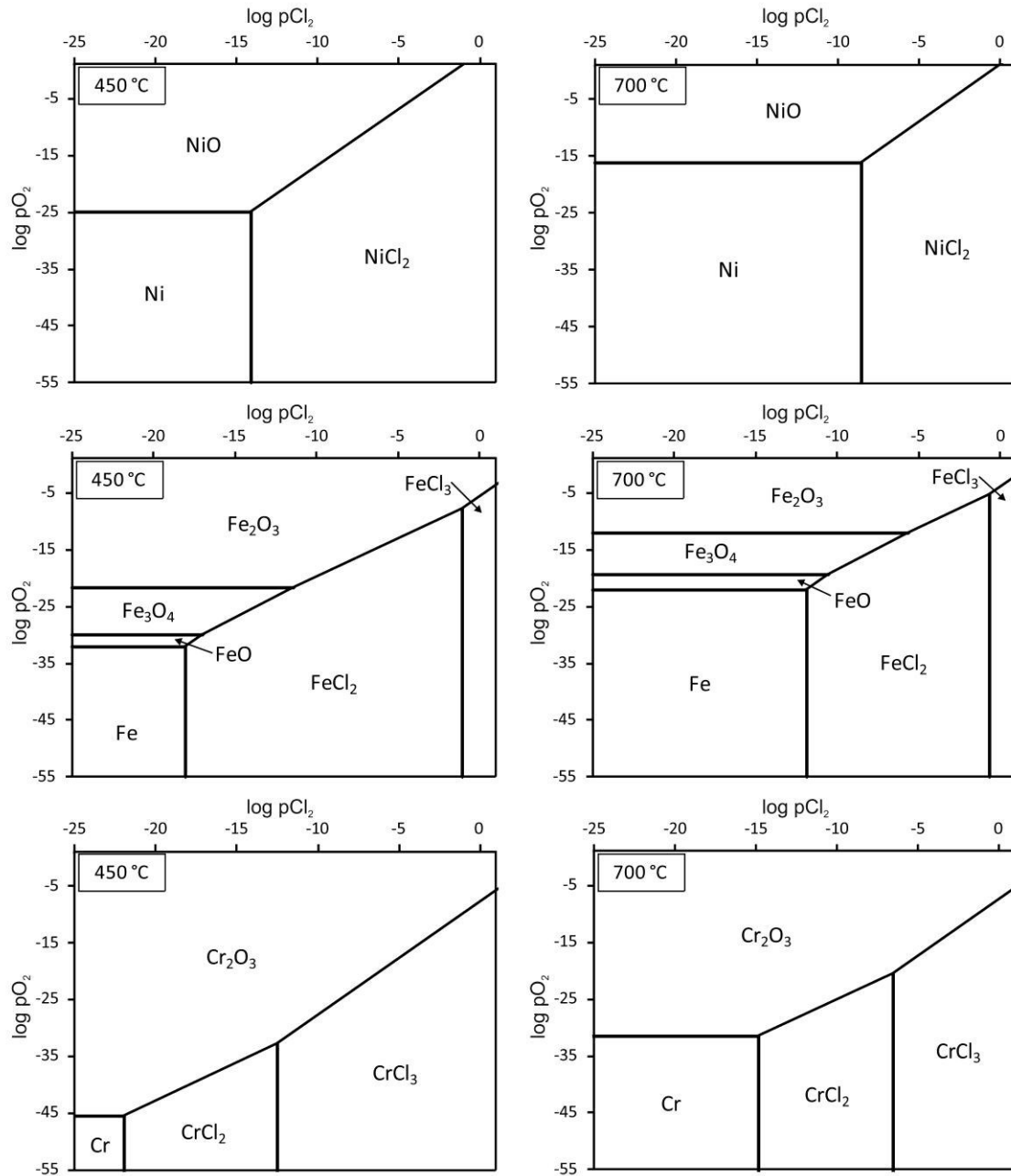


Fig. 1-5: Phase stability diagrams for nickel, iron and chromium with respect to partial pressures of chlorine ($p\text{Cl}_2$) and oxygen ($p\text{O}_2$) at temperatures of 450 °C (left) and 700 °C (right). All values of $p\text{O}_2$ and $p\text{Cl}_2$ are given in bar. Calculated with HSC Chemistry.

1.3.1.2 Hot corrosion

Parts of this chapter are modified after Müller & Heuss-Aßbichler (2016).

Due to the presence of various metal chlorides and sulfates within the flue gas these phases can react to form low-melting salt melts on the surface of metallic parts within the WTE plant (Spiegel 1999). Early research on the interaction of salt melts with metallic substrates was mainly driven by failures of jet-engines after the aircraft operated near the seawater surface during the Vietnam War in the 1960s (Rapp 2002). Swirled water vapor, containing dissolved salts (e.g. NaCl), was sucked into the engine where it reacted with sulfur from the fuel to form sodium sulfate (Na_2SO_4). At temperatures above 884 °C this

resulted in the formation of a thin film of molten Na_2SO_4 on engine parts. An accelerated corrosion of the metallic parts was observed by a sulfidation of the metal (Simons et al. 1955, Goebel & Pettit 1970). Further studies by Bornstein & DeCrescente (1971) have shown that this process does not necessarily depend on the presence of sulfur, but also happens under salt melt coatings of Na_2CO_3 or NaNO_3 . Due to the similarity of this process with atmospheric corrosion, which is initiated by a thin film of water, it was further on called hot corrosion. Hot corrosion can be subdivided into two groups: Type I – High Temperature Hot Corrosion (HTHC) describes processes at temperatures above the melting point of the involved salt phases. Type II – Low Temperature Hot Corrosion (LTHC) describes processes at temperatures below the melting point of the involved salt phases. The latter one requires the incorporation of corrosion products from the attacked substrate to lower the melting point of the salt mixture (Rapp & Zhang 1994).

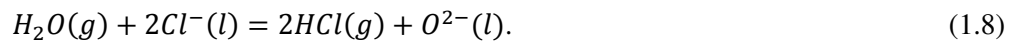
Nishikata and coworkers (1991), Rapp & Zhang (1994) and Cherginets (2005) provide a theoretical as well as practical approach based on thermodynamic calculations and experiments to describe corrosion processes initiated by molten salts. Their work emphasizes the role of acid-base reactions within the melt. Based on the Lux-Flood model, the basicity of a melt can be described by Equation (1.6):

$$pO^{2-} = -\log a_{O^{2-}}. \quad (1.6)$$

An increasing value of pO^{2-} corresponds with an increasing acidity. In sulfate containing melts, this value depends on reaction (1.7):



For chlorine containing melts an additional oxygen source is needed. This can be a water containing atmosphere, reacting with the salt melt as described by Equation (1.8) (Ishitsuka & Nose 2002):



Investigations of metal oxides in salt melts revealed an amphoteric behavior for Cr_2O_3 , Fe_3O_4 , NiO and Co_3O_4 . These phases are stable under intermediate values of basicity and dissolve under acidic and basic regimes. SiO_2 was dissolved under basic conditions only (Ishitsuka & Nose 2002).

1.4 Corrosion protection

In general, corrosion protection can be divided into active and passive methods. Active methods are employed to combat the causes of corrosion, while passive ones are used to minimize the impact of corrosion. It is well-known, that solid waste represents a heterogeneous mixture and needs to be homogenized in order to permit constant combustion conditions. This is done by “manual mixing” of the waste within the waste storage container prior to the combustion. A further primary prevention of corrosion can

also be realized through an optimization of the combustion process by using different grate systems (e.g. horizontal grate or reverse-acting grate) or through an improved flue gas management (pers. Comm. Martin J. Murer, Martin GmbH, Kassebohm 1989, Hunsinger & Andersson 2014). The corrosion inhibition by artificial additives mainly aims to minimize the chlorine induced corrosion. This can be realized by an addition of calcium and silicon oxide (Faulstich et al. 2001) or aluminum-silicon species (Coda et al. 2001) in order to initiate the formation of silicate phases, which incorporate chlorine in their crystal structure and, therefore, remove it from the flue gas. By a combination of various active corrosion protection procedures, like mentioned above, it is possible to minimize corrosion phenomena within a WTE plant but not to diminish them. Therefore, an additional passive corrosion protection needs to be employed. Within the combustion chamber, the blank steel tubes are covered with a refractory lining (e.g. SiC bricks). A failure of the anti-corrosion lining can be caused by a reaction of the binder material with elements from the flue gas (Pawlowski et al. 2006). This leads to the formation of secondary phases, causing a breakdown of the brick structure. At lower temperatures in the upper part of the combustion chamber and following sections until the front part of the superheater, the refractory lining is replaced by weld-overlay coatings (claddings) on the steel tubes. Especially Inconel 625 is a widely used coating material, due to its good corrosion resistance under operation conditions of WTE plants (Ganesan et al. 1991, Spiegel 2000, Montgomery et al. 2013). The utilization of alloyed steel (16Mo3) for superheater tubes, without any coating, represents a compromise of good corrosion resistance and moderate costs. As a consequence of the increasing improvement of thermal spray techniques, thermally sprayed coatings moved into the focus of academic and industrial research for application in WTE (and biomass combustion) plants in recent years (Bendix et al. 2008, Szymanski et al. 2015). In comparison to weld-overlays, thermally sprayed coatings exhibit several advantages: (a) Less interaction with the underlying substrate during application results in an intact surface of the substrate and a smaller iron uptake of the coating. (b) The coating thickness can be easily adjusted, depending on the corrosion attack at the respective position. This in turn enables the usage of (c) thinner coating thicknesses, with the advantage of an improved heat transfer. (d) The possibility to produce multilayer coatings allows the combination of various materials to improve corrosion resistance or to accommodate special requirements of the coating. One major drawback of thermally sprayed coatings is their structure, consisting of single splats which are a result of the (partial) melting of the feedstock powder during application. Especially for metallic materials this leads to an interchange of metallic and metal oxide layers, separated by grain boundaries and pores. This enables the penetration of aggressive species along these pathways, which represents an increased risk for corrosion (Schmidl 2009).

2 Corrosion of zirconia ceramics

Parts of this chapter are modified after Müller & Heuss-Aßbichler (2016).

Zirconia is a general term for zirconium dioxide (ZrO_2). Its natural form is known as the mineral baddeleyite, which exhibits a monoclinic crystal structure. In the early years of the 20th century ZrO_2 ceramics were identified as exceptionally well-suited refractory materials. During the usage of this material it was found out that pure zirconia has a low thermal shock resistance, which ultimately leads to a total failure of the zirconia (Ruff & Ebert 1929). A subsequent investigation revealed the presence of the three different polymorphs of zirconia: monoclinic $< 1170\text{ °C} \rightarrow$ tetragonal $< 2370\text{ °C} \rightarrow$ cubic $2706\text{ °C} \rightarrow$ melt. These new insights led to the idea of a stabilization of high-temperature modifications by the addition of different oxides. First, this was successfully done for stabilization of the cubic phase by an addition of MgO , CaO , Sc_2O_3 , Y_2O_3 or CeO_2 at 1750 °C (for ThO_2 at $T > 2400\text{ °C}$). This effect was attributed to the similar ion-radii of the added cations in comparison to zirconium (Ruff & Ebert 1929). More recent studies with undersized (Fe_2O_3 , Ga_2O_3) and oversized (Y_2O_3 , Gd_2O_3) trivalent dopants give more detailed insights into the stabilizing mechanism, emphasizing the role of the oxygen vacancies (Li et al. 1994). Li and coworkers (1994) concluded a more effective stabilization of tetragonal and cubic zirconia for oversized trivalent cations (e.g. Y^{3+} and Gd^{3+}).

Based on the discovery of the transformation toughening process for zirconia in 1975 (Garvie et al. 1975), zirconia attracted an increasing attention in academic and industrial research. The intensive study of this toughening process (Claussen 1985, Evans & Cannon 1986, Heuer 1987) boosted the application of zirconia in industry (Hannink et al. 2000).

Nowadays, yttria-stabilized zirconia (YSZ) is a widely used material in industry due to its outstanding properties, like chemical resistance, wear resistance, ionic conductivity, high melting temperature and low thermal conductivity. Of particular interest for this work is its utilization as a coating material. Since the 1960s YSZ has been used as a thermal barrier coating (TBC) material in jet engine turbines and land-based gas turbines in order to increase their operating temperature and so increase their efficiency (Clarke et al. 2012). In order to avoid phase transformations during sintering and application a stabilization of the high-temperature phase is absolutely essential.

2.1 Zirconia under chlorine-bearing atmospheres

The interaction of zirconia with chlorine-bearing atmospheres can be described by the chlorination process (Equations 2.1 and 2.2). The stability field of zirconia in dependence on the oxygen ($p\text{O}_2$) and chlorine ($p\text{Cl}_2$) partial pressure is shown in Fig. 2-1. This transformation of metals and metal oxides to their corresponding chlorides enables their easy separation through distillation, known as the Kroll-process (Kroll 1937). This process is widely used in industry for the extraction of metals from ores or metallic scrap as well as for the purification of metals (Mukherjee & Gupta 1983, Jena & Brocchi 1997,

Bohé et al. 1996). Furthermore, this method can be used to synthesize various materials by an inversion of the process, leading to the formation of oxides, e.g. ZrO_2 (Bohé & Pasquevich 1997).

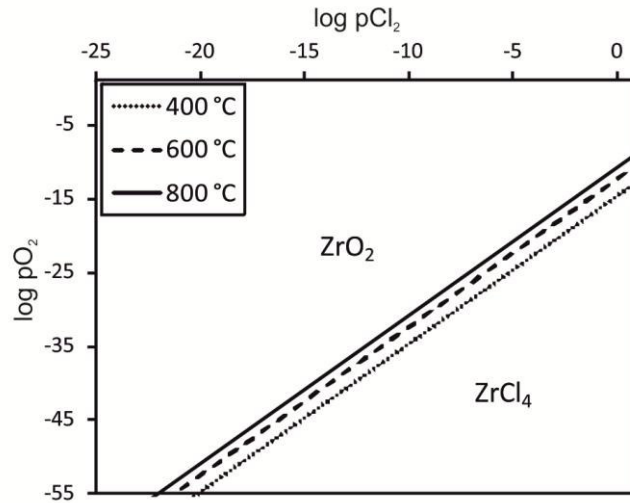


Fig. 2-1: Thermodynamic phase stability diagram for the system $\text{Zr-O}_2\text{-Cl}_2$ for the temperatures 400, 600 and 800 °C. All values of $p\text{O}_2$ and $p\text{Cl}_2$ are given in bar. Calculated with HSC Chemistry.

Investigations on the sintering behavior of ZrO_2 under a chlorine-bearing atmosphere in the range from 1100 to 1300 °C (Readey & Readey 1986) and for YSZ at 940 °C (Pasquevich et al. 1989) revealed an enhanced grain growth in comparison to chlorine free environments. This process was supposed to be based on a vapor phase transport by ZrCl_4 (Readey & Readey 1986) or on adsorption effects of the chlorine on the grain surface, leading to an enhanced surface diffusion (Pasquevich et al. 1989). Additionally a partial phase transformation from tetragonal to monoclinic zirconia was observed for the YSZ samples (Pasquevich et al. 1989).

2.2 Zirconia under aggressive melts

Chloride and sulfur containing salt melts are common constituents within deposits on heat exchanger tubes installed in WTE plants. Therefore, their interaction with zirconia is of special interest for this work.

A rough estimation of the stability field of ZrO_2 in chloride salt melts can be drawn from a phase diagram, calculated by Cherginets (2005) (Fig. 2-2). He constructed the stability field for a zirconia membrane oxygen electrode in a KCl-NaCl melt at 1000 °C on the basis of data from Combes and coworkers (1970). The resulting theoretical stability field for ZrO_2 is located at intermediate $p\text{O}^{2-}$ values ($3 < p\text{O}^{2-} < 13$).

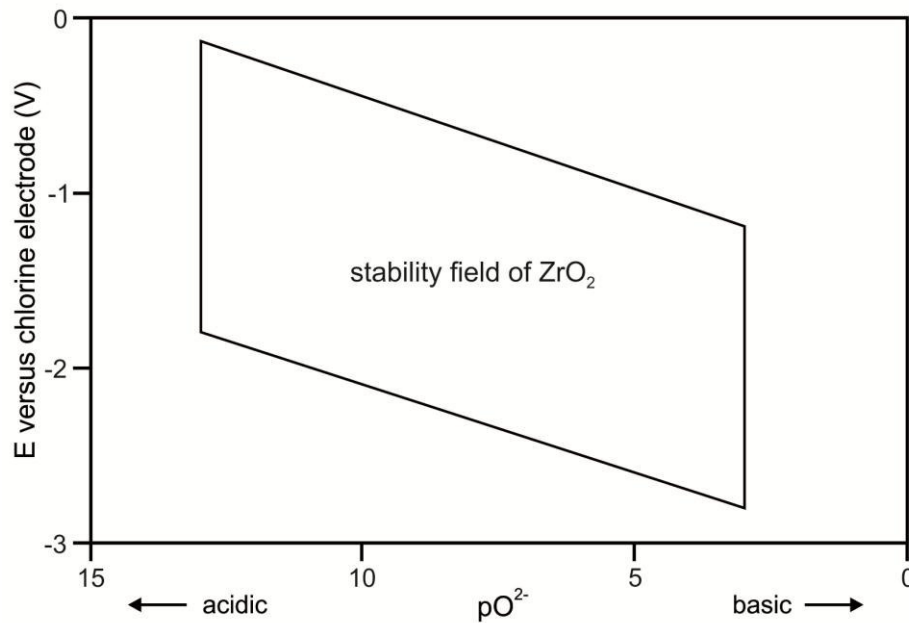


Fig. 2-2: E-pO²⁻ diagram showing the stability field of ZrO₂ in an eutectic melt of KCl-NaCl at 1000 °C. Modified after Cherginets (2005).

Various experimental studies were carried out to investigate the interaction of zirconia with different kinds of salt mixtures: Rao and coworkers (2012) studied the behavior of a multilayer coating, applied by atmospheric plasma spray (APS) method. It consists of an YSZ top-coat and a nickel-based alloy (NiCrAlCoY) bond-coat on a steel substrate. The YSZ coating interacted with a salt mixture of KCl-Na₂CO₃-Na₂SO₄-K₂SO₄ at 600 °C for 168 h under regular air or a mixture of oxygen, carbon dioxide, water and nitrogen. In dependence on the used feedstock powder size (µm- or nm-sized) they observed different penetration depths of the salt but no change of the ceramic material, neither morphologically nor chemically. Further studies by Shankar and coworkers (2008) investigated the interaction of an APS-applied YSZ (8 wt.-% Y₂O₃) coating with LiCl-KCl salts at 600 °C under argon-atmosphere for a duration of up to 500 h. As a result, they found only a little degradation, represented by a mass loss of 0.3 %. Lee & Baik (2009) investigated an APS-applied YSZ (8 wt.-% Y₂O₃) coating in contact with a LiCl-Li₂O melt at 650 °C under an atmosphere of nitrogen with 10 % oxygen. They observed no reduction of the coating thickness, but the formation of a dense amorphous surface layer of a lithium-zirconium oxide which was considered to act as a protective layer against further corrosion.

Various hot-corrosion studies were performed on the behavior of zirconia within salt melts of Na₂SO₄ and V₂O₅ (Ahmadi-Pidani et al. 2012, Habibi & Guo 2015), Na₂SO₄ and NaVO₃ (Xu et al. 2010, Reddy & Gandhi 2013), pure NaVO₃ (Park et al. 2005) or pure V₂O₅ (Chen et al. 2009) under atmospheric pressure in a temperature range between 750 – 1050 °C. Considering an application of zirconia as TBC in turbines, their choice of salt components was based on common contaminants of vanadium, sodium and sulfur in low-grade fuels. In general they observed the formation of YVO₄, initiating a structural destabilization of the tetragonal zirconia phase through consumption of the stabilizing agent yttrium. The following phase transformation from tetragonal (t-ZrO₂) to monoclinic

(m-ZrO₂), accompanied by a volume increase of approximately 4 %, finally leads to a degradation of the ceramic. Habibi & Guo (2015) described the formation of YVO₄ and m-ZrO₂ as the result of an yttrium leaching process while Reddy & Ghandi (2013) and Chen and coworkers (2009) assumed a dissolution of the yttria-stabilized zirconia followed by a precipitation of YVO₄ and m-ZrO₂ (and ZrV₂O₇ at temperatures ≤ 750 °C (Chen et al. 2009)). A similar process of yttrium leaching with subsequent phase transformation was observed by the interaction of zirconia with a metallurgical slag of a silica rich composition at 1500 °C under atmospheric pressure (Hemberger et al. 2012). Besides the considerable higher temperature, silicon is assumed to play a major role as a corrosive medium through the formation of yttria-silicates (e.g. Y₂SiO₄).

Numerous investigations on the interaction of zirconia TBCs with molten silicates were done. In particular after the eruption of the Icelandic volcano Eyjafjallajökull in March 2010, which dramatically impeded aeronautics in the North Atlantic region by a widespread distribution of volcanic ash clouds (Sammonds et al. 2010). Most of the studies, investigating YSZ - molten ash interaction, use a synthetic mixture of calcium, magnesium, aluminum and silicon oxides (calcium-magnesium-alumino-silicate - CMAS). Craig and coworkers (2015) conducted a detailed study on the influence of the basicity of the melt with respect to degradation phenomena of YSZ coatings. Therefore, they introduced a basicity index (BI) as the molar ratio of basic oxides versus acidic oxides, with BI < 1.8 defined as acidic and BI > 2.2 as basic conditions. Basic oxides are CaO, MgO, Na₂O and K₂O, acidic ones are SiO₂ and P₂O₅, whereas Al₂O₃, TiO₂ and Fe₂O₃ exhibit an amphoteric character. Under acidic conditions a leaching of yttrium was found, leading to t→m phase transformation of the zirconia. Under basic conditions, a complete dissolution of the zirconia was observed, followed by a recrystallization of fully stabilized cubic zirconia, with calcium and yttrium as stabilizing agents.

Zirconia degradation experiments in corrosive hydrothermal solutions under high temperature and high pressure (390 °C / 27 MPa (Schacht et al. 1998); 600 °C / 100 MPa (Yoshimura et al. 1986)) or low temperature and low pressure (≤ 80 °C / 1 atm (Shojai & Mäntylä 2001a, Shojai & Mäntylä 2001b, Fang et al. 1999)) yield an yttrium leaching and subsequent t→m phase transformation as well. It was found that this process is accelerated in acidic hydrothermal solutions containing HCl or H₂SO₄, which was attributed to the basicity of yttrium. Of particularly interest are observations by Yoshimura and coworkers (1986), who observed not only decomposition, as a consequence of t→m phase transformation, but dissolution and precipitation of zirconia crystals within hydrothermal solutions at 600 °C and 100 MPa: Precipitates of cubic or monoclinic zirconia grains were observed for solutions containing 15 wt.-% KOH or LiOH, respectively. Solutions with 30 wt.-% H₂SO₄ yield the growth of monoclinic zirconia whiskers on the surface of the previously dissolved surface of YSZ crystals.

2.3 Corrosion prevention by densification of thermally sprayed zirconia coatings – state of the art

In order to reduce the porosity of thermally sprayed zirconia coatings, various techniques are available. In general they are based on a physical sealing process like: (a) a variation of the process parameters for the APS deposition (Brinkiene & Kezelis 2004, Vaidya et al. 2008), (b) an infiltration of the pores by an afterwards solidifying material or (c) a post-treatment by the means of sintering. Sintering can be achieved through heating the whole specimen in a furnace at temperatures above 1100 °C (Siebert et al. 1999). This method bears the risk of phase transformation from tetragonal to monoclinic zirconia, accompanied by a volume increase of ~4 % (Krogstad et al. 2011), leading to a detachment of the coating. On a more local scale the coating can be sealed by laser melting (Fu et al. 1997, Szkaradek 2010) or high-current pulsed electron beam melting (Cai et al. 2014), with the drawback of a rapid heating and cooling that can lead to micro cracks causing again a detachment of the coating. A further method (d) can be an additional chemical vapor deposition (CVD) coating on top of the APS coating (Rajendran et al. 1995), which represents a very expensive alternative.

To overcome these disadvantages, a chemical densification process, as described herein, would be preferable. The densification discussed in the context of this work describes a process to reduce the porosity of the zirconia top-coat through a vapor flux. This effect was observed by Bendix and coworkers (2008) for the first time. They investigated several material combinations of APS-applied coatings on steel test probes, placed for 500 h (~21 days) in the WTE plant of Schwandorf. One of the tested materials was a multilayer system of a nickel-based bond-coat covered by an yttria-stabilized zirconia top-coat. The investigation of the test probe after the experiment revealed the formation of a zone with reduced porosity at the bottom of the zirconia top-coat. It was assumed that this phenomenon represents the effect of a solvothermal process, based on a mobilization and recrystallization of the zirconia through a solvent. Presumably the solvent consisted of species from the zirconia top-coat and from the nickel-based bond-coat. In lab-scale experiments, under simulated waste incineration conditions, this densification of the zirconia has been reproduced successfully (Fehr et al. 2012, Masset et al. 2013, Ye 2016). Those experiments were done in a temperature range between 600 and 800 °C, utilizing a synthetic atmosphere of nitrogen with 2 vol.-% gaseous hydrochloric acid. An eutectic salt mixture of potassium and zinc chlorides and sulfates (KCl, ZnCl₂, K₂SO₄, ZnSO₄) was mixed in a fused silica crucible together with YSZ powder. This crucible was placed in the gas flow beneath the coated steel cylinder. The salts melt during the heating of the furnace, due to their low melting point of 294 °C, hence releasing chlorine and sulfur species in the gas flow. It was assumed that highly volatile zirconium chloride (ZrCl_x) species will form in-situ, which finally diffuse through open pores and cracks of the YSZ top-coat. Reducing conditions at the border between bond-coat / top-coat lead to the reduction of SO_x compounds, releasing oxygen. The availability of oxygen enables the recrystallization of the zirconia, responsible for the reduced porosity of the top-coat.

3 Experimental

Parts of this chapter are modified after Müller & Heuss-Aßbichler (2016) and Müller and coworkers (2016).

The zirconia-coated metallic heat exchange tubes have to withstand mainly two different corrosion processes in WTE plants: An interaction with (a) aggressive gaseous phases (1.3.1.1 Active oxidation) and (b) low-melting salt melts (1.3.1.2 Hot corrosion). In order to investigate the behavior of YSZ ceramics under these conditions, three different types of lab-scale experiment series were conducted: (I) zirconia - gas phase interaction, (II) zirconia - salt melt interaction, (III) zirconia - gas phase and salt interaction. Additionally, zirconia-coated test probes were placed in a WTE plant for in-situ investigations under real application conditions with a combined attack of gaseous phases and salt melts.

3.1 Samples

All coated samples were prepared at the Fraunhofer UMSICHT institute in Sulzbach-Rosenberg, Germany. The coatings were applied by APS technology, using a F4 plasma torch from Sulzer Metco, Switzerland. Prior to each coating step the substrate was corundum-blasted and heated to 150 °C, in order to ensure a proper bonding between coating and underlying material (Karger et al. 2011). The layout of the used multilayer coating is similar for all samples, consisting of a steel substrate, followed by a nickel-based bond-coat and an YSZ top-coat. The thicknesses varied between 70 – 150 µm for the bond-coat and 180 – 300 µm for the top-coat. A metallic bond-coat is recommended for the application of a ceramic top-coat, due to the different thermal expansion coefficients of the steel substrate ($12 - 15 \cdot 10^{-6} \text{ K}^{-1}$ (Richter 2010)) and the YSZ top-coat ($7 - 8 \cdot 10^{-6} \text{ K}^{-1}$ (Hayashi et al. 2005)). Furthermore, the nickel-based bond-coat represents an additional corrosion protection for the underlying steel. The composition of the used materials is summarized in Tab. 3-1.

3.1.1 Gas phase and gas phase – salt melt experiments

As substrate material, steel cylinders with a diameter of 2 cm and a height of 1 cm of two different steels were used: (a) a low-grade steel (St35.8 / 1.0305) and (b) a high-grade steel (1.2343). The samples were coated with a multilayer coating of Diamalloy 1005 (Sulzer Metco, Switzerland) or Nibasit 625-P (DEW, Germany) as bond-coat and 8 wt.-% Y_2O_3 stabilized zirconia (GTV, Germany) as top-coat (Fig. 3-1).

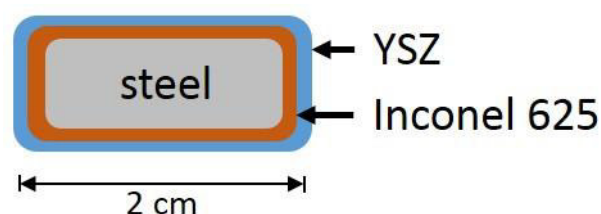


Fig. 3-1: Sample layout for lab-scale experiments.

3.1.2 Salt melt experiments

The investigated materials are yttria-stabilized zirconia beads (Zirmil Y from Saint-Gobain, France) with 5 wt.-% (2.66 mol.-%) Y_2O_3 . The material selection was based on its later application as thermally sprayed coating, where yttria-stabilized tetragonal zirconia is used.

3.1.3 Waste-to-energy plant test probes

All parts of the heat exchanging system in WTE plants must fulfill boiler engineering requirements, e.g. seamless steel tubes to resist high steam pressures. Superheater components consist of seamless 1.0345-steel tubes, which are manufactured by the so called Mannesmann- or pilgrim-rolling process. The original steel tube, referred to as substrate, is used as a testing probe for in-situ investigations (Fig. 3-2). In order to record the temperature history and to ensure a desired temperature profile they are equipped with thermocouples and a thermostat.

For the nickel-based bond-coat Nibasit 625-P (DEW, Germany) was used and 8 wt.-% Y_2O_3 stabilized zirconia (GTV, Germany) for the top-coat.

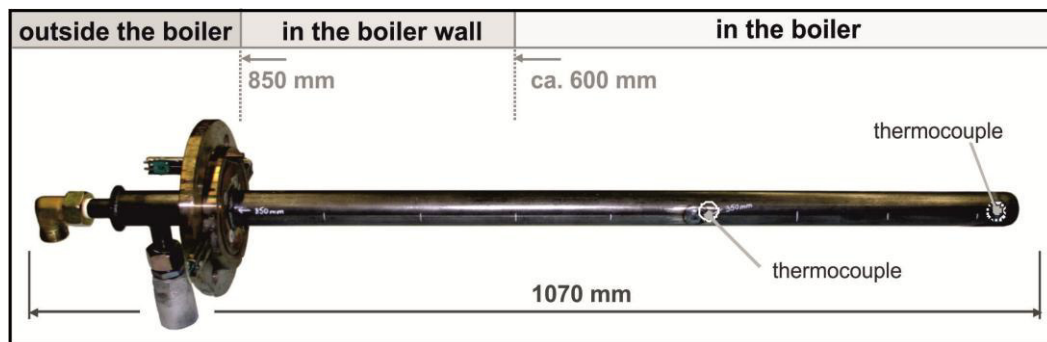


Fig. 3-2: Layout of a test probe for in-situ tests within a WTE plant (original appearance without coating). Modified after Müller and coworkers (2016).

Tab. 3-1: Overview of the used materials for top-coat, bond-coat and steel substrate. For the steel only the additives are mentioned.

layer	material	composition (all data are given in wt.-%)			
top-coat	YSZ (GTV, Germany)	Al ₂ O ₃	SiO ₂	TiO ₂	Fe ₂ O ₃
		0.06	0.03	0.05	0.03
		CaO	MgO	Y ₂ O ₃	ZrO ₂ + HfO ₂
		0.04	0.07	8.15	balance
bond-coat	Nibasit 625-P (DEW, Germany)	Cr	Mo	Fe	Nb
		22.00	9.00	4.00	3.60
		C	Ni		
		< 0.06	balance		
	Diamalloy 1005 (Sulzer Metco, Switzerland)	Cr	Mo	Fe	Nb+Ta
		21.50	9.00	2.50	3.70
		Ni			
		balance			
steel	1.0345 *	C	Mn	P	S
		< 0.16	0.6 - 1.2	< 0.025	< 0.015
		Si	V	N	Nb
		< 0.35	< 0.02	< 0.012	< 0.02
		Ti	Al	Cr+Cu+Mo+Ni	
		< 0.03	< 0.02	< 0.7	
	1.2343 *	C	Mn	P	S
		0.33 - 0.41	0.25 - 0.50	< 0.03	< 0.02
		Si	V	Cr	Mo
		0.8 - 1.2	0.3 - 0.5	4.8 - 5.5	1.1 - 1.5

* data from www.steelnumber.com

3.2 Experimental setup for lab-scale experiments

3.2.1 Gas phase experiments

In order to investigate the interaction of the zirconia top-coat with a synthetic atmosphere, simulating the operation conditions of a WTE plant, a vertically mounted tube furnace was used. Since the experiments described herein are based on previous work of the research project “ForLayer” (Fehr et al. 2012, Ye 2016), the existing (old) experimental setup (Fig. 3-3) was used for the first experiments (Tab. 3-2). This furnace was equipped with a gas supply for nitrogen (N_2) and gaseous hydrochloric acid (HCl). The furnace was composed of a high-grade steel housing, and only along the high temperature experiment chamber it was lined with alumina. Later on the experimental setup was changed, to fulfill new requirements. Therefore, an additional oxygen gas supply was added and the experiment chamber was changed to consist of fused silica only (Fig. 3-4).

Before each experiment the furnace was purged with nitrogen for 30 minutes in order to remove residual air to guarantee a controlled synthetic atmosphere. Afterwards, the respective gas mixture was introduced. It was possible to place a salt mixture within the gas flow. Therefore, the solid salts were mixed in a fused silica crucible, which was placed below the coated sample in the central part of the high temperature experiment chamber. The used salt mixtures were chosen to consist of KCl, K_2SO_4 , $ZnCl_2$, $ZnSO_4$, NaCl and / or Na_2SO_4 , to represent actual conditions within a WTE plant. Due to the low melting point(s) of the used salt mixture(s), they melt during heating of the furnace. The heating rate was kept at 3 K/min, while the cooling rate was lower. The cutting of the sample was done with a wire saw. To prevent further corrosion, the samples were stored in an evacuated desiccator.

3.2.2 Combined gas phase and salt melt experiments

Parts of this chapter are modified after Steinmetz (2015).

Before heat treatment, the samples were impregnated with saturated, equimolar solutions of potassium and zinc, sodium and zinc or potassium and sodium chlorides and sulfates (Tab. 3-3). To ensure a filling of the pores within the coating, the impregnation was done under vacuum within a desiccator. For experiments under HCl- O_2 atmosphere and air, the furnace shown in Fig. 3-4 was used. The experiment under a SO_2 containing atmosphere was performed in the furnace of Dr. Paul M. Ayris (Ayris et al. 2015). A detailed description of the experimental setup can be found in the MSc thesis of Lukas Steinmetz (Steinmetz 2015).

3.2.3 Salt melt experiments

40 YSZ beads with a diameter of 2.3 mm (\varnothing 2.012 g) were taken for each experiment. The YSZ beads were placed in an Al_2O_3 crucible (Alsint 99.7, Haldenwanger, Germany) together with an equimolar KCl- K_2SO_4 - $ZnCl_2$ - $ZnSO_4$ salt mixture, summarized in Tab. 3-4. After the experiment the beads were completely covered by the salt melt. Since

molten salts exhibit a volume increase of up to 25 % in contrast to their solid equivalent (Landon & Ubbelohde 1956), it can be assumed, that the beads were covered by the salt melt during the whole experiment. The experiments were conducted in a fused silica tube, vertically emplaced in a tube furnace (Fig. 3-4). This tube was purged by a gas mixture of 97 vol.-% N₂, 2.55 vol.-% HCl and 0.45 vol.-% O₂. The temperature range was 600 – 700 °C (heating rate at 3 K/min, cooling rate < 3 K/min) and the duration of the experiments varied between one and four days (see Tab. 3-4). The evaluation of the chemical composition of the beads was done by electron-probe micro-analysis.

After the experiment, the crucible was placed in deionized water to dissolve the solidified salts and retain the zirconia beads. The amount of dissolved zirconia is defined as weight difference of the beads before and after the experiment.

After each experiment, a small amount of white powder could be recovered from the dissolved residual salt melt in addition to the zirconia beads. This was done by centrifuging the aqueous solution of residual salts. The powder was dried in a desiccator, which was subsequently evacuated. Afterwards the powder was stepwise calcinated with increments of 100 °C up to 1000 °C. The calcination time for each step was 24 h, following Heiroth and coworkers (2011) who found no significant changes after dwell times longer than 20 h. The composition of the initial powder and those after each heating step were measured by XRD analyses.

In order to determine the compositional evolution of the salt melt, experiments with a pure 20 mmol salt mixture (without zirconia beads) were done for one, two and three days. Afterwards the initial salt mixture and the residual salt melts were analyzed by inductively coupled plasma optical emission spectrometry (ICP-OES).

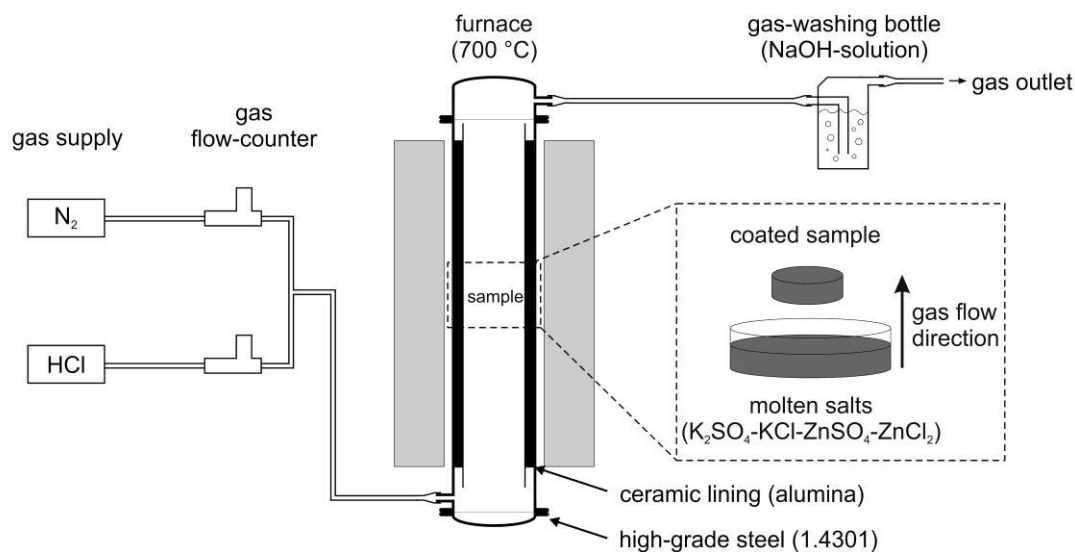


Fig. 3-3: Schematic illustration of the old experimental setup, used for investigations of the interaction between zirconia-coated samples with a synthetic atmosphere of nitrogen and hydrochloric acid, containing gaseous species of a vaporized salt melt.

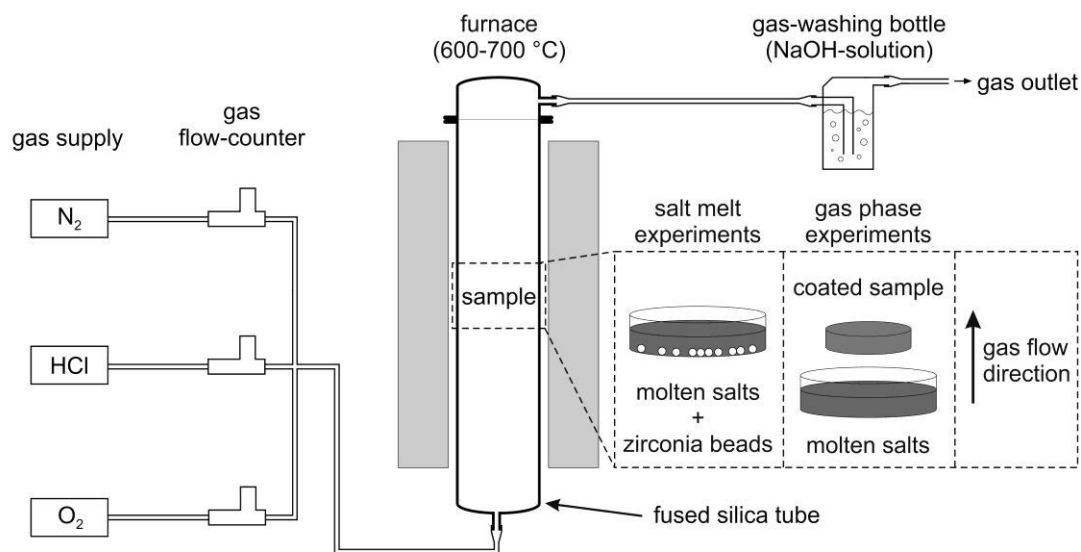


Fig. 3-4: Schematic illustration of the new experimental setup, used for investigations of the interaction between zirconia-coated samples and zirconia beads with various gas phases and salt melts at elevated temperatures. In comparison to the old experimental setup an additional oxygen supply is available and the experiment chamber is fully made of fused silica.

Tab. 3-2: Experimental conditions and porosity values of the YSZ top-coat for lab-scale experiments with steel cylinders, coated with a multilayer coating, under a defined gas-phase.

sample				treatment					porosity
number	substrate	bond-coat	top-coat	temperature	duration	atmosphere	additional salts	addition of other	of the
				(°C)	(days)	(N ₂ /HCl/O ₂) (vol.-%)		compounds together with the salts	top-coat (%)
TS-000	1.2343	Diamalloy 1005	YSZ				untreated reference sample		10.6
TS-029	1.2343	Diamalloy 1005	YSZ	700	3	100 / - / -	---		10.9
TS-043	1.0305	Diamalloy 1005	YSZ	700	3	97 / 2.1 / 0.9	---		10.4
TS-004	1.2343	Diamalloy 1005	YSZ	700	1	98 / 2 / -	KCl, K ₂ SO ₄ , ZnCl ₂ , ZnSO ₄	YSZ powder	10.1
TS-005	1.2343	Diamalloy 1005	YSZ	700	2	98 / 2 / -	KCl, K ₂ SO ₄ , ZnCl ₂ , ZnSO ₄	YSZ powder	7.7
TS-003	1.2343	Diamalloy 1005	YSZ	700	3	98 / 2 / -	KCl, K ₂ SO ₄ , ZnCl ₂ , ZnSO ₄	YSZ powder	6.2
TS-023	1.2343	Diamalloy 1005	YSZ	700	2	98 / 2 / -	KCl, K ₂ SO ₄ , ZnCl ₂ , ZnSO ₄		11.4
TS-027	1.2343	Diamalloy 1005	YSZ	700	3	98 / 2 / -	KCl, K ₂ SO ₄ , ZnCl ₂ , ZnSO ₄	YSZ powder	11.6
TS-031	1.0305	Diamalloy 1005	YSZ	700	2	97 / 2.1 / 0.9	KCl, K ₂ SO ₄ , ZnCl ₂ , ZnSO ₄		10.7 / 5.8
TS-032	1.0305	Diamalloy 1005	YSZ	700	2	97 / 2.55 / 0.45	KCl, K ₂ SO ₄ , ZnCl ₂ , ZnSO ₄		10.3
TS-051	1.0305	Nibasit 625-P	YSZ	500	2	97 / 2.1 / 0.9	KCl, K ₂ SO ₄ , ZnCl ₂ , ZnSO ₄		11.5
TS-055	1.0305	Nibasit 625-P	YSZ	700	2	97 / 2.1 / 0.9	KCl, K ₂ SO ₄ , ZnCl ₂ , ZnSO ₄	YSZ powder	7.0
TS-059	1.0305	Nibasit 625-P	YSZ	700	2	97 / 2.1 / 0.9	KCl, K ₂ SO ₄ , NaCl, Na ₂ SO ₄ , ZnCl ₂ , ZnSO ₄		6.5

Tab. 3-3: Experimental conditions for lab-scale experiments with steel cylinders, coated with a multilayer coating. The samples were impregnated with a saturated salt solution of the mentioned salts and treated at 700 °C for three days.

sample	bond-coat	treatment	
		atmosphere	used salts
		N ₂ / Ar / HCl / SO ₂ / O ₂ (vol.-%)	
TS-037	Diamalloy 1005	- / 97 / 2 / 1 / -	KCl, K ₂ SO ₄ , ZnCl ₂ , ZnSO ₄
TS-038	Diamalloy 1005	- / 97 / 2 / 1 / -	NaCl, Na ₂ SO ₄ , ZnCl ₂ , ZnSO ₄
TS-039	Diamalloy 1005	- / 97 / 2 / 1 / -	KCl, K ₂ SO ₄ , NaCl, Na ₂ SO ₄
TS-040	Nibasit 625-P	97 / - / 2.1 / - / 0.9	KCl, K ₂ SO ₄ , ZnCl ₂ , ZnSO ₄
TS-041	Nibasit 625-P	97 / - / 2.1 / - / 0.9	NaCl, Na ₂ SO ₄ , ZnCl ₂ , ZnSO ₄
TS-042	Nibasit 625-P	97 / - / 2.1 / - / 0.9	KCl, K ₂ SO ₄ , NaCl, Na ₂ SO ₄
TS-044	Nibasit 625-P	air	KCl, K ₂ SO ₄ , ZnCl ₂ , ZnSO ₄
TS-045	Nibasit 625-P	air	NaCl, Na ₂ SO ₄ , ZnCl ₂ , ZnSO ₄
TS-046	Nibasit 625-P	air	KCl, K ₂ SO ₄ , NaCl, Na ₂ SO ₄

Tab. 3-4: Experimental conditions for the investigation of YSZ beads with a salt melt. m_{salts} – amount of the salts; T – temperature.

sample	used salts	m _{salts} (mmol)	T (°C)	duration (days)
SE01		20		1
SE02		20		2
SE03		20		3
SE04		20		4
SE05		30		2
SE06	KCl, K ₂ SO ₄ , ZnCl ₂ , ZnSO ₄	30	600	3
SE07		30		4
SE08		40		2
SE09		40		4
SE10		60		2
SE11		60		4
SE12		40		1
SE13	KCl, K ₂ SO ₄ , ZnCl ₂ , ZnSO ₄	40	700	2
SE14		40		3

3.3 In-situ test facility

The in-situ tests were performed at the WTE plant Zweckverband Müllverwertung Schwandorf (ZMS) in Schwandorf, Bavaria, Germany, consisting of four separate combustion lines. The incinerator has a waste throughput of 12.5 t/h, operating at a live steam pressure of 72 bar and 410 °C. It uses a horizontal grate system to burn municipal and industrial solid waste. Three sample locations at the upper part of the second pass were prepared to accommodate test probes described above. This setup enables the simultaneous operation of three test probes under similar conditions. The test probes extend about 60 cm into the second pass of the WTE plant, facing the flue gas temperature of approximately 700 °C. Two sets of experiments were carried out (Tab. 3-5):

In-situ test at 700 °C:

An uncooled test probe (TP 1) was placed for 14 days in the WTE plant at a flue gas temperature of 700 °C (± 25 °C).

In-situ test at 450 °C:

In order to simulate temperatures which are typically found in membrane walls and superheater tubes, three test probes (TP 2.1, 2.2, 2.3) were cooled by circulating compressed air, to achieve a temperature of 450 °C (± 10 °C). These cooled test probes were placed for 23 days in the WTE plant.

As municipal solid waste is a highly heterogeneous fuel, slightly different chemical conditions of the flue gas in different in-situ experiments should be considered. In general, the following concentrations of gaseous HCl and SO₂ can be assumed (measured values are not available): HCl – 0.09 vol.-%; SO₂ – 0.005 vol.-%.

For the test probes the flue gas-facing side (luv) and the face-away side of the flue gas (lee) were investigated separately. The uncooled test probe exposed an up to 3 cm thick layer of flue gas deposits on the surface as shown in Fig. 3-5. These deposits were analyzed by X-ray fluorescent (XRF) and X-ray diffraction (XRD) analyses at different positions on the luv side (Fig. 3-5, position 1 – 4) and another one on the opposite side (Fig. 3-5, position 5).

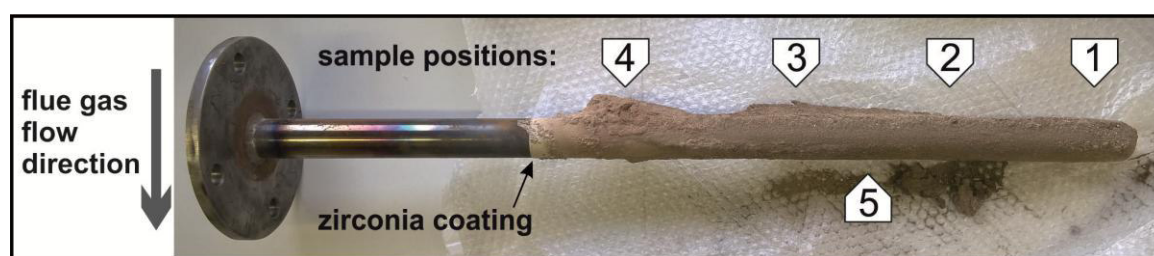


Fig. 3-5: Uncooled test probe with deposits from the flue gas. Modified after Müller and coworkers (2016).

Tab. 3-5: Overview of the in-situ experiments (TP - test probe).

sample	coating	atmosphere	temperature (°C)
TP 1	Nibasit 625-P + YSZ	WTE plant	~700
TP 2.1	Nibasit 625-P + YSZ	WTE plant	~450
TP 2.2	Nibasit 625-P + YSZ	WTE plant	~450
TP 2.3	Nibasit 625-P + YSZ	WTE plant	~450

3.4 Sample preparation and analytical methods

3.4.1 Sample preparation for electron-probe micro-analyses (EPMA)

Coated steel cylinders were cut by half, resulting in a rectangular cross section. One half was used for further analyses of the coating, the other one represents a retained sample, stored in a desiccator. The test probes were cut perpendicular to the coating layer. Both samples, cut steel cylinders and test probes, were embedded in epoxy. YSZ beads were completely embedded in epoxy and ground up to half of the beads in order to enable an investigation of their cross section. Final polishing for all samples was done with diamond paste of 1 μm grain size to obtain a flat surface.

Due to a possible salt content within the pores of the coating, one sample, impregnated with a salt solution, was prepared water free (storage between single preparation steps as far as possible in a desiccator). The investigation of this sample revealed no evidence for the presence of salt within the coating. Therefore, the preparation routine, used for all investigated samples described herein, employs cooling water for the cutting and polishing equipment.

3.4.2 Electron-probe micro-analyzer (EPMA)

For the determination of the porosity, the chemical composition and the chemical distribution within the samples a Cameca SX 100 electron-probe micro-analyzer was used. The EPMA is equipped with a LaB_6 electron source and five wavelength dispersive spectrometers.

Porosity was determined by defining a threshold in visible light (VIS) images for in-situ samples and in backscattered-electron (BSE) images for lab-scale samples, using the ImageJ software. To ensure comparable values, the VIS images were taken in reflected light mode at a 600x magnification. For the BSE images a resolution of 1024 x 768 pixel and a frame time of 15.36 s at a 1000x magnification was chosen (Breitschwerdt 2015). Quantitative analyses and element mappings were done by using an acceleration voltage of 15 keV and a current of 40 nA. The chemical distribution within the coatings was determined by qualitative element mappings. The width of the mapping area was always 60 μm , while the height varied, depending on the coating thickness. A step size of 1 μm per pixel was chosen with a dwell time of 100 ms per pixel. The composition of the YSZ beads was determined by measuring the following elements and X-ray lines (used standards in brackets): Zr L_α (ZrO_2), Y L_α (YIG), Hf L_α (Hf), Al K_α (Al_2O_3).

3.4.3 X-ray diffraction (XRD)

XRD analyses of powder samples were done on a GE X-ray diffractometer (XRD 3003 TT). Sample preparation was done by manual grinding in an agate mortar. Non hygroscopic samples were placed on a SiO_2 zero background sample holder and measured in Bragg-Brentano geometry using $\text{Cu-K}\alpha_1$ radiation. Hygroscopic samples were put in a

sealed glass capillary and measured in Debye-Scherrer geometry by using Mo-K $_{\alpha 1}$ radiation.

For measurements of the solid coating, the polished EPMA sample was used. For the analysis a Bruker D8 discover GADDS system, equipped with a HOPG primary monochromator and a VÅNTEC 2D area detector, was employed at the Department of Applied Mineralogy, University of Tübingen, Germany. Measurement was done by using Co-K $_{\alpha 1}$ radiation.

3.4.4 X-ray fluorescence (XRF)

The bulk analyses of the deposits from the surface of the in-situ test probe were done by ED-XRF analysis on a Philips MagiX Pro. For the determination of the loss on ignition (LOI) the sample was first dried for > 6 h at 110 °C and subsequently ignited at 1050 °C for > 2 h. The major and minor elements were measured using glass beads prepared by fusion of 1 g of ignited sample powder and 9 g of SPECTROMELT A12 (66 % di-lithium tetraborate, 34 % lithium metaborate) in a Panalytical Eagon 2 furnace fusion system at 1150 °C. The percental relative standard deviation (%RSD) for element concentrations > 500 ppm is ~2.4 % and for values < 500 ppm ~7.5 %.

3.4.5 Raman spectroscopy

Raman spectroscopic investigations were done with a Horiba XploRA system, mounted on an Olympus BX10 microscope, operated by the Mineralogical State Collection Munich. The used wavelength was 532 nm. All measurements were done with a 100x long-distance objective. A laser power of 5.5 mW was employed for all analyses.

3.4.6 Fourier transformed infrared (FT-IR) spectroscopy

FT-IR spectroscopic analyses were done with a Bruker EQUINOX55 spectrometer. 1.5 mg of the powdered sample was mixed with 200 mg KBr and pressed into a pellet. The used wavelength was 634 nm.

3.4.7 Weighing

For weighing the zirconia beads, a Sartorius MC210P high precision balance was used. The weighing procedure was repeated five times for each sample, giving an average relative error of 0.002 %.

3.4.8 Inductively coupled plasma optical emission spectrometry (ICP-OES)

The salts were dissolved in 100 ml deionized water to analyze the concentration of potassium, zinc, chlorine and sulfur by ICP-OES at the Centre for Building Materials of the Technische Universität München.

4 Results and discussion of lab-scale experiments

In order to unveil the fundamental processes, leading to the modification of a zirconia coating after exposure to WTE plant conditions, three different scenarios were investigated by lab-scale experiments: (a) zirconia – gas phase interaction, (b) zirconia – gas phase and salt melt interaction and (c) zirconia – salt melt interaction. For the gas phase experiments, zirconia-coated steel cylinders were treated under various gas phases at temperatures ranging from 500 – 700 °C (see Tab. 3-2). For an investigation of the interaction of zirconia with gas phases together with a salt melt, zirconia-coated steel cylinders were impregnated with a saturated salt solution and afterwards heat treated under various gas phases at a temperature of 700 °C (see Tab. 3-3). To investigate the interaction of zirconia with a salt melt, zirconia beads were placed in a crucible together with the salt melt and heat treated under a $N_2 - HCl - O_2$ atmosphere (see Tab. 3-4).

4.1 Gas phase experiments

For the first experiments (TS-003 – TS-005), the old experimental setup was employed, in order to reconstruct prior experiments of Fehr and coworkers (2012) and Ye (2016). This old furnace consisted of a steel housing with an alumina-lined experimental chamber, which was purged with an atmosphere of $N_2 - 2 \text{ vol.-% } HCl$ for the experiments. Further experiments were done within the new experimental setup, which consists of an experimental chamber of fused silica and an additional oxygen gas supply (see chapter 3.2.1). Sections of the treated samples, summarized in Tab. 3-2, were characterized by BSE image analysis and element mappings. The presentation of the chemical distribution within the element mappings is structured as follows: (a) salt components (zinc, sodium / potassium, chlorine, sulfur) (for treated samples only), (b) top-coat (zirconium, yttrium), (c) bond-coat (chromium, nickel) and (d) steel substrate (iron). The oxygen was analyzed too in order to identify oxide compounds.

As reference, an untreated sample (TS-000) was characterized first:

The microstructure of an untreated APS-applied multilayer coating is shown in Fig. 4-1. The ceramic top-coat consists of homogeneously distributed globular and interlamellar pores. The porosity was determined to be 10.6 %. It is within the range of typical porosity values between 10.0 and 13.2 % obtained by image analysis of BSE images of similar untreated samples (Breitschwerdt 2015).

The element distribution within the untreated sample is shown in Fig. 4-2. The ceramic top-coat reveals a homogeneous distribution of zirconium and also of yttrium. In some parts an enrichment of yttrium is visible. The bond-coat generally consists of mainly nickel and chromium, as major components of Inconel 625. As visible in Fig. 4-2, the distribution of chromium and nickel is heterogeneous. Enrichments of chromium correspond with the presence of oxygen and the absence of nickel, enclosing homogeneous sub-areas consisting of chromium and nickel, but no oxygen (Fig. 4-3). The steel substrate shows a homogeneous distribution of iron. The transition between top- and

bond-coat as well as bond-coat and steel substrate is characterized by a sharp, but irregular line, with local Al_2O_3 enrichments.

Résumé

The differences of the yttrium distribution within the top-coat can result from the thermal spray deposition process or from an inhomogeneous feedstock. Mauer and coworkers (2012) observed a loss of lanthanum or gadolinium during the deposition of lanthanum (gadolinium) zirconates via thermal spraying, depending on the spray parameters. A similar process can occur for yttrium during the thermal spray deposition of YSZ. A XRD analysis of the feedstock revealed tetragonal zirconia as main phase containing a small amount of monoclinic zirconia, which is obviously caused by a lower amount of yttria. Since XRD patterns of cubic and tetragonal zirconia are very similar, the presence of minor amounts of cubic zirconia (caused by an increased yttria content) cannot be proven. Areas of homogeneously distributed chromium and nickel without oxygen represent metallic Inconel 625 of the bond-coat. These regions are enclosed by thin layers of chromium and oxygen, indicating the presence of chromium oxide (Cr_2O_3). The formation of these thin Cr_2O_3 layers originates from the atmospheric plasma spray process (Deshpande et al. 2006). The oxidation can happen in flight of the particles from the gun to the substrate or at the surface of the solidifying or solidified splat. As a consequence of this process, a Cr_2O_3 surface layer can be expected at the top of the bond-coat. Notably, no Cr_2O_3 layer is observable at the transition zone between bond- and top-coat (Fig. 4-3). This can be explained by the production procedure, since each surface was corundum blasted prior to the following coating step. Hence the hard corundum grains easily remove the former Cr_2O_3 surface layer. The observable Al_2O_3 grains can also be seen as relicts from the production process of the coating. Due to the hardness of Al_2O_3 in comparison to the ductile metallic substrates, some Al_2O_3 grains attach to the substrate and are preserved.

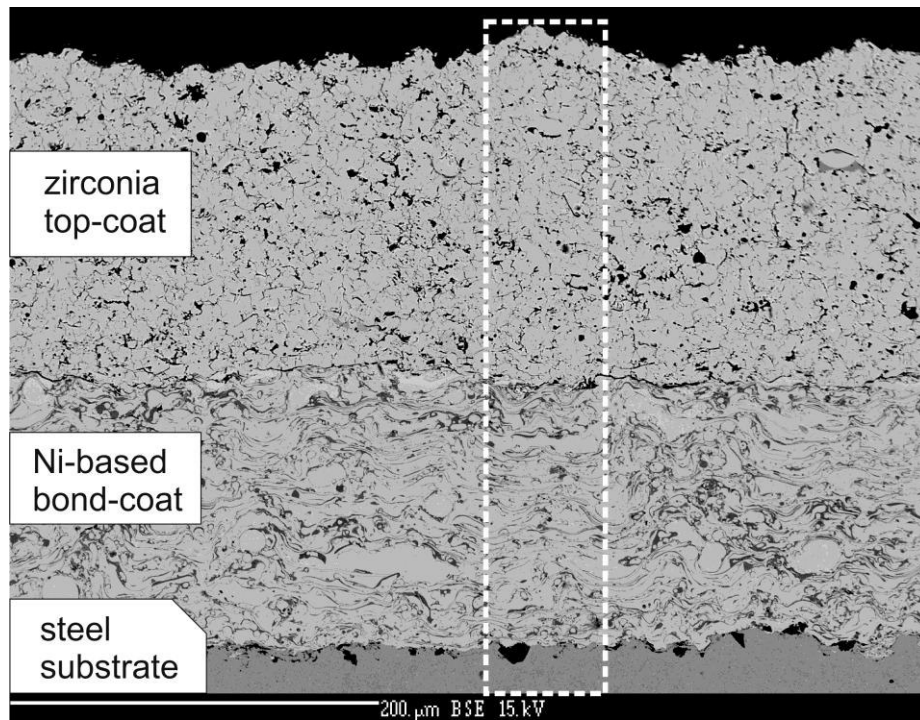


Fig. 4-1: Back-scattered electron (BSE) image of an untreated sample (TS-000). The marked area (dotted line) represents the region of the element mapping.

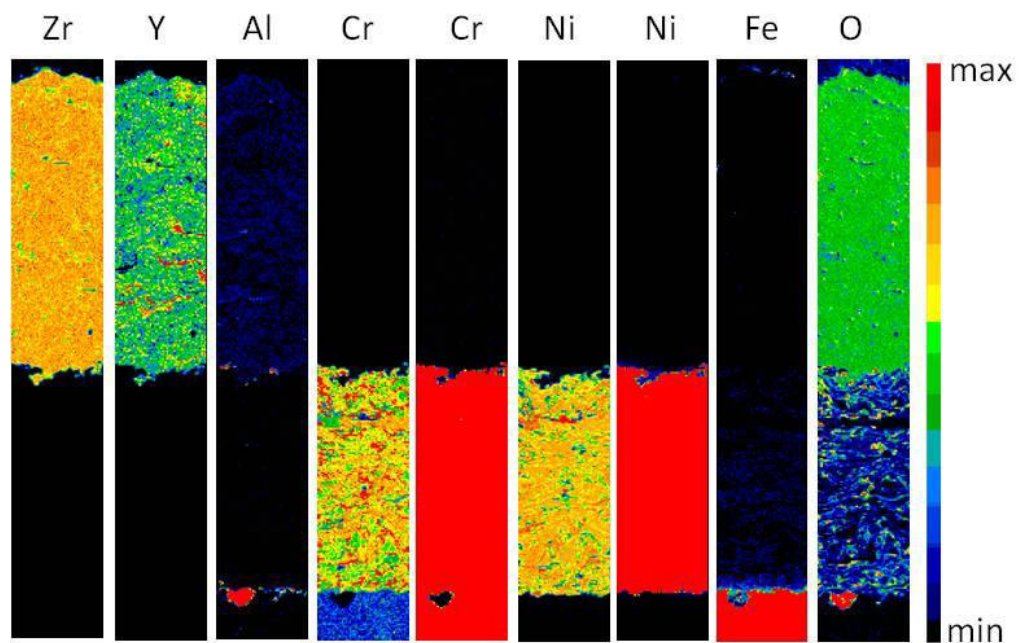


Fig. 4-2: Element mapping of an untreated sample (TS-000) for zirconium, yttrium, aluminum, chromium, nickel, iron and oxygen. Chromium and nickel are shown in two different scales (left: large range; right: small range) in order to visualize also minor amounts. Base length of each mapping is 60 µm.

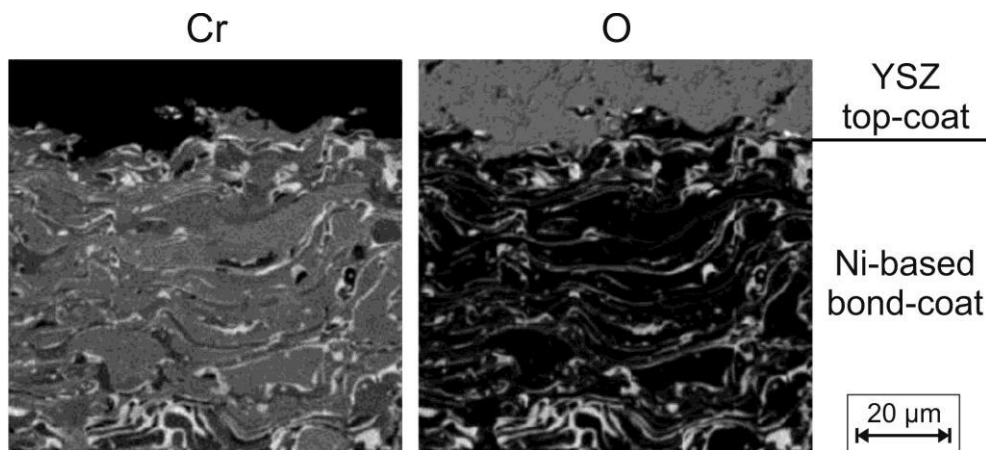


Fig. 4-3: Element mapping of the transition zone between bond-coat and top-coat for chromium and oxygen of an untreated sample (TS-000).

4.1.1 Experiments with the old experimental setup

In order to investigate the temporal evolution of the densification process, three experiments were performed with one, two and three days of reaction time (TS-004, TS-005 and TS-003, respectively) (Tab. 3-2). An equimolar mixture of $\text{KCl-K}_2\text{SO}_4\text{-ZnCl}_2\text{-ZnSO}_4$ was placed in a fused silica crucible together with YSZ powder. The atmosphere consisted of $\text{N}_2 - 2 \text{ vol.-% HCl}$ at a temperature of 700°C .

After the two- and three-day experiments the surface of the samples TS-005 and TS-003 was partially green colored (Fig. 4-4).



Fig. 4-4: Photographs showing the samples treated for two (TS-005) and three (TS-003) days. The samples are cut by half. Sample diameter is 2 cm.

Fig. 4-5 shows the development of the treated samples in comparison to the untreated sample (TS-000). After one day the porosity of the top-coat of sample TS-004 was 10.1 %, while after two days in sample TS-005 a separation into two layers with different porosity is observable: An outer layer with a porosity of 9.6 % and an inner layer with a porosity of 7.7 %. After three days the porosity of the whole top-coat of sample TS-003 decreased further to 6.2 %, accompanied by the formation of vertical cracks.

The amount of zinc, potassium, chlorine and sulfur within the coating (Fig. 4-6) is negligible after one (TS-004) and two days (TS-005), indicating the absence of salt components. After three days of treatment (TS-003) the combined occurrence of potassium and chlorine is observable, predominantly within the bond-coat, pointing to the presence of KCl . Only minor amounts of sulfur and zinc can be observed. Zirconium and

yttrium show no change, even for the two day sample (TS-005), which shows a separation into two regions with different porosity within the top-coat. The main elements of the bond-coat (chromium and nickel) show no changes after one and two days of treatment. After three days, a small nickel-enriched layer is observable at the bond-coat – steel substrate interface. In contrast, chromium is enriched within and on top of the ceramic top-coat after three days. Iron shows minor enrichments on the surface of the top-coat and a strong enrichment within the bond-coat after three days of treatment. Comparable to untreated samples, also some Al_2O_3 enrichments can be found at the transition zones between bond-coat – top-coat and bond-coat – steel substrate

Due to the high amount of zirconium oxide within the top-coat, the determination of additional oxide compounds within this area on the basis of the oxygen distribution is difficult. Due to the excitation volume of the electron beam (in the range of several micrometers) it is not possible to prove the presence of oxides smaller than $3\text{ }\mu\text{m}$, e.g. Cr_2O_3 grains. For bigger grains this differentiation can be done, as visible for the chromium enrichments of the three-day treated sample, which are accompanied by an increased value of oxygen (red areas in the top-coat of the oxygen mapping - Fig. 4-6). Based on this observation it can be concluded, that the observable chromium enrichments within the top-coat represent Cr_2O_3 .

Résumé

The observed results partially conform but also contradict observations of prior studies of Fehr and coworkers (2012) and Ye (2016). An overview of similarities and differences is given in Tab. 4-1.

No densification is observable after one day of treatment, while after two days a separation into two layers (undensified outer layer, densified inner layer) is visible. This formation of a densified layer at the bottom of the ceramic top-coat and an unaffected outer layer confirms the results of Fehr and coworkers (2012) and Ye (2016), who described a densification, starting from the top-coat - bond-coat interface outward. For both prior studies (Fehr et al. 2012 and Ye 2016), YSZ powder was added to the salt mixture. It was assumed, that highly volatile ZrCl_x species were formed in-situ, which were able to penetrate the ceramic top-coat. Fehr and coworkers (2012) further described the formation of CrCl_x species at the top-coat – bond-coat interface through an interaction of gaseous HCl with the bond-coat. A reduction of gaseous sulfate compounds within the top-coat was supposed to represent a possible source for the recrystallization of chromium and / or zirconium oxides. While Fehr and coworkers (2012) ascribed the densification of the top-coat to the formation of Cr_2O_3 and ZrO_2 in open pores of the top-coat, Ye (2016) described only a recrystallization of ZrO_2 .

Since the densified bottom layer in this work consists of pure YSZ (see Fig. 4-6), it can be described as densified zirconia. A thickness of approximately $120\text{ }\mu\text{m}$ for this densified layer gives a densification rate of $\sim 120\text{ }\mu\text{m/day}$, according to the value of $130\text{ }\mu\text{m/day}$ determined by Fehr and coworkers (2012). After three days, the whole top-coat exhibits a porosity of 6.2 %. On the basis of a top-coat thickness of $\sim 230\text{ }\mu\text{m}$, a continuous densification rate of $\sim 120\text{ }\mu\text{m/day}$ can be assumed. Additionally, the

formation of vertical cracks is visible within the top-coat after three days (see Fig. 4-5). The growth of secondary oxides can cause an increased mechanical stress within the ceramic matrix, leading to the observable cracks. Fehr and coworkers (2012) and Ye (2016) described the growth of a newly formed Cr_2O_3 layer with minor amounts of Al_2O_3 between bond- and top-coat, designated as thermally grown oxides (TGO). In this study, no continuous Cr_2O_3 layer can be observed, but secondary Cr_2O_3 particles within the top-coat (Fig. 4-6), partially influencing the observable reduced porosity, as already described by Fehr and coworkers (2012). The bond-coat – top-coat border appears rather rough with increasing experimental duration, showing fringes of chromium enrichments reaching into the ceramic top-coat. The Al_2O_3 enrichments can be seen as relicts from the production process of the coating. Thus, it is more unlikely, that the aluminum evolved out of the bond-coat as described in prior studies (Fehr et al. 2012, Ye 2016). The minor amounts of aluminum within the top-coat, tracing the splat morphology, were deliberately added during the production process of the feedstock powder to improve mechanical properties of the zirconia ceramic.

The common occurrence of potassium and chlorine indicates the presence of KCl salt. If no potassium or zinc correlates with the appearance of chlorine it can be a pore, filled with epoxy (contains chlorine) or a solid metal chloride. The proof of the latter is difficult for possible metal chlorides within the metallic bond-coat, since the assignment of specific metals to the chlorine is not unequivocally feasible.

The presence of Cr_2O_3 within the outer parts of the ceramic top-coat correlates with the green color of the samples. An investigation of the furnace revealed a corrosion attack of the steel housing, which was in contact with the $\text{N}_2\text{-HCl}$ gas mix. This suggests a mobilization of the chromium from the steel as CrCl_x , which entered the sample pores and recrystallized as Cr_2O_3 . Therefore, a new experimental setup with a fused silica experiment chamber was built, in order to guarantee controlled experiment conditions.

Tab. 4-1: Comparison of observations regarding the densification process between prior studies of Fehr and coworkers (2012) and Ye (2016) with results from this study.

subject	prior studies	this study
densification	ZrO_2 and Cr_2O_3 (Fehr et al. 2012) ZrO_2 (Ye 2016)	ZrO_2 and Cr_2O_3 (TS-003) / ZrO_2 (TS-005)
densification onset	no information	after 1 day
densification rate	130 $\mu\text{m/day}$	~120 $\mu\text{m/day}$
TGO layer	Cr_2O_3 and Al_2O_3	no TGO layer observable

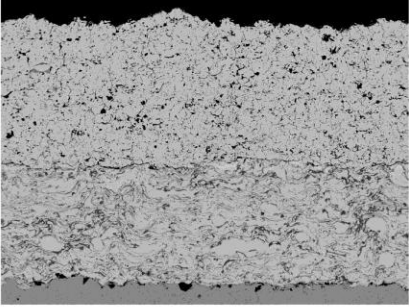
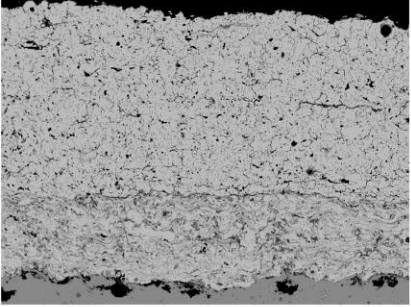
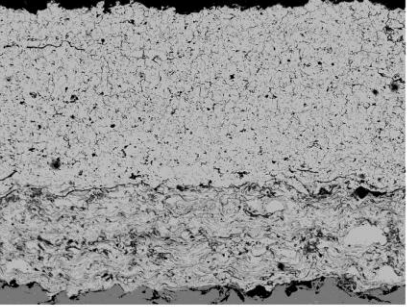
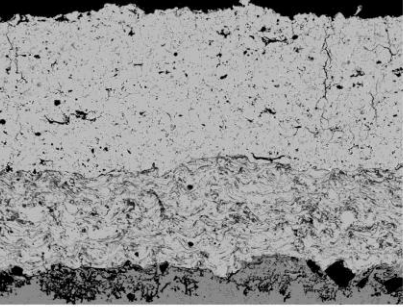
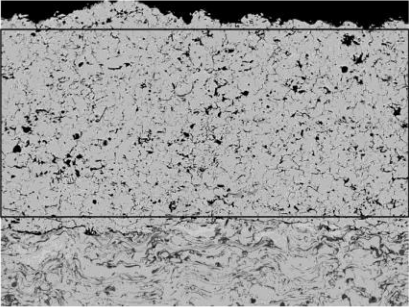
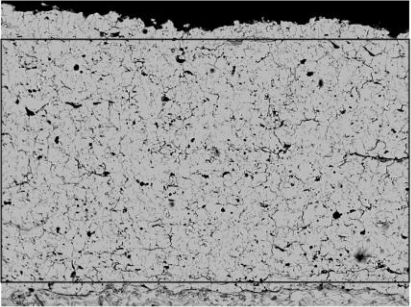
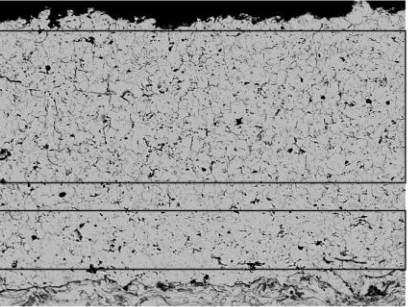
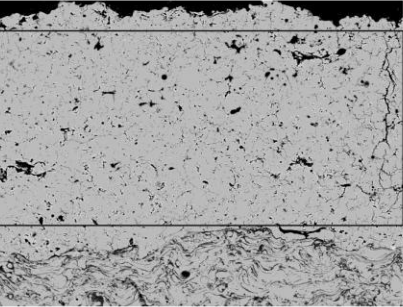
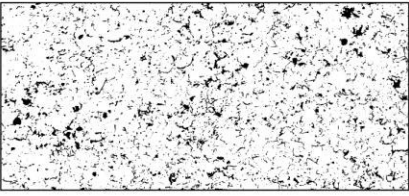
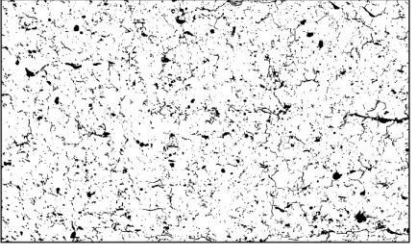
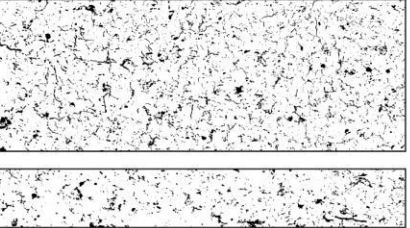
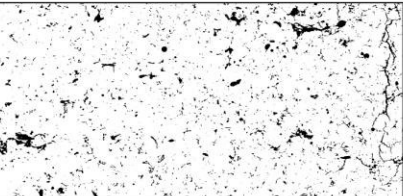
	untreated	1 day	2 days	3 days
BSE (base length 500 μ m)				
BSE (base length 337 μ m)				
porosity	 10.6 %	 10.1 %	 top: 9.6 % bottom: 7.7 %	 6.2 %

Fig. 4-5: Back-scattered electron (BSE) images of an untreated sample (TS-000) in comparison with samples TS-004 (1 day), TS-005 (2 days) and TS-003 (3 days). The porosity determination is based on a threshold analysis of the marked area within the BSE image with a base length of 337 μ m.

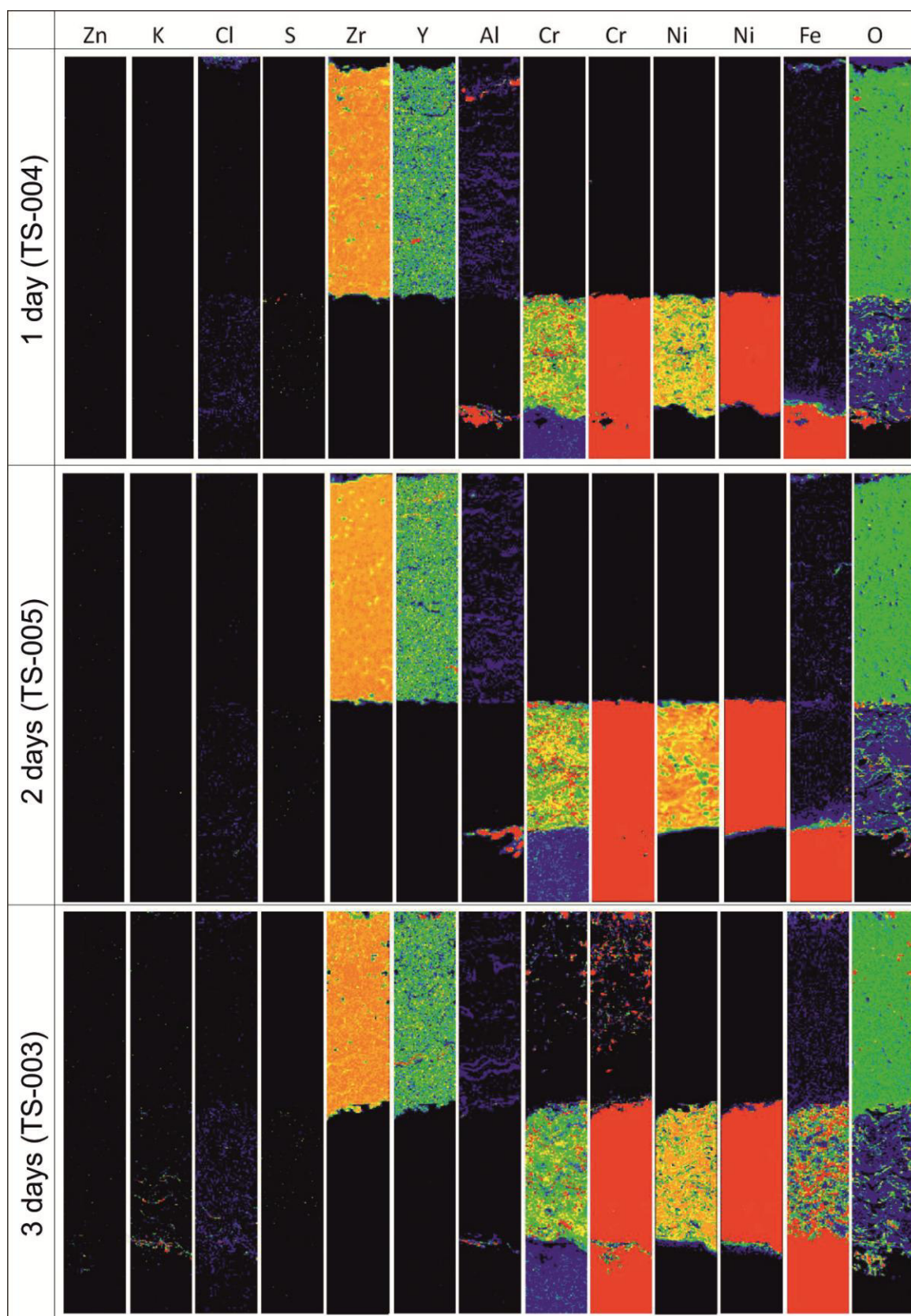


Fig. 4-6: Qualitative element mappings from samples TS-004 (1 day), TS-005 (2 days) and TS-003 (3 days). Base length of each mapping is 60 μm . Chromium and nickel are shown in two different scales: Cr 5-250 counts; Ni 5-1700 (left); Cr 5-25; Ni 5-170 counts (right). The mapping areas of the three samples (1, 2 and 3 days) represent the central part of the BSE images of each sample in Fig. 4-5.

4.1.2 Experiments with the new experimental setup

Parts of this chapter are modified after Müller and coworkers (2016).

The BSE images, together with the porosity value of all experiments done within the new experimental setup are shown in Fig. 4-7 and Fig. 4-8. The first experiments with the new experimental setup (TS-023, TS-027) were done under similar conditions (700 °C, N₂ – 2 vol.-% HCl) like the experiments conducted with the old experimental setup (TS-003, 004, 005), in order to evaluate the influence of the experimental setup (see Tab. 3-2). Generally, no sample treated within the new experimental setup showed a green color of the coating surface.

Experiment TS-027 corresponds with experiment TS-003 (salts + YSZ), while TS-023 was treated without an addition of YSZ into the gas flow. The evaluation of BSE images from TS-027 and TS-023 gives a porosity of 11.6 % and 11.4 %, respectively (Fig. 4-7). In contrast to experiments within the old experimental setup, the porosity was not reduced. In particular, experiment TS-003 (porosity of 6.2 %) could not be reproduced by using the new experimental setup (TS-027 – porosity of 11.6 %), as summarized in Tab. 4-2. No Cr₂O₃ can be found within the top-coat (Fig. 4-9) and no densification of the top-coat can be observed for TS-027.

Tab. 4-2: Comparison of TS-003 (old experimental setup) and TS-027 (new experimental setup).

sample	TS-003	TS-027
porosity (%)	6.2	11.6
secondary phases in top-coat	Cr-oxides	---
coloring of the top-coat surface	dark green	white

Further experiments employed additional oxygen within the gas mixture by using the same salt composition of potassium and zinc chlorides and sulfates (TS-031, 032, 051, 055) or a salt mixture of sodium, potassium and zinc chlorides and sulfates (TS-059).

The experimental conditions for TS-031 are comparable with those from experiment TS-023, except the additional introduction of 0.9 vol.-% O₂ together with a slightly higher amount of HCl (2.1 vol.-%). This treatment led to the formation of two distinct regions with different porosity within the top-coat of sample TS-031. The upper (outer) layer exhibits a porosity of 10.7 %, in contrast to 5.8 % of the lower (inner) part of the top-coat (Fig. 4-7). For the same gas mixture, but at 500 °C (TS-051), no densification is observable. A reduction of the oxygen content within the atmosphere to 0.45 vol.-% in combination with an increased HCl amount of 2.55 vol.-% (TS-032) also led to no densification.

In contrast, a densification of the whole top-coat was achieved by (a) an addition of YSZ powder to the salt mixture (TS-055) and (b) by using a salt mixture of sodium, potassium and zinc chlorides and sulfates (TS-059), both under an oxygen-bearing atmosphere.

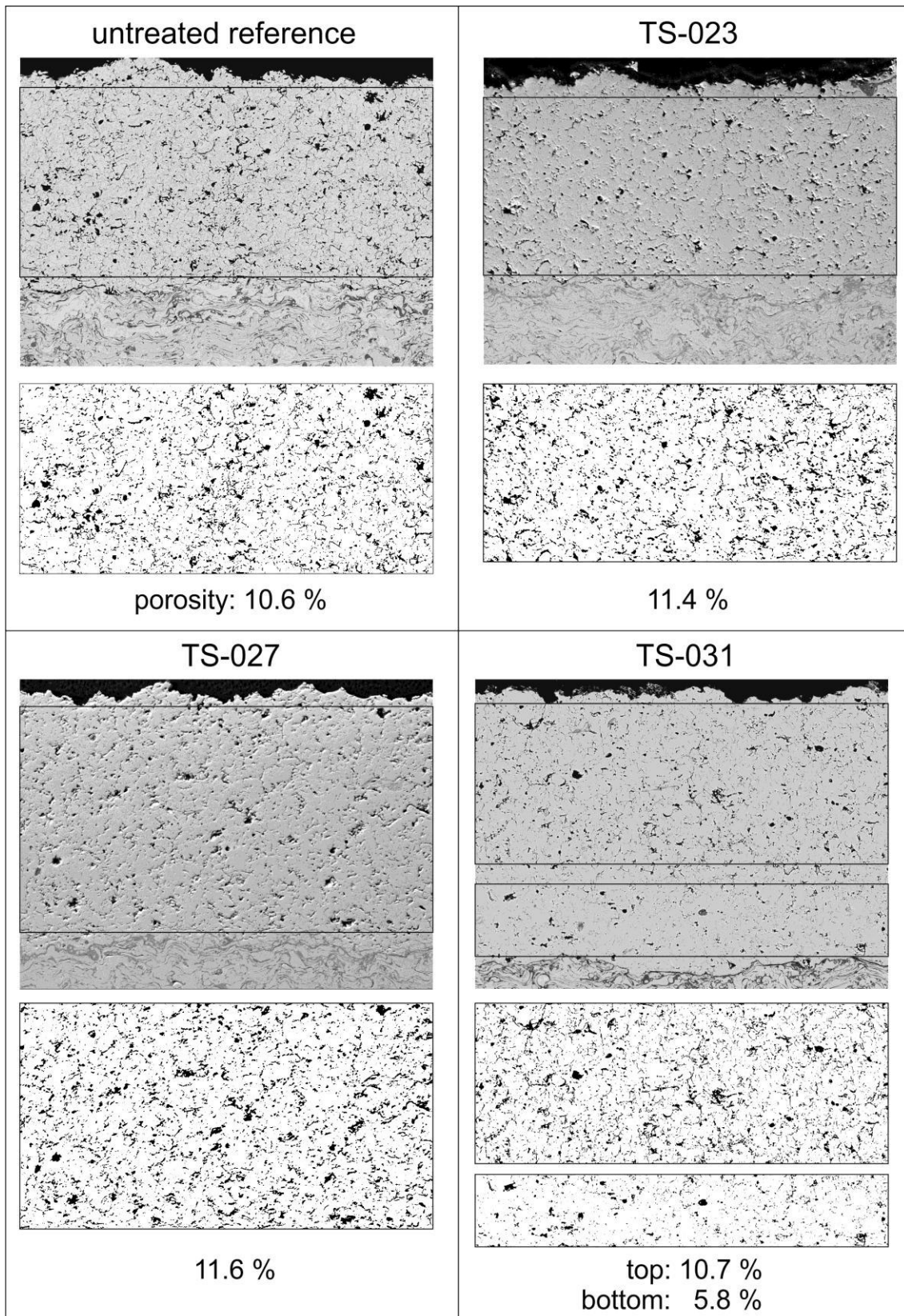


Fig. 4-7: BSE images of samples TS-023, TS-027 and TS-031 in combination with threshold images in order to determine the porosity of each specimen. As reference an untreated sample is shown. The base length of each image is 337 μm .

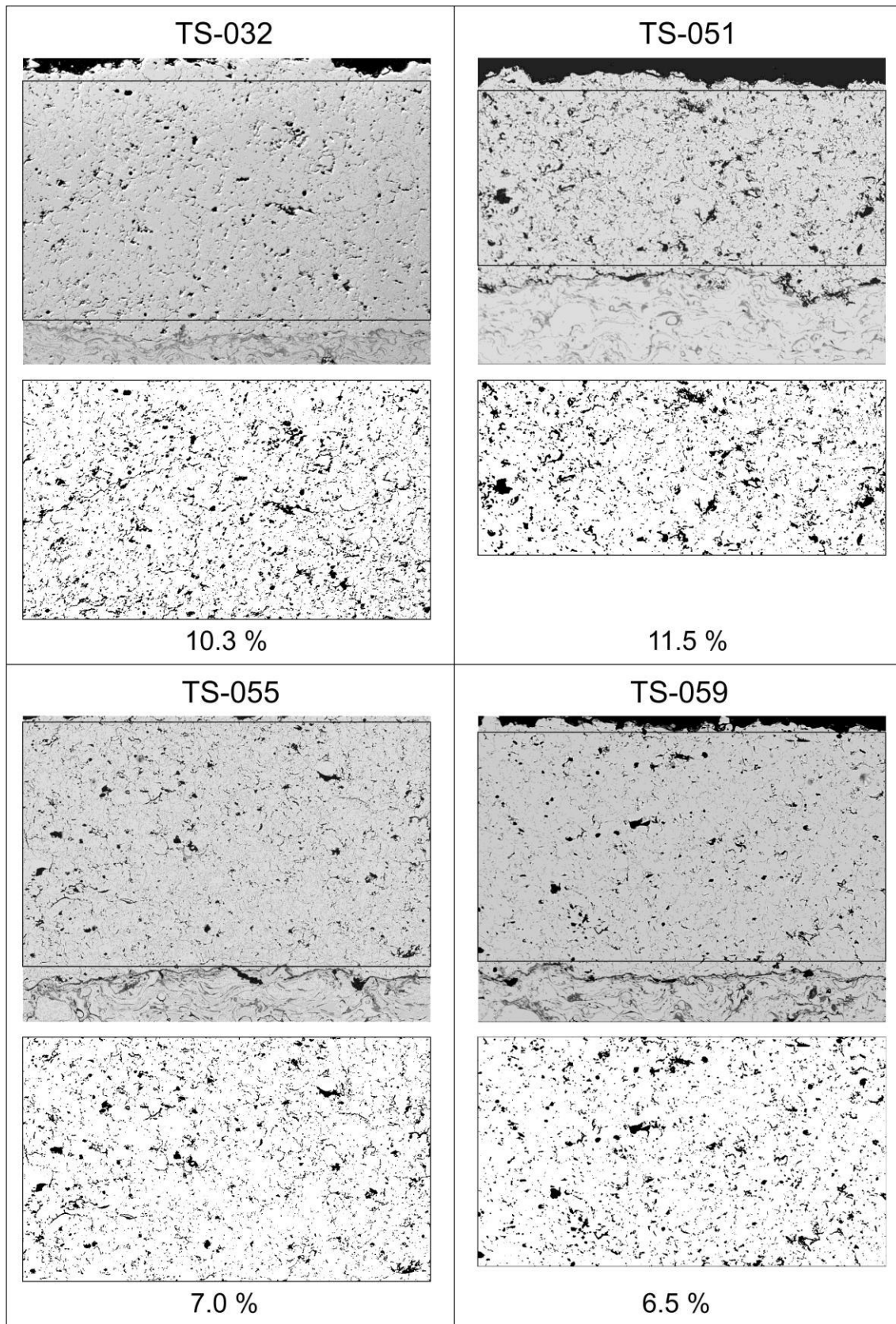


Fig. 4-8: BSE images of samples TS-032, TS-051, TS-055 and TS-059 in combination with threshold images in order to determine the porosity of each specimen. The base length of each image is 337 μm .

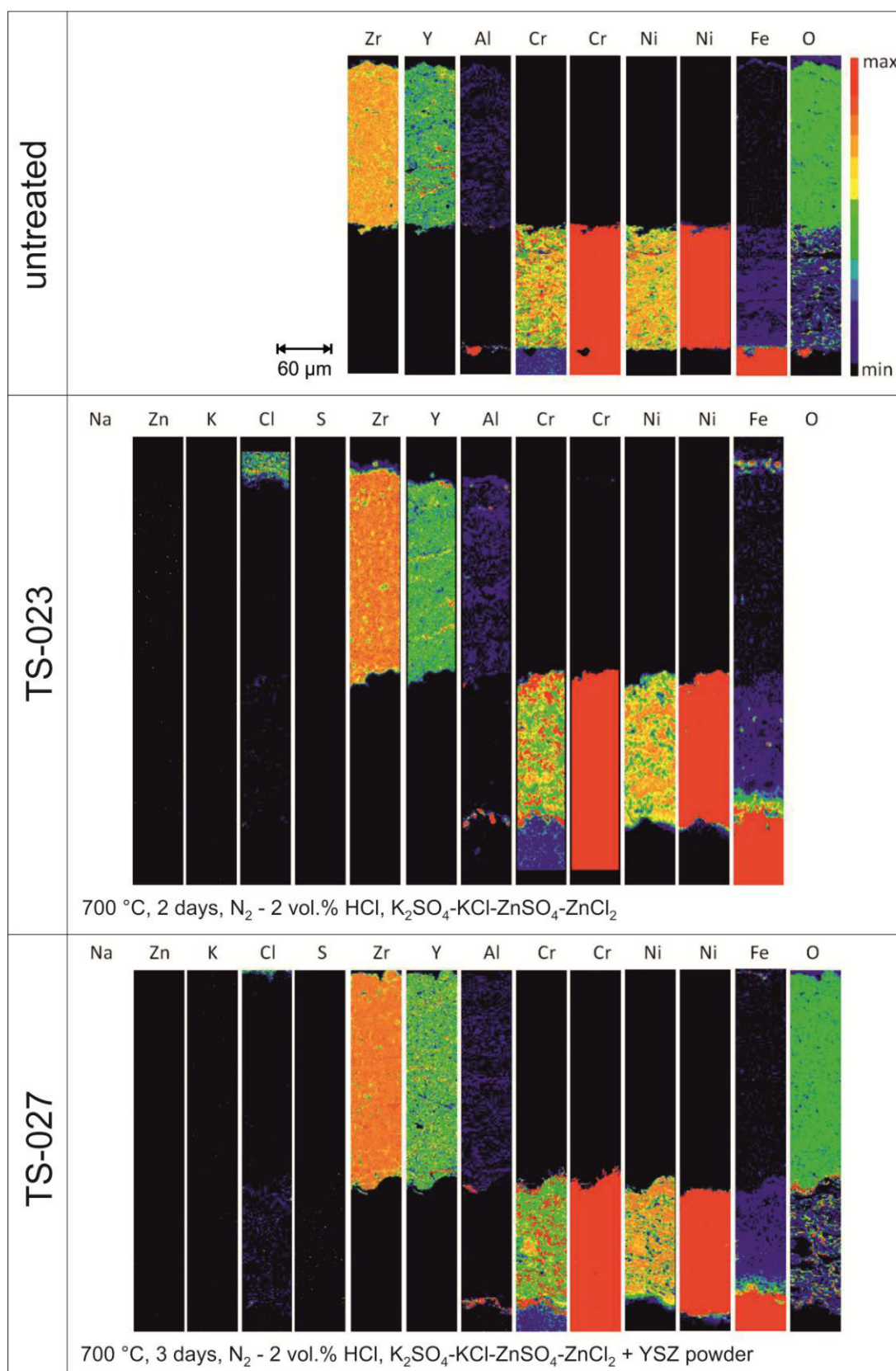


Fig. 4-9: Element mappings for zinc, potassium, sulfur, zirconium, yttrium, aluminum, chromium, nickel, iron and oxygen (as available) of an untreated sample, TS-023 and TS-027. Chromium and nickel are shown in two different scales: Cr 5-250 counts; Ni 5-1700 (left); Cr 5-25; Ni 5-170 counts (right).

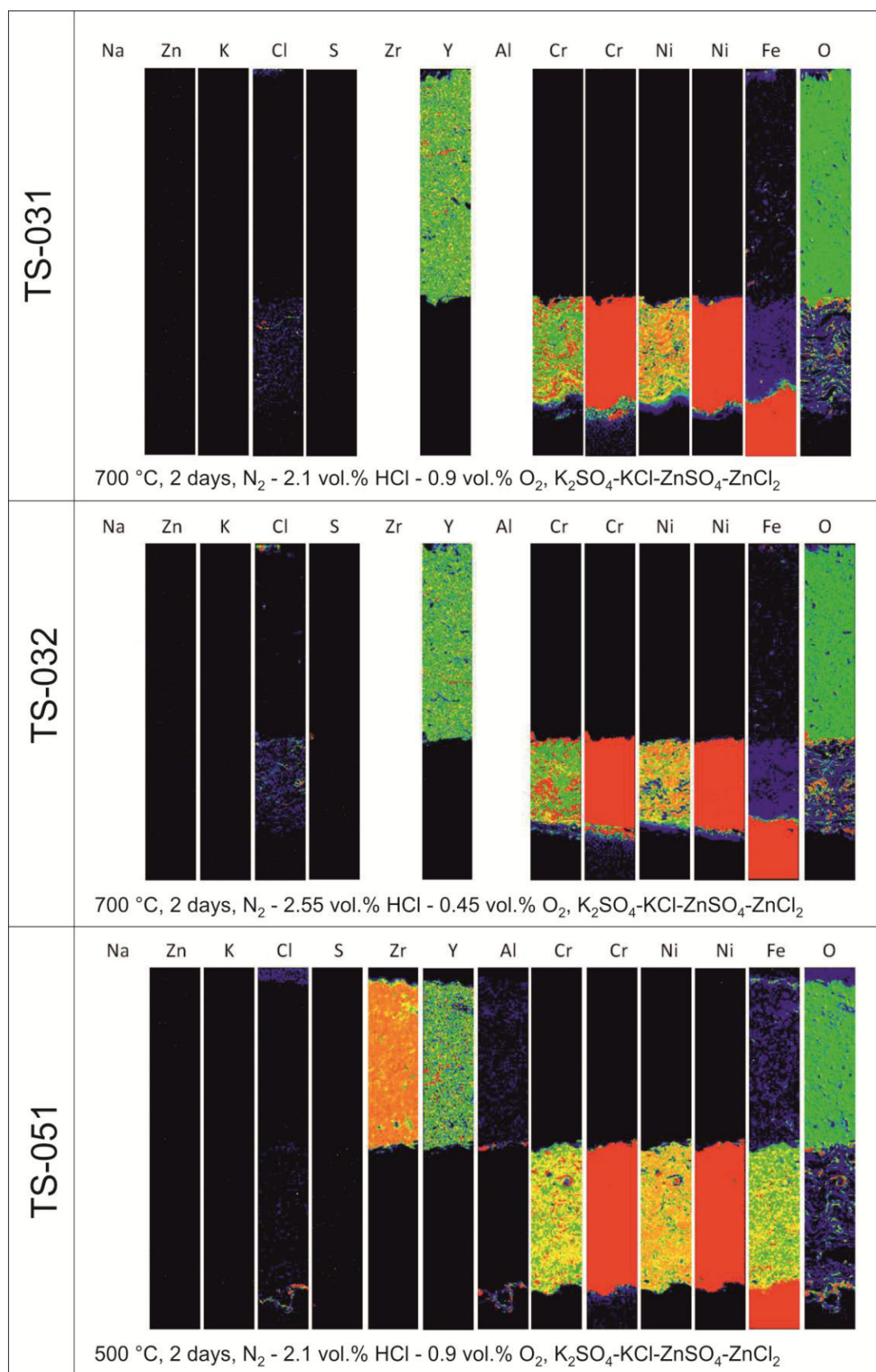


Fig. 4-10: Element mappings for zinc, potassium, sulfur, zirconium, yttrium, aluminum, chromium, nickel, iron and oxygen (as available) of TS-031, TS-032 and TS-051. Chromium and nickel are shown in two different scales: Cr 5-250 counts; Ni 5-1700 (left); Cr 5-25; Ni 5-170 counts (right).

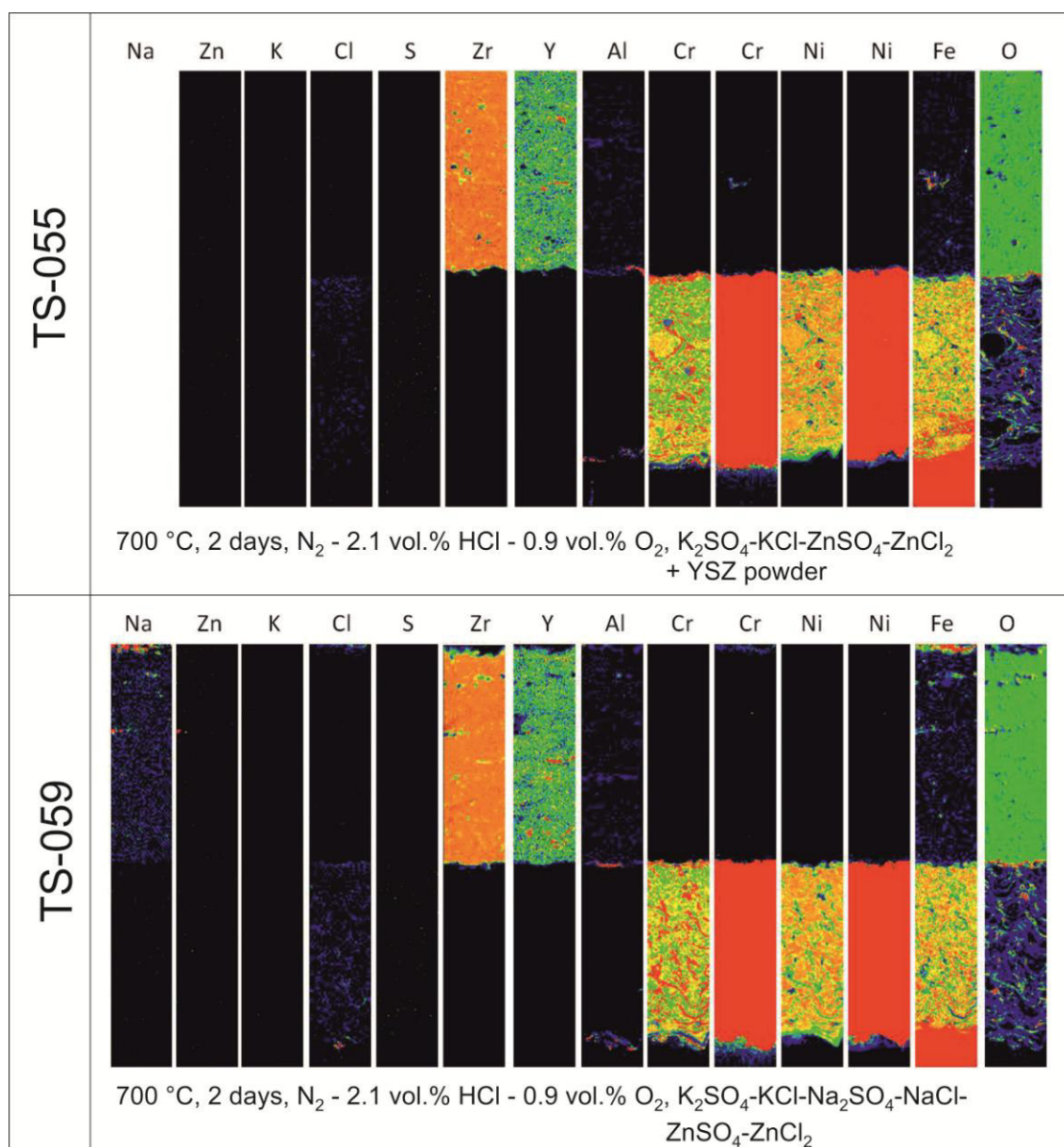


Fig. 4-11: Element mappings for sodium, zinc, potassium, sulfur, zirconium, yttrium, aluminum, chromium, nickel, iron and oxygen (as available) of TS-055 and TS-059. Chromium and nickel are shown in two different scales: Cr 5-250 counts; Ni 5-1700 (left); Cr 5-25; Ni 5-170 counts (right).

The element mappings of all treated samples are shown in Fig. 4-9, Fig. 4-10 and Fig. 4-11. An overview of the results of the experiments within the new experimental setup is given in Tab. 4-3. Chlorine can be found within the bond-coat of all samples: TS-031, TS-032 and TS-059 exhibit a stronger enrichment of chlorine, within sample TS-051 it is predominantly enriched between bond-coat and steel substrate. The other samples only show a small enrichment of chlorine. TS-059 shows minor amounts of zinc and small amounts of homogeneously distributed sodium within the ceramic top-coat. The presence of sulfur is restricted to the interface between top- and bond-coat, as visible for TS-032. Based on the X-ray wavelength differences between sulfide and sulfate compounds it can unambiguously be identified as sulfide by EPMA analysis (Essene et al. 2006). The combined occurrence of sulfur and chromium within the element mappings points to the presence of a chromium sulfide. Potassium cannot be found within the samples. The occurrence of zirconium, yttrium and aluminum is comparable to untreated samples and samples treated within the old experimental setup. Also for the densified samples, no change in the zirconium distribution is visible.

For the comparison of the elements of the bond-coat (chromium, nickel, iron), it needs to be considered that for samples TS-023, 027, 031 and 032 Diamalloy 1005 (2.5 wt.-% Fe) was used and Nibasit 625-P (4.0 wt.-% Fe) for TS-051, 055 and 059. Regarding the chromium distribution it becomes visible, that Diamalloy 1005 appears more heterogeneous in contrast to Nibasit 625-P. The Diamalloy 1005 samples show a more pronounced separation between Cr-rich and Cr-poor regions. All samples, except TS-051, show a newly formed Cr_2O_3 layer between top- and bond-coat, visible as a continuous dark grey line within the BSE images (Fig. 4-7, Fig. 4-8). A detailed element mapping of this Cr_2O_3 layer is shown in Fig. 4-12 for sample TS-031. Chromium as well as nickel show a small enrichment within the steel substrate, close to the bond-coat and vice versa for iron, which is enriched within the bond-coat. A significant iron enrichment is observable within sample TS-055. The general difference of the iron concentration within the Diamalloy 1005 and Nibasit 625-P samples is based on the different iron amounts of both feed stock powders as mentioned above. Additionally, minor amounts of iron can be found within the top-coat of all samples.

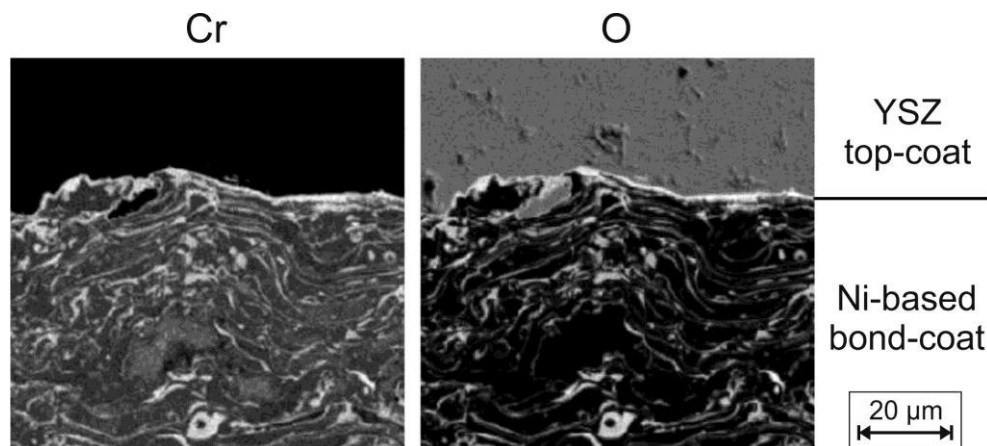


Fig. 4-12: Element mapping of the transition zone between bond coat and top coat for chromium and oxygen of a treated sample (TS-031).

Tab. 4-3: Overview of the experiments within the new experimental setup. For the top-coat (TC), bond-coat (BC) and the steel substrate, artificial elements and their amounts are given (↑ - high; → - moderate; ↓ - low amount).

sample	TS-023	TS-027	TS-031	TS-032	TS-051	TS-055	TS-059
experimental conditions:							
temperature	700	700	700	700	500	700	700
atmosphere (N ₂ /HCl/O ₂)	98 / 2 / 0	98 / 2 / 0	97 / 2.1 / 0.9	97 / 2.55 / 0.45	97 / 2.1 / 0.9	97 / 2.1 / 0.9	97 / 2.1 / 0.9
salts			KCl, K ₂ SO ₄ , ZnCl ₂ , ZnSO ₄				+ NaCl, Na ₂ SO ₄
		+ YSZ powder				+ YSZ powder	
porosity of the TC	11.4	11.6	10.7 / 5.8	10.3	11.5	7.0	6.5
TC	Fe ↑	Fe ↓	Fe ↓	Fe ↓	Fe ↑	Fe →	Fe ↑
	Zn ↓						Zn ↓
							Na ↑
newly formed Cr ₂ O ₃ layer	yes	yes	yes	yes	no	yes	yes
BC	Cl ↓	Cl →	Cl ↑	Cl ↑	Cl →	Cl ↓	Cl ↑
	Fe ↑	Fe ↑	Fe →	Fe →	Fe ↓ ¹	Fe ↑ ¹	Fe → ¹
steel	Ni →	Ni →	Ni ↑	Ni ↑	Ni ↓	Ni →	Ni →
	Cr ↑ ²	Cr ↑ ²	Cr ↑ ²	Cr ↑	Cr →	Cr →	Cr →

¹ - BC: Nibasit 625-P

² - high-grade steel

Résumé

The appearance of the BSE image of TS-031 is similar to TS-005 (old experimental setup). Both samples show a partially densified ceramic top-coat at the border to the underlying bond-coat. Element mappings of both samples (Fig. 4-6, Fig. 4-10) and XRD analysis of the densified layer of TS-031 (Fig. 4-13) prove the presence of pure YSZ, since only t-ZrO₂ peaks appear in the XRD pattern. TS-055 and TS-059 were also treated for two days, but the whole top-coat exhibits a reduced porosity. The addition of YSZ powder into the salt mixture (TS-055) leads to an enhanced densification of the top-coat. The enhanced densification of the ceramic top-coat by using additional sodium salts (TS-059) is notable. This observation correlates with results from whole rock analyses of sanidine-bearing volcanic rocks from Laacher See, Germany, done by Donjá Aßbichler (Aßbichler et al. 2017): These rocks show a significant enrichment of zirconium minerals, like baddeleyite (ZrO₂). A positive correlation between the content of zirconium and sodium (Fig. 4-14) suggests an enhanced mobilization of zirconium in the presence of sodium.

The formation of the newly formed Cr₂O₃ layers between bond- and top-coat for samples treated at 700 °C will be discussed in the following chapter 4.2.

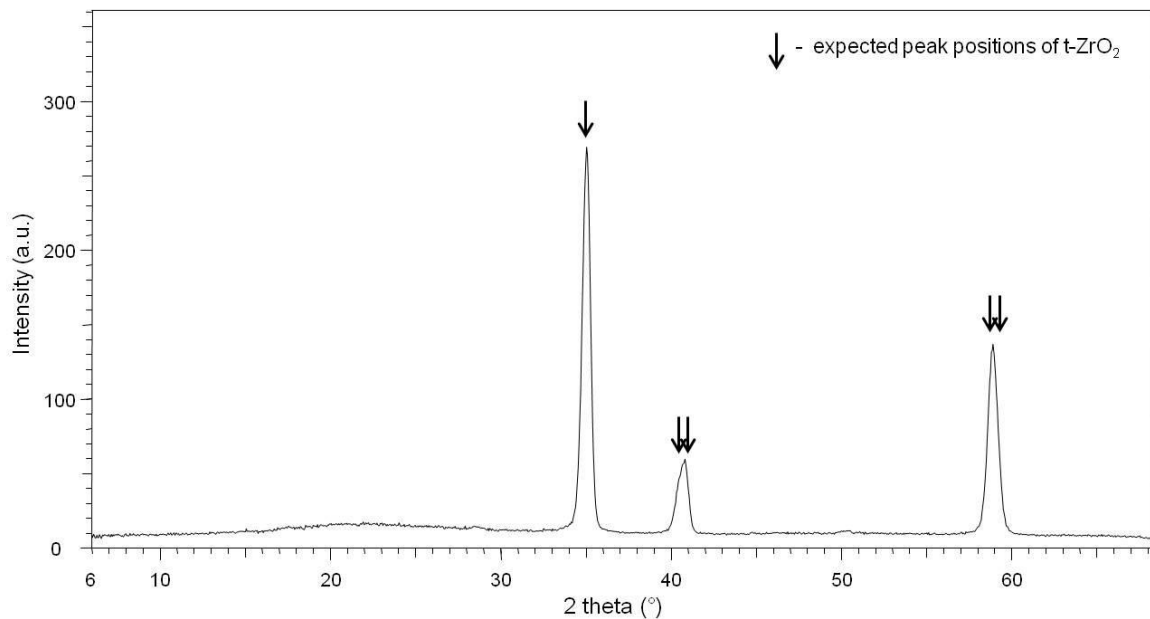


Fig. 4-13: XRD analysis of the densified layer within the YSZ top-coat of sample TS-031. Expected peak positions of t-ZrO₂ are marked. Radiation: Co-K_{α1}

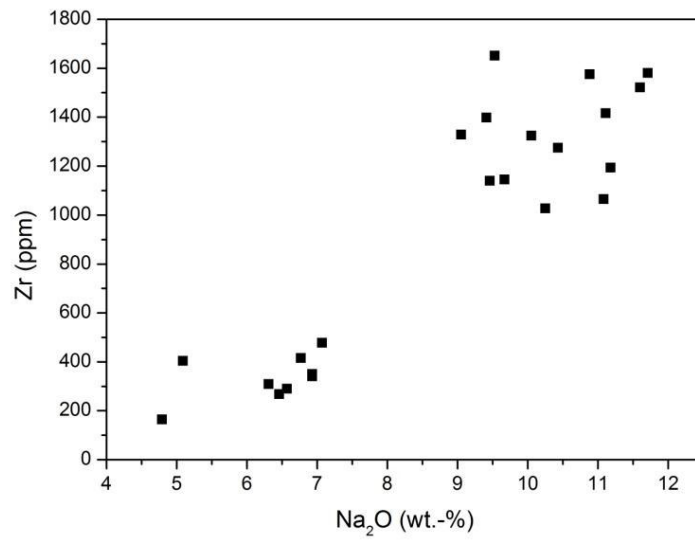


Fig. 4-14: Diagram showing the zirconium versus sodium oxid content of whole rock analysis from sanidinites from the Laacher See volcano. Modified after Abbichler et al. 2016.

4.2 Combined gas phase and salt melt experiments

Parts of this chapter are modified after Steinmetz (2015).

Since heat exchanger tube surfaces in WTE plants are exposed to aggressive gas phases and salt melts, lab-scale experiments simulating a combined gas phase and salt melt interaction were conducted. To introduce the salts, the zirconia-coated steel cylinders were impregnated with a saturated salt solution. It is assumed that the solution fills up open pores and ensures a homogeneous distribution of the dissolved salts within the coating. During heat treatment, the salts are supposed to form a low melting eutectic salt melt which interacts with the atmosphere and the coating. A summary of the experiments is shown in Fig. 4-15. The analysis was done on the basis of element mappings (Fig. 4-16 and Fig. 4-17). In order to compare the distribution of chromium, nickel and iron within the multilayer coating their relative concentrations are shown in Fig. 4-18, Fig. 4-19 and Fig. 4-20. These diagrams represent the average intensities of each single line of the element mapping (60 points per line). Due to the irregular surface morphologies of the substrate – bond-coat and bond-coat – top-coat transitions, the vertical position was adapted for each column. For the comparison of the iron content within the bond-coat it needs to be considered that two different materials were used (Diamalloy 1005 with 2.5 wt.-% Fe; Nibasit 625-P with 4 wt.-% Fe). Tab. 3-3 gives an overview of the composition and reaction conditions of the combined gas phase and salt melt experiments.

As references, three different samples were used: (a) an untreated sample (TS-000), (b) a sample treated for 3 days under pure nitrogen atmosphere at 700 °C (TS-029) and (c) a sample treated for 3 days under an atmosphere of N₂ – 2.1 vol.-% HCl – 0.9 vol.-% O₂ at 700 °C (TS-043). The untreated sample shows thin chromium- and oxygen-rich layers within the bond-coat, representing Cr₂O₃ surfaces of former splat surfaces, but no Cr₂O₃ layer at the transition between bond- and top-coat, as already presented in chapter 4.1. Nickel and iron form a sharp transition line at the substrate – bond-coat and bond-coat – top-coat interfaces. Within sample TS-029 a similar chromium distribution as for TS-000 is observable. Nickel and iron form an extended transition zone between bond-coat and steel substrate (Fig. 4-18). Sample TS-043 shows a newly formed chromium enrichment at the border bond-coat – top-coat with a width of approximately 10 µm. Additionally, an enrichment of chromium is observable in the steel substrate. Similar to sample TS-029, nickel forms a transition zone between bond-coat and steel substrate.

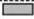

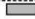
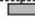


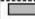
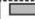


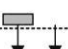


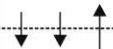

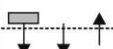

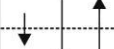
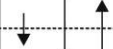
The samples treated under atmospheric conditions (denoted as “air” – TS-044, TS-045, TS-046) reveal a transition zone for chromium, nickel and iron at the border between bond-coat and steel substrate, while nickel and chromium are enriched in the steel substrate and iron in the bond-coat (see Fig. 4-15). The strongest element migration can be found for the sample, impregnated with a solution of sodium and zinc chlorides and sulfates (TS-045) with a transition zone thickness of 16 µm for chromium and nickel and 22 µm for iron. The thicknesses of the transition zones for the other two salt mixtures (potassium-zinc, potassium-sodium) is 8 – 10 µm for chromium and nickel and 14 – 15 µm for iron. Additionally, chromium and nickel form a thin (7 – 9 µm) transition zone

at the top-coat – bond-coat interface of sample TS-045 (sodium-zinc). No formation of a Cr_2O_3 layer at the top of the bond-coat is observable for any sample treated under air.

Samples treated under HCl-O_2 atmosphere (TS-040, TS-041, TS-042) show a transition zone for chromium, nickel and iron at the border between bond-coat and steel substrate as well (see Fig. 4-15), with the thickest transition zones of the respective elements for potassium and zinc chloride and sulfate salt solution impregnated samples (TS-041). The thickness of the chromium transition zone for sample TS-041 is 17 μm , while for nickel it is 30 μm and 28 μm for iron. For sample TS-040 (potassium-zinc), chromium and nickel show a transition zone thickness of 12 μm and for iron 17 μm . Within sample TS-042 (potassium-sodium) the transition zones for all three elements have a similar thickness of 10 μm . Additionally, nickel and chromium show a thin transition zone with a thickness of 4 – 6 μm at the top-coat – bond-coat interface for samples TS-041 and TS-042. Notably is the formation of a Cr_2O_3 layer at the top of the bond-coat within all three samples.

Samples treated under an atmosphere of HCl-SO_2 (TS-037, TS-038, TS-039) also show a transition zone at the bond-coat – steel substrate interface for chromium (see Fig. 4-15), nickel and iron. In contrast to the other experiments (under air and HCl-O_2 atmosphere) the thicknesses of these transition zones are similar for all three salt mixtures: chromium – 9 μm , nickel – 20 - 21 μm , iron – 16 - 20 μm . At the border top-coat – bond-coat also a newly formed Cr_2O_3 layer is observable.

All salt solution impregnated samples, as well as reference sample TS-043, show an iron enrichment within the top-coat (see Fig. 4-16 and Fig. 4-17).

atmosphere	---	N ₂	HCl + O ₂	Air			HCl + O ₂			HCl + SO ₂		
sample	TS-000	TS-029	TS-043	TS-044	TS-045	TS-046	TS-040	TS-041	TS-042	TS-037	TS-038	TS-039
salts				K, Zn	Na, Zn	K, Na	K, Zn	Na, Zn	K, Na	K, Zn	Na, Zn	K, Na
top-coat					7 9			5 5	6 4			
bond-coat												
steel substrate												
	Cr Ni Fe	Cr Ni Fe	Cr Ni Fe	Cr Ni Fe	Cr Ni Fe	Cr Ni Fe	Cr Ni Fe	Cr Ni Fe	Cr Ni Fe	Cr Ni Fe	Cr Ni Fe	Cr Ni Fe

legend:  Cr₂O₃ enrichment


 element diffusion (the vertical position represents the relative position of the diffusion zone within the coating, the thickness of the diffusion zone is given in μm)

Fig. 4-15: Overview of the experiments with a combined gas phase and salt melt interaction. The used salts were always an equimolar mixture of chlorides and sulfates of the mentioned cations (potassium, sodium, zinc).

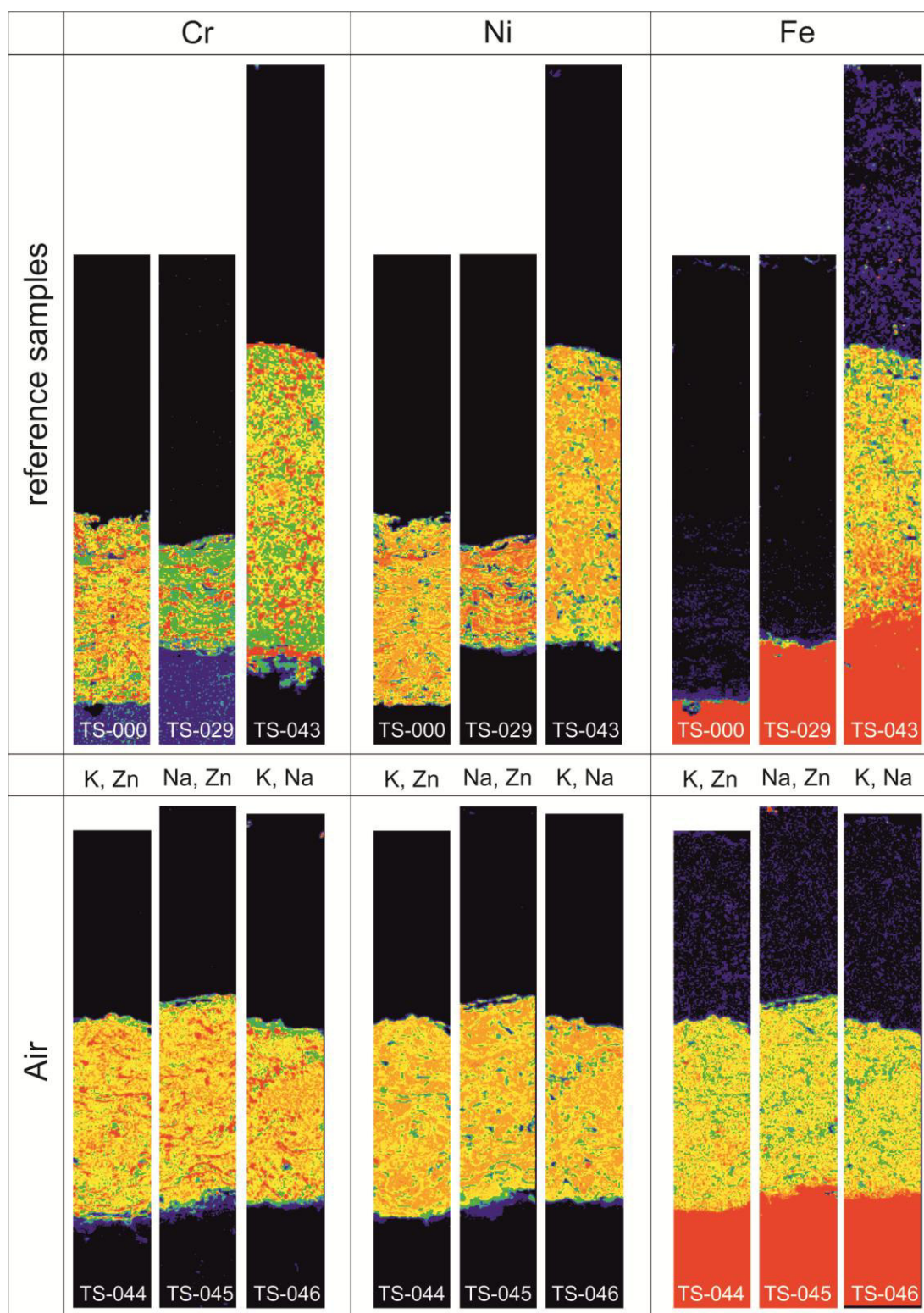


Fig. 4-16: Element mappings for chromium, nickel and iron. Reference samples were treated as follows: (a) untreated (TS-000), (b) 700 °C, pure nitrogen atmosphere, 3 days (TS-029) (c) 700 °C, $N_2 - 2.1 \text{ vol.}\% \text{ HCl} - 0.9 \text{ vol.}\% \text{ O}_2$, 3 days (TS-043). The displayed samples TS-044, TS-045, TS-046 were impregnated with saturated, equimolar solutions of K & Zn, Na & Zn and K & Na chlorides and sulfates, respectively, and treated at 700 °C for 3 days under atmospheric conditions.

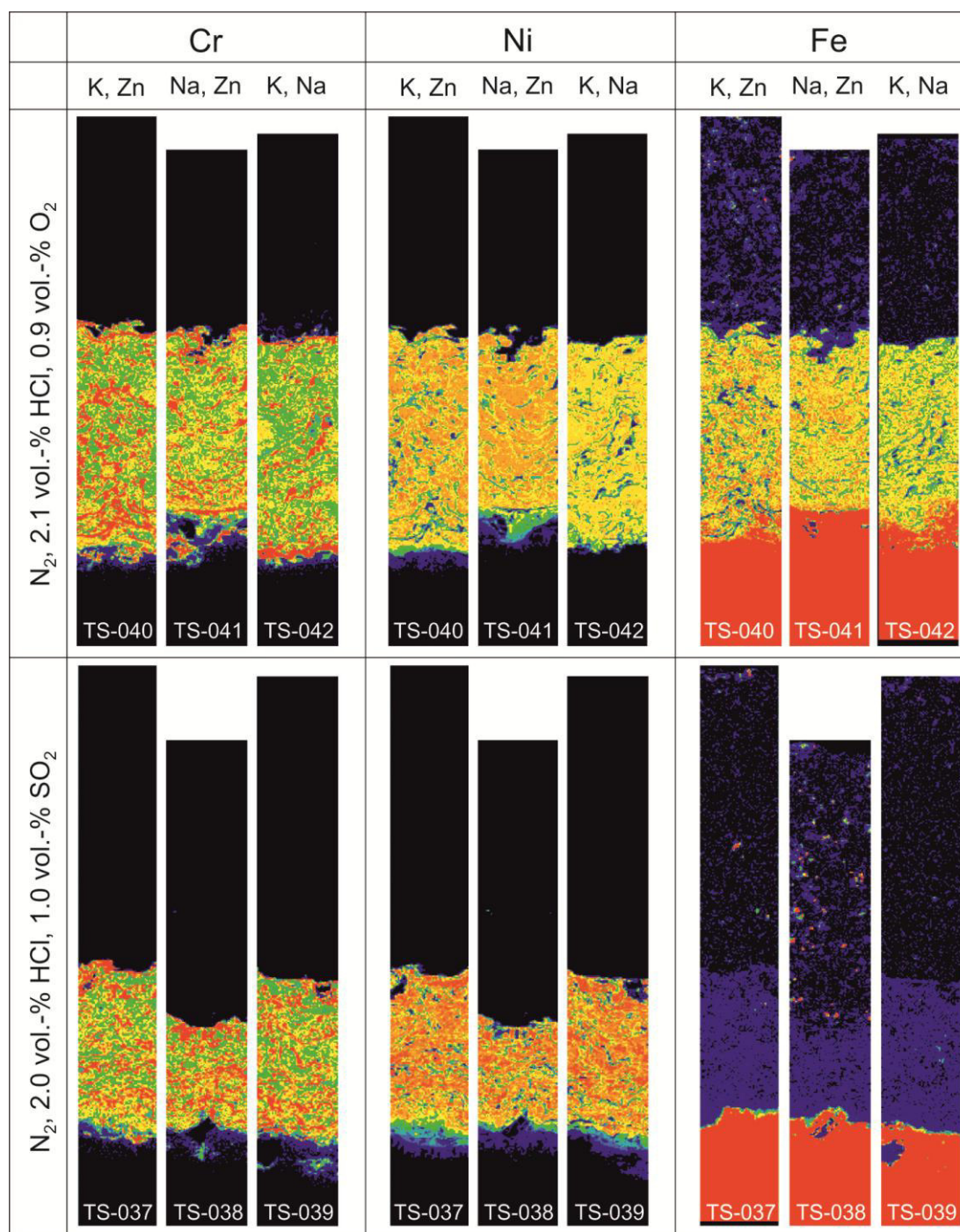


Fig. 4-17: Element mappings for chromium, nickel and iron. The displayed samples at the top TS-040, TS-041, TS-042 were impregnated with saturated, equimolar solutions of K & Zn, Na & Zn and K & Na chlorides and sulfates, respectively, and treated at 700 °C for 3 days under N_2 – 2.1 vol.-% HCl – 0.9 vol.-% O_2 . The shown samples at the bottom TS-037, TS-038, TS-039 were impregnated with saturated, equimolar solutions of K & Zn, Na & Zn and K & Na chlorides and sulfates, respectively, and treated at 700 °C for 3 days under Ar – 2.0 vol.-% HCl – 1.0 vol.-% SO_2 .

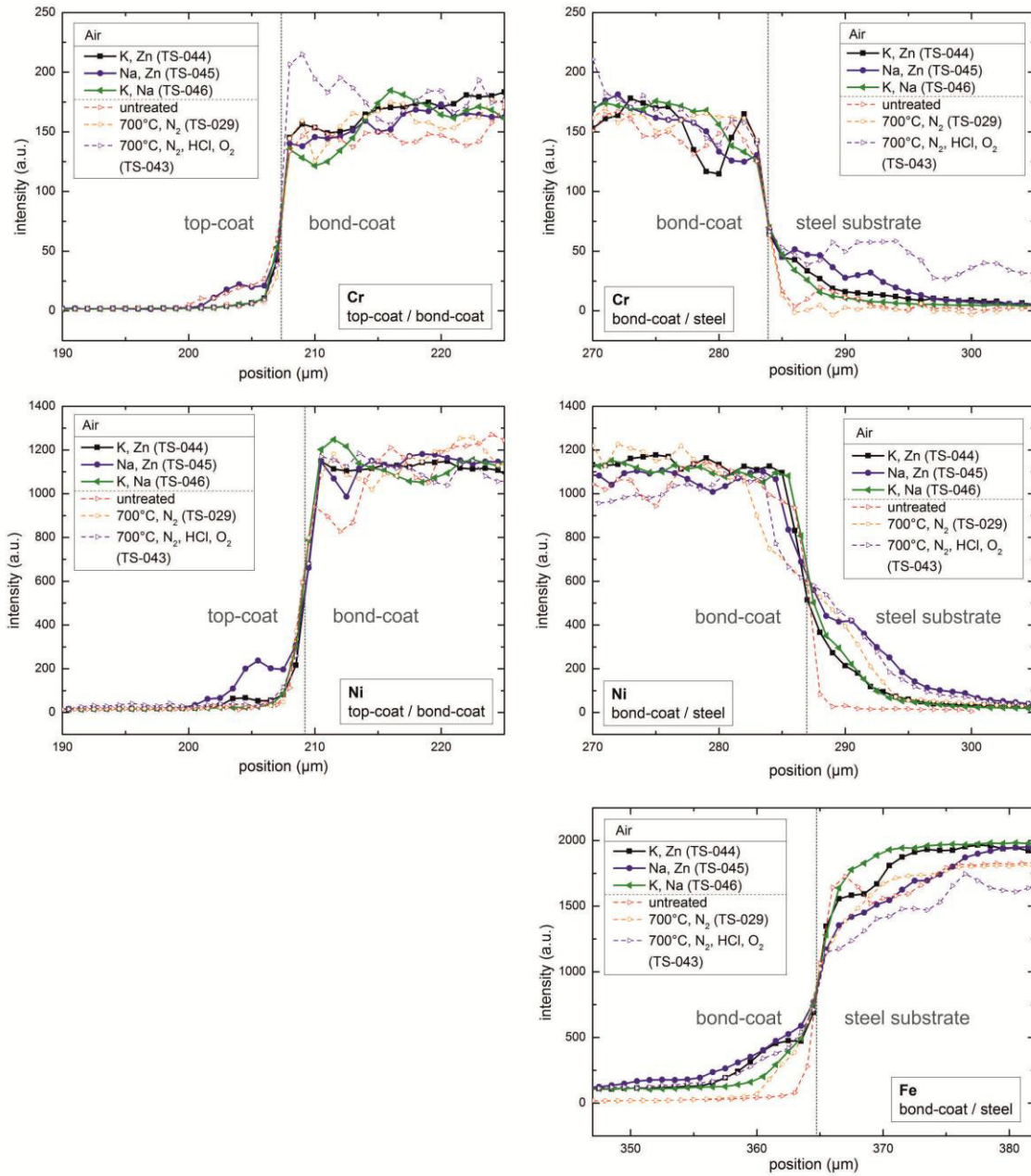


Fig. 4-18: Profiles of the transition zones between top-coat / bond-coat and bond-coat / steel for chromium and nickel and bond-coat / steel for iron. The displayed samples TS-044, TS-045, TS-046 were impregnated with saturated, equimolar solutions of K & Zn, Na & Zn and K & Na chlorides and sulfates, respectively, and treated at 700 °C for 3 days under air. Reference samples were treated as follows: untreated (TS-000) / 700 °C, pure nitrogen atmosphere, 3 days (TS-029) / 700 °C, N₂ – 2.1 vol.-% HCl – 0.9 vol.-% O₂, 3 days (TS-043).

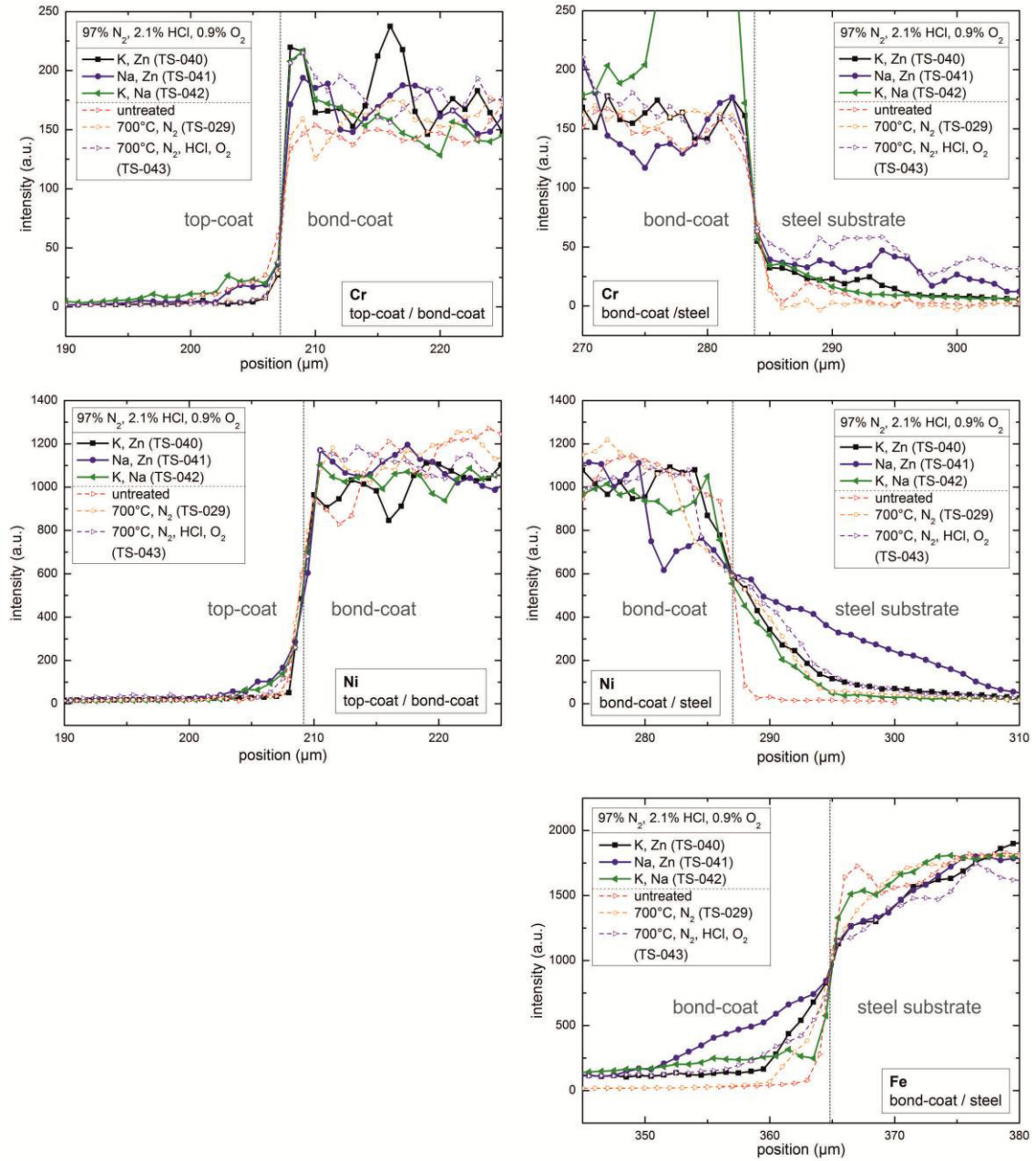


Fig. 4-19: Profiles of the transition zones between top-coat / bond-coat and bond-coat / steel for chromium and nickel and bond-coat / steel for iron. The displayed samples TS-040, TS-041, TS-042 were impregnated with saturated, equimolar solutions of K & Zn, Na & Zn and K & Na chlorides and sulfates, respectively, and treated at 700 °C for 3 days under N₂ – 2.1 vol.-% HCl – 0.9 vol.-% O₂. Reference samples were treated as follows: untreated (TS-000) / 700 °C, pure nitrogen atmosphere, 3 days (TS-029) / 700 °C, N₂ – 2.1 vol.-% HCl – 0.9 vol.-% O₂, 3 days (TS-043).

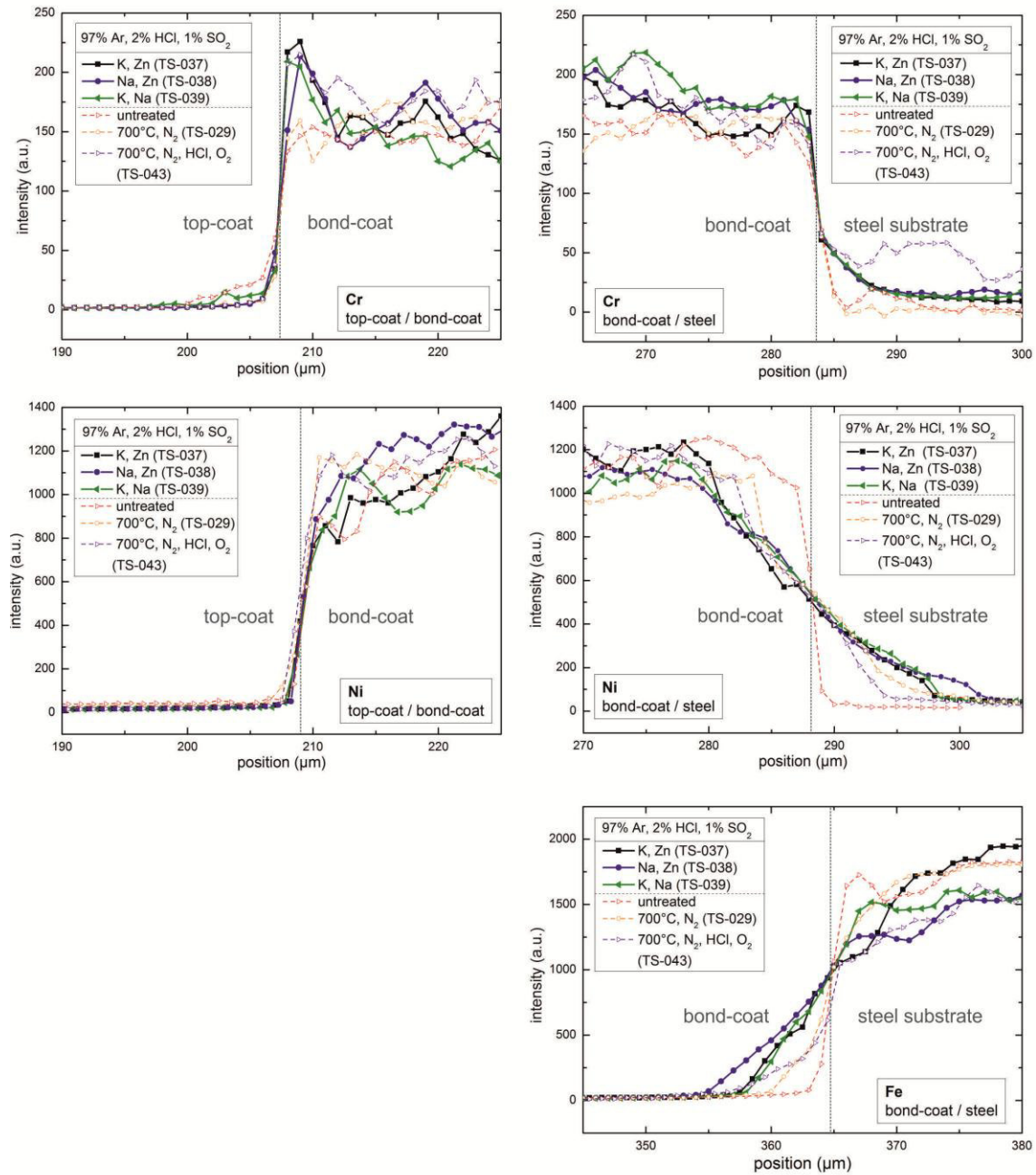


Fig. 4-20: Profiles of the transition zones between top-coat / bond-coat and bond-coat / steel for chromium and nickel and bond-coat / steel for iron. The displayed samples TS-037, TS-038, TS-039 were impregnated with saturated, equimolar solutions of K & Zn, Na & Zn and K & Na chlorides and sulfates, respectively, and treated at 700 °C for 3 days under Ar – 2.0 vol.-% HCl – 1.0 vol.-% SO₂. Reference samples were treated as follows: untreated (TS-000) / 700 °C, pure nitrogen atmosphere, 3 days (TS-029) / 700 °C, N₂ – 2.1 vol.-% HCl – 0.9 vol.-% O₂, 3 days (TS-043).

Résumé

The shape of the element distribution within the newly formed transition zones between top-coat – bond-coat and bond-coat – steel substrate is characteristic of a diffusion of the respective elements. Since this pattern is already observable for sample TS-029, treated under an inert atmosphere of pure nitrogen at 700 °C, this diffusion can be described by the Tammann diffusion (Tammann 1926). Tammann observed the onset of diffusion within crystals approximately at one third of their melting temperature. The melting point of Inconel 625 is approximately 1330 – 1400 °C (1603 – 1673 K) and of low-grade steel approximately 1500 °C (1773 K). Thus, the experimental temperature of 700 °C (973 K) represents a sufficient value to initiate a Tammann diffusion.

The formation of a Cr₂O₃ layer at the top-coat - bond-coat interface is only observable for samples treated under an HCl-O₂ and HCl-SO₂ containing atmosphere, but not under atmospheric conditions or pure nitrogen atmosphere. As shown in chapter 4.1 (Gas phase experiments), this newly grown Cr₂O₃ layer only forms at 700 °C but not at 500 °C. These observations cannot be explained by an oxidation only, following a parabolic growth rate, as described by Wagner (1956). The process of oxidation should also be observable for the experiments under air (containing ~21 % oxygen). More likely, the formation of the Cr₂O₃ layer is caused by the active oxidation process (1.3.1.1 Active oxidation), based on the combined interaction of chlorine and oxygen. Grabke and coworkers (1995) described, that chlorine diffusion through an oxide scale is preferred in contrast to oxygen diffusion, leading to an increased chlorine partial pressure at the scale – substrate interface. For the multilayer coating, used in this work, it needs to be considered that the zirconia top-coat exhibits a higher porosity (10 – 12 %) in contrast to the underlying bond-coat (< 4 % (Azarmi & Salimijazi 2015)) and zirconia represents an oxygen-ion conductor (Badwal 1992). Thus, it can be assumed that the zirconia top-coat is permeable for oxygen. Chlorine is present throughout the whole coating (top-coat and bond-coat), as already described in chapter 4.1 (Gas phase experiments). With respect to oxygen, the bond-coat is supposed to represent a barrier, since no additional formation of oxides can be found within the bond-coat or at the surface of the steel substrate within the lab-scale experiments. The low oxygen partial pressure in the presence of chlorine promotes the formation of highly volatile CrCl_x species within the bond-coat. The presence of sulfur at the border of the top-coat - bond-coat (see chapter 4.1) suggests the reduction of SO_x. In consequence a release of additional available oxygen near the bond-coat surface is expected which enhances the transformation of CrCl_x species to Cr₂O₃. The absence of a Cr₂O₃ layer for the 500 °C-treated sample can have two reasons. (a) The estimated partial pressures for chlorine and oxygen within the experiment chamber at 500 and 700 °C lay in the stability field of Cr₂O₃ (500 °C: pCl₂ = 6.59·10⁻³ bar, pO₂ = 1.93·10⁻³ bar ; 700 °C: pCl₂ = 3.75·10⁻³ bar, pO₂ = 3.06·10⁻³ bar) (Fig. 4-21). For the experiment at 700 °C, the observable combined occurrence of chromium and chromium oxide together with the assumed presence of chromium chloride (CrCl₂) determines the partial pressures for oxygen and chlorine to be log pO₂ = -31.6 bar and log pCl₂ = -14.8 bar at the border between bond- and top-coat. At 500 °C, the combined presence of chromium, chromium chloride (CrCl₂) and chromium

oxide is defined at $\log pO_2 = -42.1$ bar and $\log pCl_2 = -20.2$ bar. Since no chromium oxide layer is observable at 500 °C, such low pO_2 and pCl_2 values were not reached, which precludes the formation of Cr_2O_3 through the active oxidation process. (b) The oxygen partial pressure is low enough and / or the chlorine partial pressure is high enough, so that $CrCl_x$ phases can be generated. Due to a retarded kinetic the mobility of these phases is inhibited, so that the active oxidation process cannot take place. The iron enrichments within the top-coat can also be seen as a result of the active oxidation process, through the formation of highly volatile iron chlorides at the bond-coat – substrate interface. Since the reaction from iron chlorides to their corresponding oxides requires higher oxygen partial pressures as for the chromium reaction (see Fig. 1-5), chromium oxides will form first (at the top-coat – bond-coat interface), followed by iron oxides (within the top-coat). The preferential diffusion of chromium, nickel and iron between bond-coat and steel substrate can be seen as a result of the concentration gradient, since steel consists of >98 wt.-% iron and Inconel 625 of ~22 wt.-% chromium and ~70 wt.-% nickel.

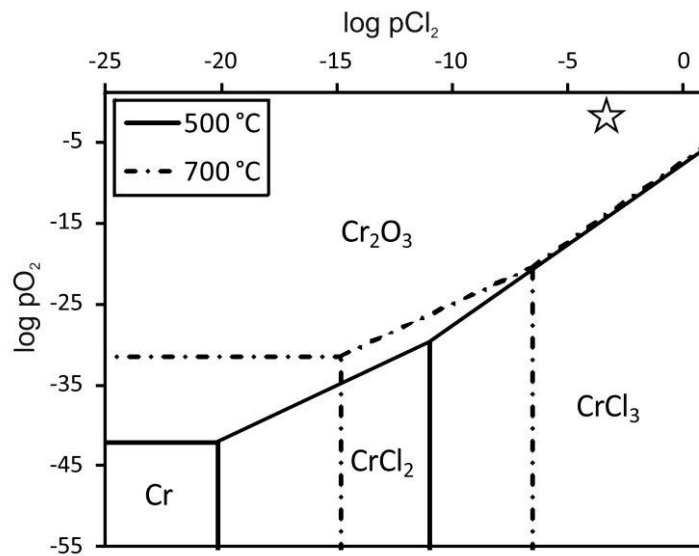


Fig. 4-21: Phase stability diagrams for chromium with respect to partial pressures of chlorine (pCl_2) and oxygen (pO_2) at temperatures of 500 °C and 700 °C. The star represents the estimated atmosphere within the experiment chamber for both temperatures. All values of pO_2 and pCl_2 are given in bar. Calculated with HSC Chemistry.

4.3 Proposed densification process in gas phase experiments

The experiments showed a densification without additional zirconium within the gas flow under specific experimental conditions: An atmosphere of $\text{N}_2\text{-HCl-O}_2$ (97 / 2.1 / 0.9 vol.-%) containing an equimolar salt mixture of $\text{KCl-K}_2\text{SO}_4\text{-ZnCl}_2\text{-ZnSO}_4$ at 700 °C (TS-031). At higher HCl content (TS-032) or lower temperatures (TS-051), no densification can be observed. Furthermore, it could be demonstrated, that the addition of zirconium in the gas flow only leads to a densification under an oxygen-bearing atmosphere (TS-055). An enhanced zirconium-free densification was achieved by using sodium salts in combination with potassium and zinc salts (TS-059).

Based on the Deacon equation (Equ. 1.1) the initial gas mixture of HCl and O_2 reacts to H_2O and Cl_2 , leading to a combined presence of all four phases at 700 °C. The molten chloride and sulfate salts mainly release Cl_2 and $\text{SO}_3 / \text{SO}_2$ (depending on the unknown oxygen partial pressure above the salt melt). In summary, the assumed reactive gas atmosphere consists of HCl, Cl_2 , O_2 , $\text{SO}_3 / \text{SO}_2$, which penetrates the coating (Fig. 4-22). The occurrence of chromium sulfide enrichments at the border top- / bond-coat of sample TS-032 suggest a reduction of the $\text{SO}_3 / \text{SO}_2$, releasing oxygen. This observation is in correspondence with observations from prior studies (Fehr et al. 2012, Ye 2016). The results from the gas phase experiments (chapter 4.1) and the combined gas phase and salt melt experiments (chapter 4.2) showed the formation of a Cr_2O_3 layer at the top-coat – bond-coat interface as a result of the active oxidation process, consuming oxygen and releasing chlorine.

Two different theories regarding the densification mechanism are currently in discussion: One option follows the theory of a solvothermal process as proposed in prior studies (Fehr et al. 2012, Masset et al. 2013, Ye 2016), suggesting a mobilization of the zirconium through a vapor phase by the formation of zirconium chloride (ZrCl_x) under a $\text{N}_2\text{-HCl}$ atmosphere. The authors describe a recrystallization of ZrO_2 as a consequence of an increased oxygen partial pressure in open pores, which is expected to cause the observed densification. As shown, for sample TS-027 this assumption needs to be negated. No densification was observable under a $\text{N}_2 - \text{HCl}$ atmosphere, but under $\text{N}_2 - \text{HCl} - \text{O}_2$ (TS-055). But, the fact that no additional zirconium is necessary for the densification implies a partial solution of the zirconia within the top-coat to provide the zirconium for the recrystallization process. Another option is a densification mechanism by grain growth via sintering in combination with a partial phase transformation from tetragonal to monoclinic zirconia (going along with a volume increase of ~4 %): In general, a significant grain growth via sintering of YSZ ceramics as well as a phase transformation from tetragonal to monoclinic, initiated by a temperature driven diffusion of yttrium, occurs at temperatures above 1100 °C (Siebert et al. 1999, Wang et al. 2007, Krogstad et al. 2011). Besides the significantly lower temperatures of the experiments described herein, both processes would affect the whole top-coat instead of creating a partially densified ceramic, as visible for sample TS-005 and TS-031 (see Fig. 4-5 and Fig. 4-7). Notably is the observation of Pasquevich and coworkers (Pasquevich et al. 1989), who found an accelerated grain growth of YSZ under a chlorine-bearing

atmosphere at even lower temperatures of 940 °C, additionally accompanied by a partial phase transformation from tetragonal to monoclinic zirconia. Thus, it seems a possible explanation, that a locally chlorine enriched atmosphere at the bottom of the top-coat promote the partial densification at 700 °C via grain growth, based on a combination of sintering and phase transformation. Since grain growth via sintering positively correlates with the temperature, our assumption supports the observations from prior studies (Fehr et al. 2012, Masset et al. 2013, Ye 2016), who found a higher densification rate at higher temperatures.

The vapor phase transport via zirconium chloride species and the chlorine induced sintering accompanied by a phase transformation, are based on the interaction of the YSZ top-coat with chlorine, which was present during the whole experiment. Therefore, the densification of the zirconia can be interpreted as a combined mechanism of both. The residual chlorine from the reactions of $\text{ZrCl}_x \rightarrow \text{ZrO}_2$ and $\text{CrCl}_x \rightarrow \text{Cr}_2\text{O}_3$ leads to a chlorine enrichment next to the top-coat – bond-coat interface, responsible for the sintering and phase transformation process (Fig. 4-22). Excess chlorine can leave the top-coat through open pores or again penetrate the bond-coat to form metal chlorides. A detection of m- ZrO_2 was not possible, neither by EPMA (Y-lean regions) nor by XRD or Raman spectroscopic analyses. This can be explained by the expected small grain size and small amount of the m- ZrO_2 phase at the grain boundary between the different YSZ splats of the top-coat. The analyzed volume of EPMA analyses is in the range of several micrometers, comparable to the spatial resolution of Raman spectroscopic measurements (Presser et al. 2009), and the detection limit for XRD analyses is approximately 2 %.

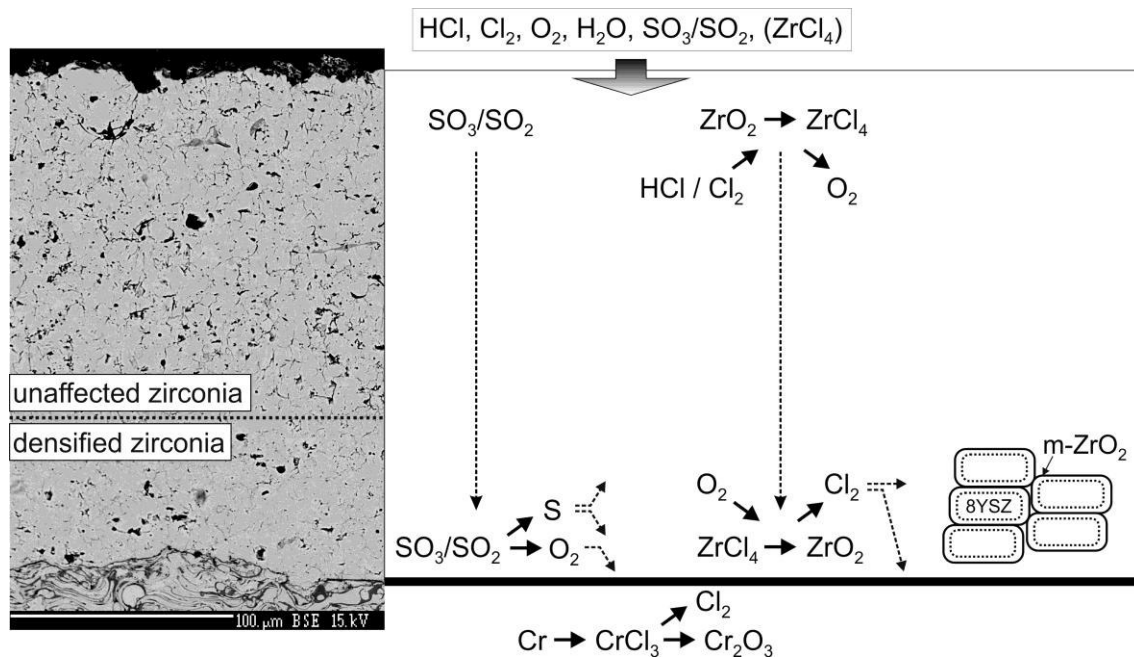


Fig. 4-22: Schematic illustration of the proposed densification process for the ceramic top-coat.

4.4 Salt melt experiments

Parts of this chapter are modified after Müller & Heuss-Aßbichler, 2016.

4.4.1 Dissolution and recrystallization phenomena

4.4.1.1 Investigation of the beads

To determine the influence of the salt amount, the zirconia beads were treated in four different amounts of salt (20, 30, 40 and 60 mmol) at 600 °C under an atmosphere of N₂ - 2.55 % O₂ - 0.45 % HCl (Fig. 4-23) (Tab. 4-4). The 60 mmol (SE10, SE11) series shows an exponentially increasing weight loss, hence dissolution of the zirconia, within four days. For the 40 mmol series (SE08, SE09) an enhanced weight loss is observable in comparison to the 60 mmol series. The 30 mmol sample series (SE05, SE06, SE07) shows an intense weight loss during the first two days, much stronger than for the 40 and 60 mmol sample series. After two days the weight loss diminishes, expressed by the weight loss difference between the experiments: after one day (SE06-SE05) -0.79 %, and the next day (SE07-SE06) -0.47 %. For the 20 mmol series (SE01, SE02, SE03, SE04), the strong weight loss only lasts for the first day. The maximum dissolution is achieved after two days. Afterwards the beads show a weight gain.

In summary, the experiments show that all samples have lost weight as a consequence of the combined chemical and thermal treatments. While decreasing the amount of salt the dissolution of zirconia becomes accelerated. For samples treated for two days at 600 °C this can be expressed as the ratio of weight loss versus salt amount ($\Delta m_{\text{YSZ}}/m_{\text{salt}}$): 0.005, 0.015, 0.039, 0.105 (60, 40, 30, 20 mmol, respectively). For higher salt amounts the dissolution starts slower but in the long-term it leads to higher values of mass loss than for smaller amounts of salt.

Experiments at 700 °C with a salt amount of 40 mmol (SE12, SE13, SE14) exhibit a similar trend as for 600 °C and 20 mmol of salts (Fig. 4-23). The only difference is the maximum amount of dissolved zirconia: after two days it was maximal 0.88 % at 700 °C in comparison to 2.10 % at 600 °C.

Besides zirconia, it was observable that with each experiment the Al₂O₃ crucible became lighter (\varnothing 0.03 %). This indicates a minor dissolution of alumina through interaction with the salt melt as well.

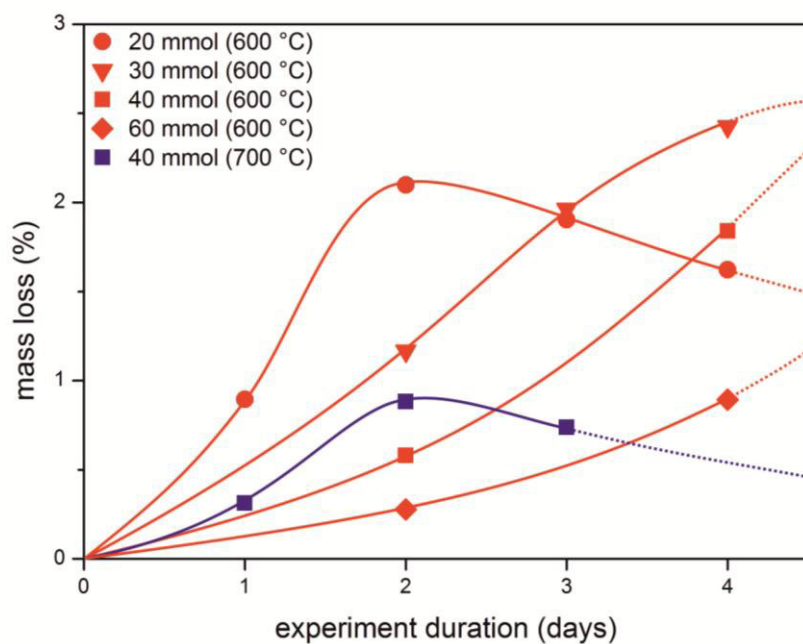


Fig. 4-23: Graph showing the weight loss of the zirconia beads, treated at 600 °C (red) and 700 °C (blue) in different amounts of KCl-K₂SO₄-ZnCl₂-ZnSO₄. The relative error for each experiment is about 0.06 %, approximately represented by the size of the markers.

Tab. 4-4: Experimental conditions for the investigation of YSZ beads with a salt melt together with the percental mass loss of the YSZ beads.

sample	used salts	m _{salts} (mmol)	T (°C)	duration (days)	Δm YSZ (%)
SE01	KCl, K ₂ SO ₄ , ZnCl ₂ , ZnSO ₄	20	600	1	0.89
SE02		20		2	2.10
SE03		20		3	1.90
SE04		20		4	1.62
SE05		30		2	1.17
SE06		30		3	1.96
SE07		30		4	2.43
SE08		40		2	0.58
SE09		40		4	1.84
SE10		60		2	0.28
SE11		60		4	0.89
SE12	KCl, K ₂ SO ₄ , ZnCl ₂ , ZnSO ₄	40	700	1	0.31
SE13		40		2	0.88
SE14		40		3	0.74

BSE-EPMA

The surface of the beads was examined in cross sections by the use of BSE images. Untreated samples show a uniform, flat surface. The experiment performed for two days at 600 °C with 20 mmol salt amount (SE02) exposes two different surface features: (a) on the upper side only dissolution effects are present. As shown in Fig. 4-24, the attacked surface exhibits a rough and edged structure. (b) On the bottom side a newly formed layer is observable on top of a previously dissolved surface (Fig. 4-24). Notable, the previously attacked surface exhibits a smoother and more rounded morphology. The new layer with a maximum thickness of approximately 15 µm covers approximately 50 % of the two days treated spheres. Beads treated for only one day show an all over attacked surface, while after three days of treatment (or longer) the sphere is totally enclosed by the newly formed layer.

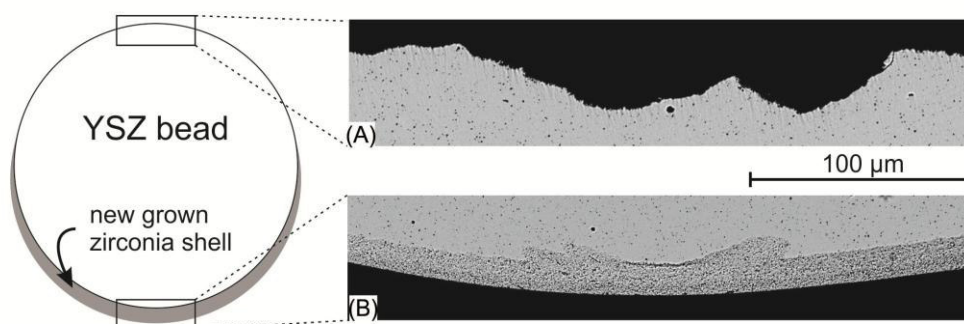


Fig. 4-24: BSE images showing (A) the attacked surface at the top and (B) the recrystallized surface on top of a previously attacked surface of a zirconia bead from sample SE02.

EPMA

Element mappings on an untreated bead show a homogeneous composition of the zirconia, containing minor amounts of aluminum (93.03 wt.-% ZrO_2 , 2.05 wt.-% HfO_2 , 5.24 wt.-% Y_2O_3 , 0.28 wt.-% Al_2O_3) (Tab. 4-5). Additionally some inclusions of Al_2O_3 grains ($< 2 \mu\text{m}$) were detected. The Al_2O_3 was deliberately added during the production process to improve physical and mechanical properties of the zirconia as well as to enhance its hydrothermal resistance (pers. Comm. Egbert Kleinert, SEPR Keramik GmbH & Co. KG, Saint-Gobain Zirpro). Element mappings on sample SE02 (treatment for two days at 600 °C with 20 mmol salt amount) show a homogeneous chemical distribution within the bead and within the new layer as well (Fig. 4-25). The composition of the bead is similar to an untreated sample, containing 5.23 wt.-% Y_2O_3 (Tab. 4-5). However, the newly formed layer exhibits only 3.74 wt.-% Y_2O_3 , as indicated in the BSE image by the dark grey appearance in contrast to bright grey color of the bead substrate (see Fig. 4-24).

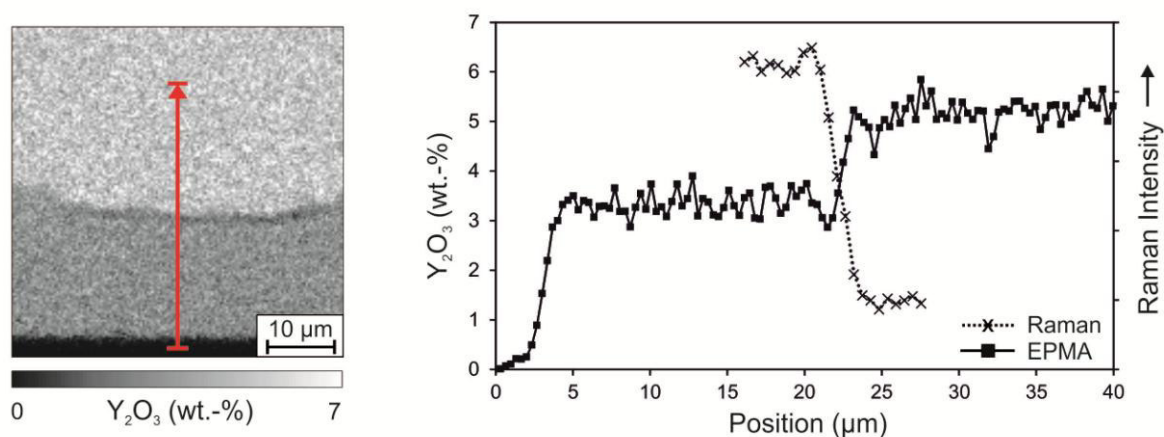


Fig. 4-25: Detailed view of the newly formed layer in the central part of Fig. 4-24 (B) (sample SE02). An element mapping of yttrium (left) and a line scan for yttrium (right) show a homogeneous distribution of yttrium within the bead substrate (5.23 wt. % Y_2O_3) and the new grown zirconia shell (3.74 wt.-% Y_2O_3). The Raman line scan (right) shows the Raman intensity under the graph of the Raman pattern between wavenumbers of 165 and 210 cm^{-1} , representing the amount of monoclinic zirconia. The monoclinic new grown shell is separated by a sharp transition line from the tetragonal bead.

Tab. 4-5: Chemical compositions of untreated zirconia beads and sample SE02, treated for two days in 20 mmol salt amount. For the treated sample, analysis of the new grown zirconia layer and the underlying bead are shown.

	SE02		
	untreated	bead	layer
ZrO_2	93.03	92.77	94.00
HfO_2	2.05	2.06	2.11
Y_2O_3	5.24	5.23	3.74
Al_2O_3	0.28	0.25	0.16
Total	100.60	100.31	100.01

Raman spectroscopy

Raman spectroscopic measurements of an untreated bead surface show a pure tetragonal pattern (Fig. 4-26). Analyses of an attacked and uncovered bead surface show a pattern of t- ZrO_2 with three additional peaks at 182, 193 and 381 cm^{-1} , indicating the formation of m- ZrO_2 . For the new layer, a pure monoclinic Raman pattern is observable. A cross-sectional line scan, perpendicular to the interface of the new layer and the previously attacked surface was done within the same area as the EPMA mapping (see line in Fig. 4-25). The outer layer consists of monoclinic zirconia, separated by a sharp transition line from the tetragonal zone of the bead. These observations correspond with EPMA analysis giving only 3.74 wt.-% Y_2O_3 for the newly formed layer. This concentration is insufficient to stabilize the tetragonal zirconia modification at room temperature (Brandon & Taylor 1991). The small proportion of monoclinic zirconia (Fig. 4-26) observable on the dissolved surface (see Fig. 4-24(A)) is possibly the contribution of a thin monoclinic rim. It has to be considered that the sampling depth of the laser beam is in the range of

several micrometers (Presser et al. 2009). These observations point to a phase transformation initiated by the leaching of the stabilizing agent yttrium within a thin surface volume of the bead. This is similar to the leaching and transformation process described by studies with vanadium containing melts (Rao et al. 2012, Shankar et al. 2008, Lee & Baik 2009, Ahmadi-Pidani et al. 2012, Habibi & Guo 2015, Reddy & Gandhi 2013) or a silica rich slag (Hemberger et al. 2012).

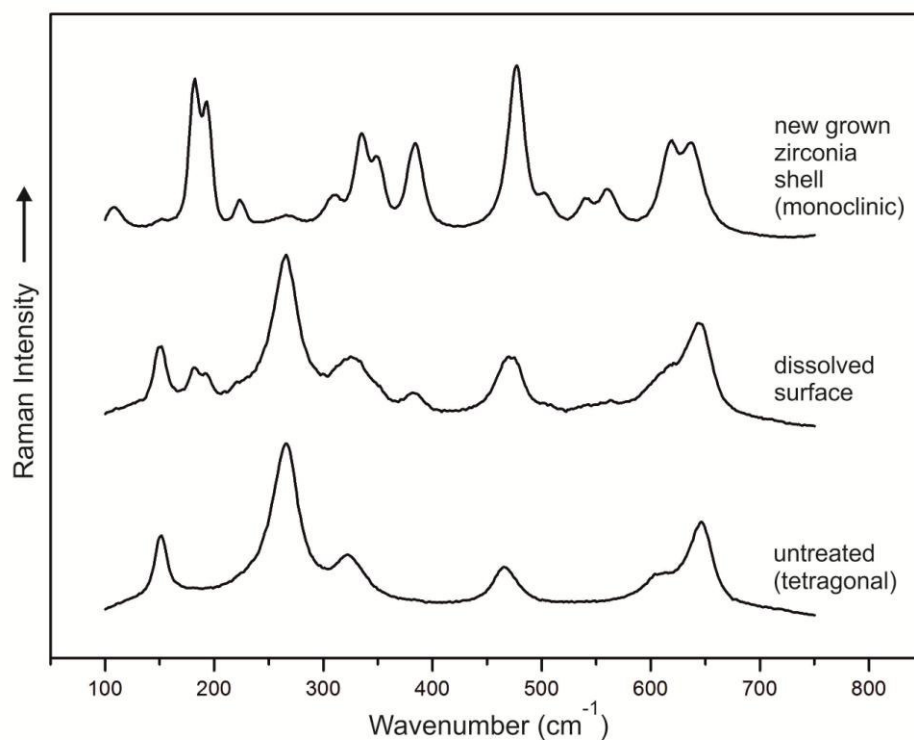


Fig. 4-26: Comparison of Raman spectroscopic surface analyses of untreated and dissolved (SE01) surfaces as well as the new grown zirconia shell (SE02).

4.4.1.2 Investigation of the residual powder

XRD

The initially obtained residual powder and the calcinated powders, heated for 24 hours at 100 to 1000 °C in steps of 100 °C, were measured by XRD analyses (Fig. 4-27). The untreated powder and those heated to 300 °C show no peaks and can, therefore, be described as an amorphous material. After calcination at 400 °C first peaks occur. The peaks at 28.3° and 31.5° 2 theta can be assigned to monoclinic zirconia, the other one at 30.3° 2 theta to tetragonal or cubic (c-ZrO₂) zirconia. At 500 °C these peaks become more pronounced. A differentiation of these phases can be done by a detailed study of the 2 theta region between 48-52°: m-ZrO₂ (ICSD #62993) exhibits five peaks at 48.90°, 49.24°, 50.10°, 50.54° and 51.17° 2 theta, t-ZrO₂ (ICSD #93028) two peaks at 50.41° and 50.95° 2 theta and c-ZrO₂ (ICSD #89429) one peak at 50.21° 2 theta. However, the quality of the pattern is poor due to the bad crystallinity and the small amount of powder, therefore, only a manual peak fitting was possible, as shown in the inset of Fig. 4-27. The four peaks observable at 49.45°, 50.29°, 50.73° and 51.17° 2 theta, verify the presence of

m-ZrO₂. A reliable differentiation between the cubic or tetragonal phase is not possible, since their peaks may be overlaid by peaks of the monoclinic phase. At high temperatures between 600 °C and 1000 °C, however, the peak at 30.3° 2 theta gradually disappears while the monoclinic polymorph becomes the only detectable phase. This calcination development from amorphous to monoclinic zirconia, with intermediate formation of cubic and / or tetragonal polymorphs, corresponds well with observations of other authors (Naguib & Kelly 1970, Zyuzin et al. 2006, Leib et al. 2015, Drazin & Castro 2015).

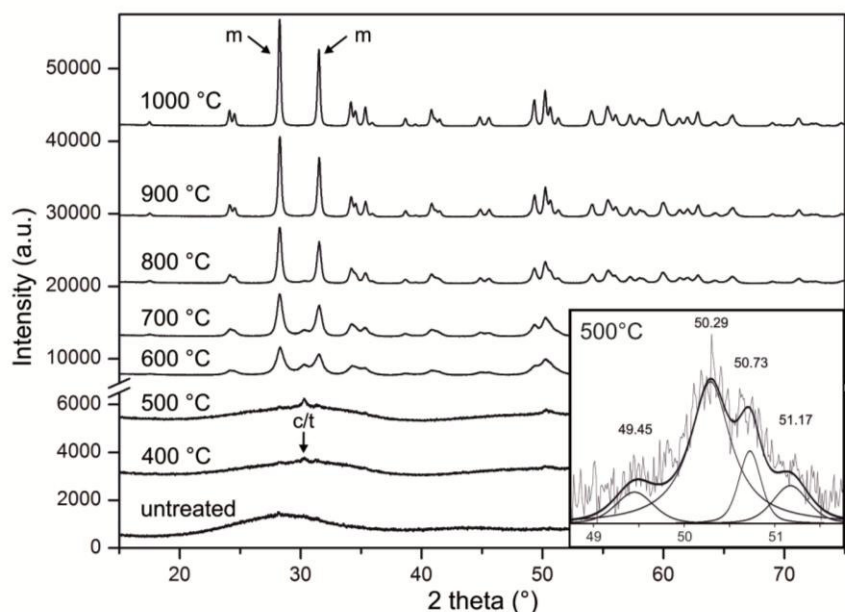


Fig. 4-27: XRD analyses of the residual powder, calcinated in stages of 100 °C. The untreated powder shows no peaks, thus, can be seen as amorphous zirconia. At 400 °C, first cubic (c) and/or tetragonal (t) zirconia can be observed, gradually displaced by monoclinic (m) zirconia at increasing temperatures. Inset shows a detailed study of the 500 °C sample in the range between 48.75 – 51.75° 2 theta. Four different peaks at 49.45, 50.29, 50.73 and 51.17° 2 theta can be observed, indicative for m-ZrO₂. Radiation: Cu-K_{α1}.

FT-IR

The initial powder was also analyzed by FT-IR spectroscopy. Prominent peaks are observable at 441, 500, 620, 1000, 1070, 1132, 1216 and 1630 cm⁻¹ and a broad absorption band between 2600 – 3800 cm⁻¹ (Fig. 4-28). The absorption bands between 400 – 1300 cm⁻¹ account for various Zr-O vibrations (Merle-Méjan et al. 1998, Sarkar et al. 2006). The absorption bands at 1630 cm⁻¹ and 2600 – 3800 cm⁻¹ can be assigned to Zr-OH bending and stretching modes, respectively (Sarkar et al. 2006) or to adsorbed water on the surface of the zirconia (Merle-Méjan et al. 1998). Thus, the powder can tentatively be seen as ZrO(OH)₂·nH₂O.

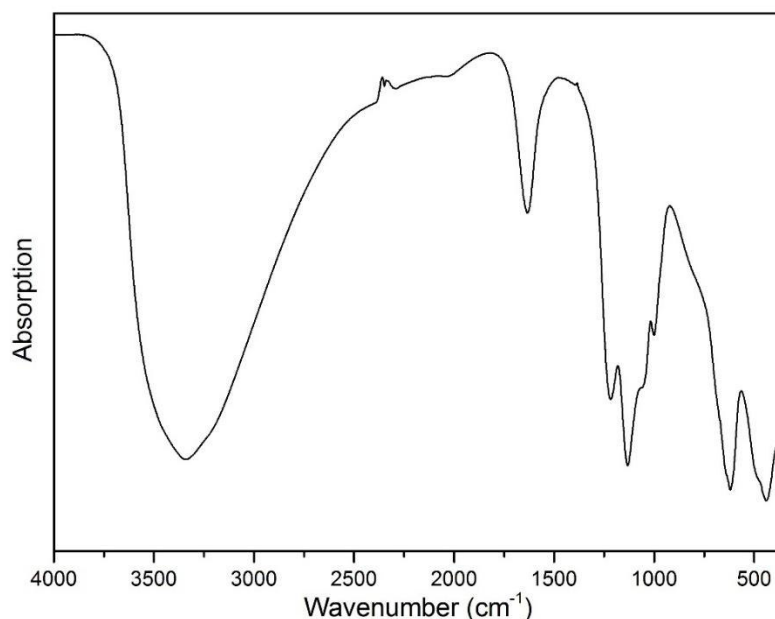


Fig. 4-28: FT-IR spectrum of the uncalcinated residual powder.

4.4.1.3 Investigation of the residual salt melt

ICP-OES

The initial salt mixture and the residual salt melts after one to three days of experiment were analyzed by ICP-OES (Fig. 4-29), in order to determine their chemical evolution. During the first day the concentration of all four elements decreased significantly: -62% S; -60% Zn; -52% Cl; -44% K. For sulfur, zinc and potassium this decreasing trend weakens between one and two days (-30% S; -22% Zn; -11% K), while the concentration of chlorine becomes slightly enriched (+10%). Between two and three days the concentration of sulfur and zinc decreased further (-32% S; -17% Zn), whereas the concentration of chlorine increased (+11%), while the concentration of potassium seems to be unchanged (-0.5%). These results attest a significant change in the chemical composition of the melt within the first three days of experiment, leading to a KCl dominated composition (Fig. 4-30).

Additionally, the yttrium and zirconium concentration in the residual salt melt of an YSZ beads-containing experiment with 60 mmol salt amount for four days at 600 °C (SE11) was analyzed. The Y/Zr ratio was 6/25 (0.24), representing a significant enrichment of yttrium within the residual salt melt. In comparison the YSZ beads show a Y/Zr ratio of 2/31 (0.06).

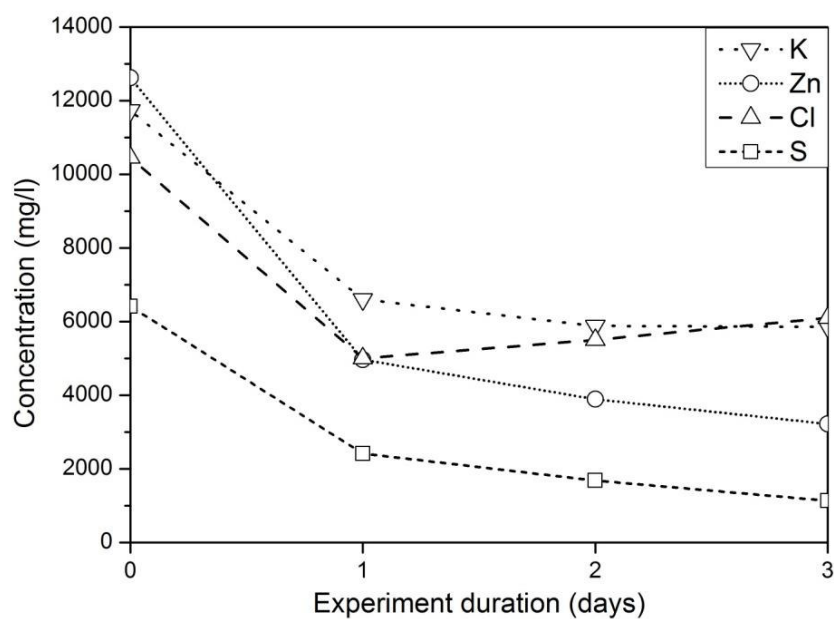


Fig. 4-29: ICP-OES analyses of residual salt melts before any treatment and after one, two and three days of treatment at 600 °C under chlorine containing atmosphere. The initial amount of salt was 20 mmol. The error of each analysis is represented with the size of the markers.

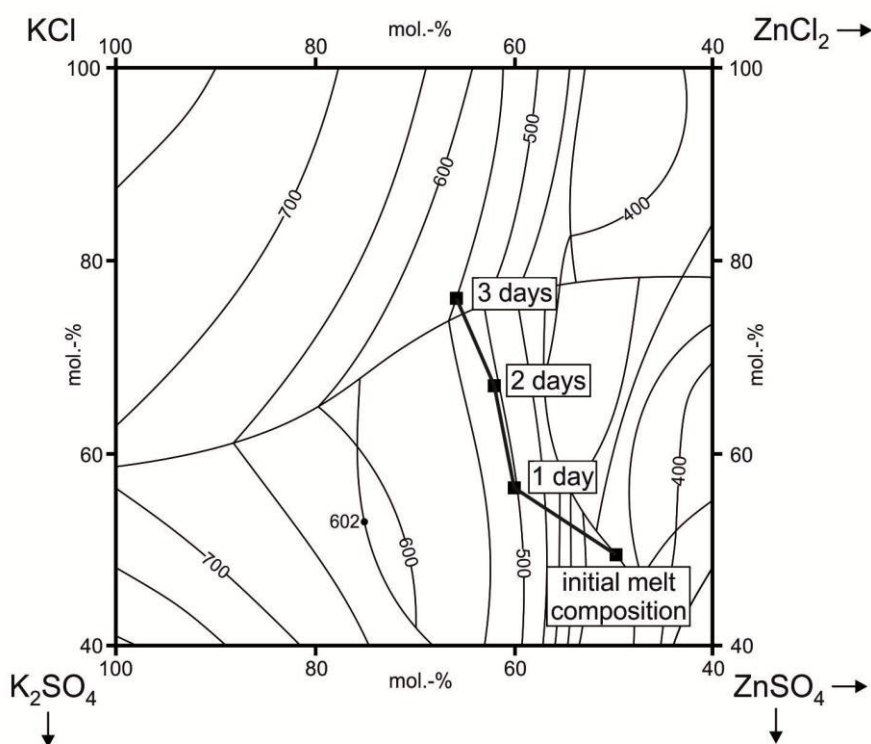


Fig. 4-30: Section of the phase diagram of KCl-K₂SO₄-ZnCl₂-ZnSO₄ after Lushnaya and coworkers (1956). The evolution of the salt melt of 20 mmol salt amount within three days of experiment is shown.

XRD

An XRD analysis of the residual salt melt after the third day of experiment gives a composition of mainly ZnK_2Cl_4 and K_2SO_4 with some minor amounts of KCl (Fig. 4-31). The only zinc containing phase is ZnK_2Cl_4 with a ZnCl_2/KCl ratio of 1/2. This result indicates a significant loss of zinc during the experiment compared with the initial salt mixture containing equimolar amounts of KCl , K_2SO_4 , ZnCl_2 and ZnSO_4 (1/1/1/1). Most likely zinc vaporizes as ZnCl_2 owing to its higher vapor pressure of $1.09 \cdot 10^{-1}$ bar at 600 °C. In contrast, the retention of potassium is presumably the effect of the lower vapor pressures of KCl and K_2SO_4 ($4.53 \cdot 10^{-6}$ bar and $4.61 \cdot 10^{-5}$ bar, respectively). A continuous vaporization of gaseous SO_3 can be assumed as the dominating process for the reduction of sulfur, due to the high vapor pressure of SO_3 of $9.30 \cdot 10^2$ bar at 600 °C.

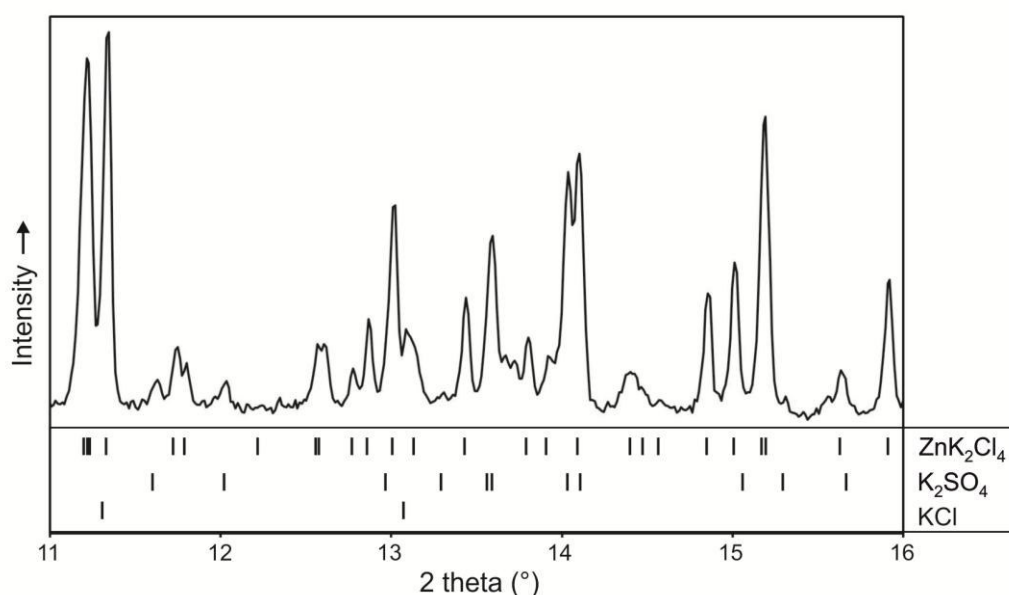


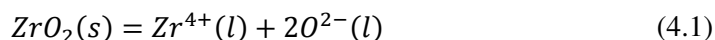
Fig. 4-31: XRD analysis of the residual melt after three days under chlorine containing atmosphere at 600 °C. For an unambiguous identification of the three phases ZnK_2Cl_4 , K_2SO_4 and KCl the 2 theta range between 11-16° is shown. Radiation: $\text{Mo-K}_{\alpha 1}$.

4.5 Proposed dissolution and recrystallization process in salt melt experiments

To understand the observed dissolution of zirconia it is necessary to consider the composition of the atmosphere. The initial gas mixture consists of HCl and O_2 , with N_2 as the carrier gas. According to the Deacon equation (Equ. 1.1) the atmosphere at 600 °C consists of HCl , Cl_2 , H_2O and O_2 in the ratio 2/1/1/0.5.

Molten salts can be regarded as a mixture of free ions and/or ion pairs (Bloom 1967). Thus, a dissociation of the salts (KCl , K_2SO_4 , ZnCl_2 , ZnSO_4) releases K^+ , Zn^{2+} , Cl^- and SO_4^{2-} ions. The ICP-OES analyses of the residual salt melt indicate a preferential decrease of the positively-charged Zn^{2+} during the first day, which means a shift of the electromotive force (e.m.f.) to more negative values. Consequently, ZrO_2 will become

unstable and will be dissolved in the molten salts (as shown in Fig. 4-32) by forming Zr^{4+} ions according to Equation (4.1).



Since yttrium has a more basic character in comparison to zirconium it will be attacked (leached) first, as proved by the changed Y/Zr ratio detected by ICP-OES analysis. This preferential leaching of yttrium leads to the formation of the thin rim of m-ZrO₂, detectable with Raman analysis.

As a consequence of Equation (1.5) SO_4^{2-} will react to O^{2-} ions and gaseous SO_3 . In addition gaseous H_2O from the atmosphere is expected to interact with Cl^- ions from the melt, leading to O^{2-} ions and gaseous HCl (Equ. 1.6). Accordingly, an enrichment of O^{2-} ions in the melt can be assumed which means an increasing basicity of the melt (Equ. 1.4). The continuously changing salt melt composition during the experiment, promotes a KCl dominated composition. In consequence the melting point of the melt assemblage shifts to higher temperatures (Fig. 4-30). This implies an increasing viscosity with time and hence a decreasing diffusivity within the melt. It is expected that the decreasing diffusivity leads to a gradual change within the melt. Near the surface the loss of Zn^{2+} continues to decrease the e.m.f. in the upper part. Near the bottom the e.m.f. values are more positive and in combination with an ongoing formation of O^{2-} ions, thus an increasing basicity of the melt, evoke as a driving force for the recrystallization of the zirconia (Fig. 4-32). The retarded incorporation of yttrium in the newly formed layer seems to be a consequence of its stronger basicity in comparison to zirconium. This leads to a longer retention of yttrium in the melt when facing increasing pO^{2-} values.

As Fig. 4-23 shows, the dissolution of zirconia is much faster at a smaller volume of salt. As the salt melt surface area is identical for all experiments the rate of Zn^{2+} loss is also similar. But the salt volume differs, leading to a slower decrease of the e.m.f. for a larger reservoir of salt compounds.

After each experiment the salts were dissolved within water to retain the zirconia beads. The observed amorphous $ZrO(OH)_2 \cdot nH_2O$ is obviously produced by the reaction of the dissolved Zr^{4+} ions. The retained amorphous powder of a zirconium-phase indicates that only a part of the dissolved zirconia recrystallizes at the surface of the zirconia beads.

Our experiments confirm the results of various studies on the hot corrosion behavior of zirconia (Yoshimura et al. 1986, Schacht et al. 1998, Sammonds et al. 2010, Hemberger et al. 2012, Craig et al. 2015), where a primary leaching of yttrium with subsequent phase transformation from t-ZrO₂ to m-ZrO₂ was observed under acidic or basic conditions. Our results also show the recrystallization of zirconia under basic conditions within a salt melt. This observation is in contradiction with the findings of Rao and coworkers (2012) who did not observe any phase transformation of their YSZ coating, even by using sulfate salts. This difference might be explained by the used amount of salt: Rao and coworkers (2012) sprayed a “near-saturated” salt solution on the YSZ surface, which was pre-heated

to 130°C. The immediately vaporizing water led to the formation of a homogeneous solidified salt layer. This procedure raises the question whether the sample was completely covered by a salt melt during the experiment, as the vaporization of the melt compounds with time has to be considered. In contrast, our beads were totally embedded in the salt melt during the whole experiment.

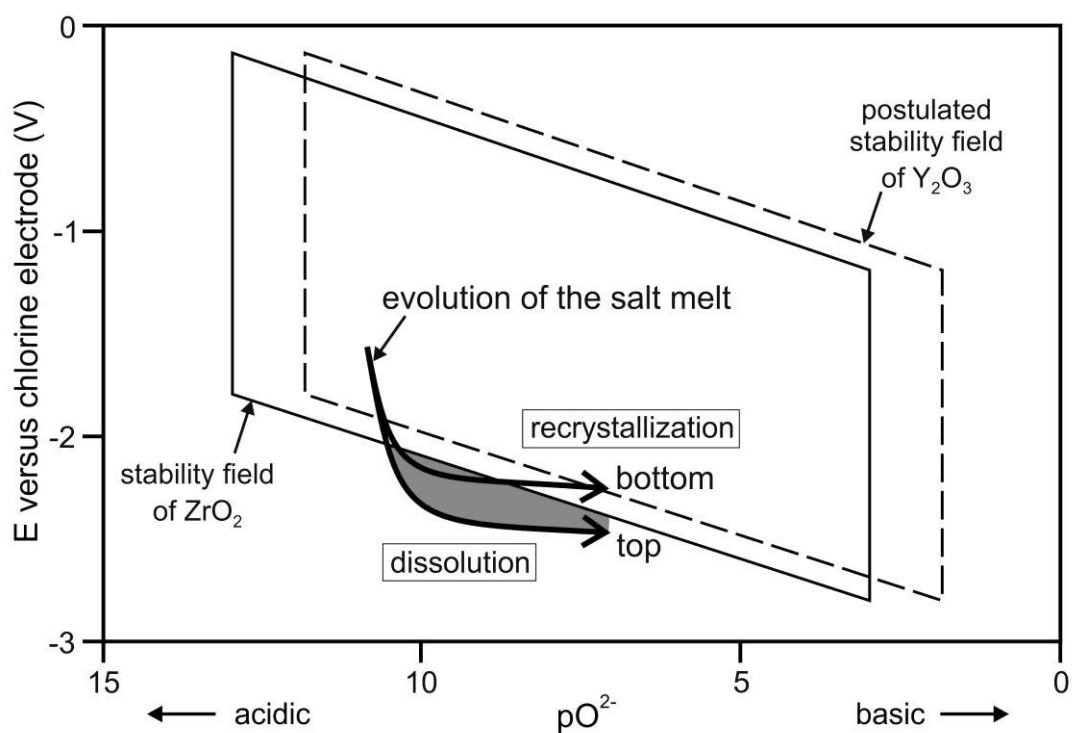


Fig. 4-32: Schematic illustration of the evolution of the salt melt, causing a dissolution and recrystallization of ZrO_2 as a consequence of a changing electromotive force and pO^{2-} value.

5 In-situ tests

Parts of this chapter are modified after Müller and coworkers (2016).

In order to evaluate the behavior of the zirconia-based multilayer coating under true operation conditions, coated test probes were placed in the WTE plant of Schwandorf, Germany. The sample location was in the second pass of the plant with an average flue gas temperature of 700 °C. One uncooled test probe was left for 14 days, three internally cooled (450 °C) test probes were left for 23 days within the plant.

5.1 In-situ test of an uncooled test probe at 700 °C

EPMA

All samples show an intact coating. Fig. 5-1 shows the sample from position 1 (lee). In the reflected light image an approximately 50 - 100 µm-thick area with significantly reduced porosity (7 % modified zirconia, 16 % unmodified zirconia) can be observed at the bottom of the zirconia top-coat, labeled as modified zirconia. The BSE image reveals that former cracks and open pores of the zirconia are filled with a secondary phase, which appears as a network of dark gray lines. By element mappings (Fig. 5-2) and EDX analyses, this newly formed chromium rich oxide with minor amounts of nickel and iron is assigned as metal oxide. The formation of metal oxide was accompanied by a replacement of the zirconia, as proved by a depletion of zirconium within the modified area in comparison to the unmodified area above. Additionally, small amounts of zinc can be found within the modified zirconia layer. Within the bond-coat a strong enrichment of sodium, potassium and chlorine is observable. Their common occurrence indicates the presence of sodium and potassium chloride salts. Sulfur (sulfate) was not detected in the element mappings.

XRF

Bulk analyses of the deposits from TP 1 show a continuously decreasing amount of SiO₂, Al₂O₃, Fe₂O₃, MgO, Na₂O, K₂O, TiO₂ from the tip of the test probe (pos. 1) to the region near the boiler wall (pos. 4) , while the concentration of CaO, Cl and partially for SO₃ increase (Tab. 5-1). The high LOI indicates a high amount of volatile compounds like carbonates, oxyhydroxides, chlorides and sulfates. This dominant presence of highly volatile compounds near the boiler wall might be explained by the lower temperature and hence higher condensation rate in comparison to the central part of the flue gas flow. Notable is the presence of zirconium within the deposits at all four positions with amounts between about 300 – 2100 ppm. A reasonable source for the zirconium is represented by the underlying coating. The highest value of 2100 ppm at pos. 1 correlates with the observed replacement of the zirconia within the top-coat, as shown in Fig. 5-2.

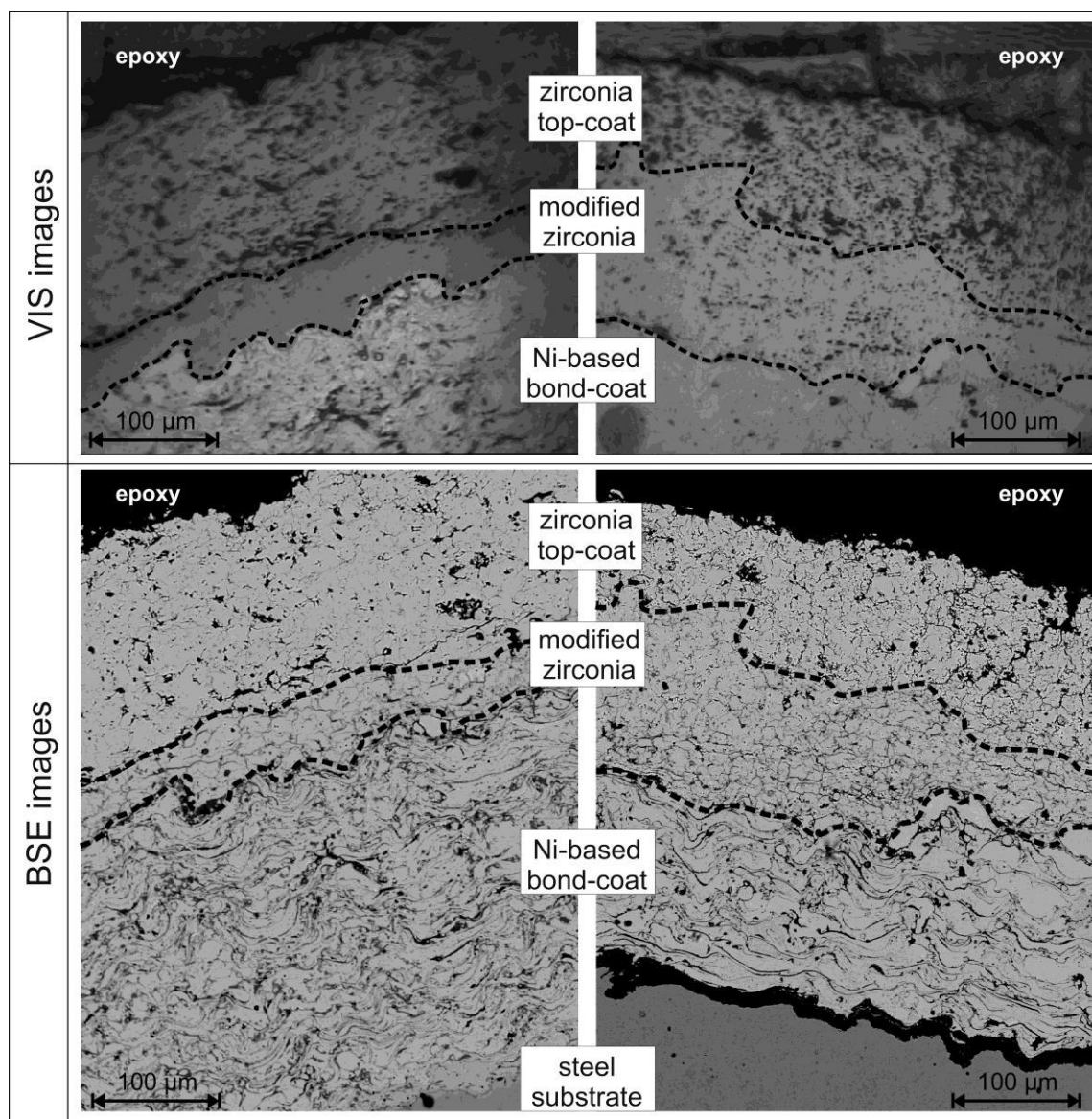


Fig. 5-1: Reflected light (VIS) and back-scattered electron (BSE) images of an uncooled test probe TP 1 (700 °C) (left) and a cooled test probe TP 2.1 (450 °C) (right).

XRD

Following solid phases were determined by XRD analyses of the deposit on the surface of the flue gas facing side (luf) of TP 1 (in decreasing amount): anhydrite (CaSO_4), melilite (gehlenite – $\text{Ca}_2\text{Al}[\text{AlSiO}_7]$), sylvite (KCl), spinel (franklinite – ZnFe_2O_4), magnesite (MgCO_3), halite (NaCl), cristobalite (SiO_2), quartz (SiO_2). These observations correspond well with XRF analysis showing high amounts of SiO_2 , Al_2O_3 , CaO , Na_2O , K_2O , SO_3 , Cl , MgO and Zn . On position 5 (lee) the observable phases differ (in decreasing amount): calcite (CaCO_3), quartz, anhydrite, halite, sylvite, cristobalite, hematite (Fe_2O_3).

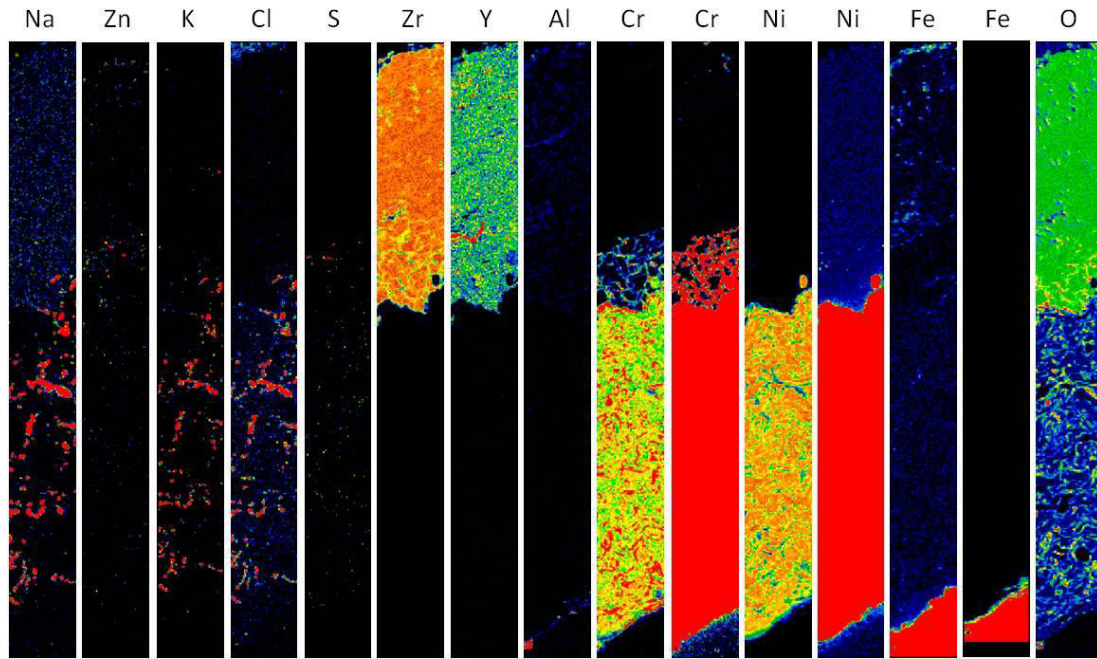


Fig. 5-2: Back-scattered electron (BSE) image in combination with element mappings of sodium, potassium, zinc, chlorine, iron, chromium, nickel, zirconium and oxygen of the multilayer coating from the lee-side of the uncooled test probe (TP 1 - 700 °C for 14 days). The element mapping of iron, chromium and nickel is separated into two parts with different scales in order to visualize the distribution of different amounts within the coating. Base length of each mapping is 60 μm .

Tab. 5-1: Results of XRF analyses from surface deposits of an uncooled test probe, placed for 14 days at 700 °C in a WTE plant. Sample positions 1 – 4 are shown in Fig. 3-5.

sample position	1	2	3	4
SiO ₂ (wt.-%)	15.58	14.50	13.42	11.37
Al ₂ O ₃	8.07	7.98	7.23	6.36
Fe ₂ O ₃ T	3.12	2.82	2.77	2.15
MnO	0.38	0.43	0.40	0.32
MgO	3.32	3.15	2.92	2.59
CaO	19.72	28.36	28.68	28.11
Na ₂ O	9.97	6.28	5.71	5.33
K ₂ O	5.97	4.12	3.84	3.82
TiO ₂	1.99	1.87	1.75	1.70
P ₂ O ₅	2.10	-	1.92	1.68
SO ₃	17.86	18.83	20.84	16.89
Cl	0.94	1.31	1.19	3.04
Ba	0.23	0.19	0.21	0.23
Cr	0.12	0.17	0.13	0.06
Cu	0.05	0.02	0.02	0.03
Ni	0.03	0.02	0.02	0.02
Pb	0.01	0.01	-	0.01
Rb	0.01	0.01	0.01	0.01
Sb	0.10	0.07	0.33	0.14
Sn	0.06	0.03	0.19	0.04
Sr	0.03	0.04	0.04	0.04
Zn	3.47	1.94	2.07	1.04
Zr	0.21	0.03	0.14	0.13
LOI	6.77	7.78	6.10	14.88
Total	100.11	99.96	99.93	99.99

5.2 In-situ test of a cooled test probe at 450 °C

The investigation of cross sections from TP 2.1-2.3 shows various stages of corrosion attack (Fig. 5-3): Only sample TP 2.2 does not show any detachment of the coating. In contrast, samples TP 2.1 and TP 2.3 expose a delamination of the multilayer coating from the steel substrate on the luv-side. On bare steel substrate surfaces a massive layer of metal oxide is observable. Due to EDX analyses this layer consists of mainly iron oxide containing minor amounts of chromium, nickel, locally molybdenum as well as sodium and potassium. The presence of sodium and potassium might represent adsorbed Na_2O and K_2O on the metal oxide surface. On the lee-side of sample TP 2.1 an approximately 50 – 250 μm thick modified area is exposed at the bottom of the zirconia top-coat similar to that of TP 1 (Fig. 5-1). In the reflected light mode image this area shows less porosity in comparison to the overlaying YSZ (9 % modified zirconia, 19 % unmodified zirconia). The BSE image shows clearly, that the formerly open pores and cracks of the zirconia top-coat are filled by a secondary phase. Element mappings of this area (Fig. 5-4) reveal the presence of chromium, nickel, iron and oxygen together with minor amounts of zinc within these cracks, but no zirconium. In contrast to the uncooled test probe, this newly formed metal oxide contains significantly more nickel and iron. Within the bond-coat an additional iron enrichment can be observed containing only traces of sodium, potassium and chlorine. Between the steel substrate and the nickel-based bond-coat a layer of sodium, potassium and iron oxides has formed (see Fig. 5-4) similar to the observed oxide layer on top of an exposed steel substrate discussed above.

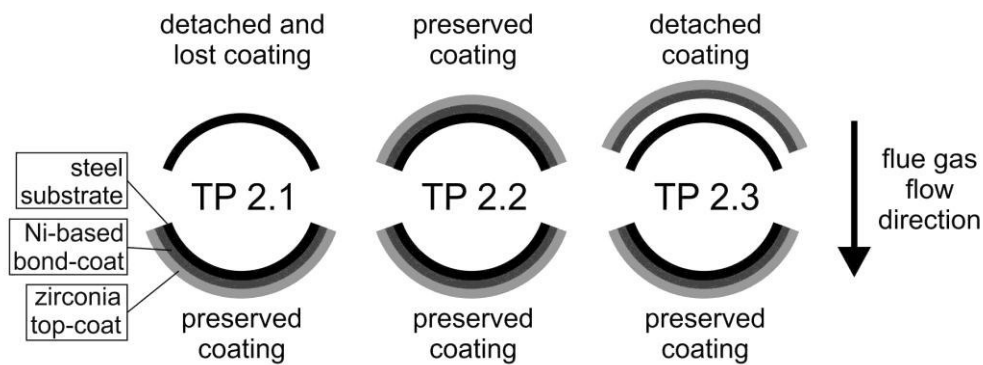


Fig. 5-3: Condition of the coatings of the cooled test probes (TP 2.1, TP 2.2, TP 2.3) after 23 days within a WTE plant. Samples were prepared from the luv- and lee-side.

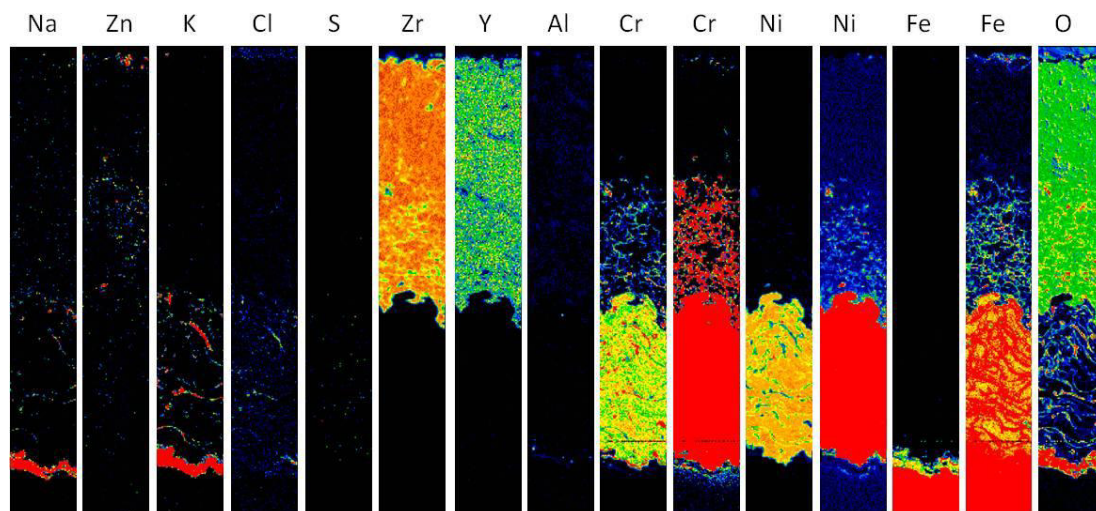


Fig. 5-4: Back-scattered electron (BSE) image in combination with element mappings of sodium, potassium, zinc, chlorine, iron, chromium, nickel, zirconium and oxygen of the multilayer coating from the lee-side of a cooled test probe (TP 2.1 - 450 °C for 23 days). The element mapping of iron, chromium and nickel is separated into two parts with different scales in order to visualize distribution of different amounts within the coating. Base length of each mapping is 60 μm .

5.3 Discussion of in-situ tests

All test probes - at 450 °C as well as 700 °C - show a modified area at the bottom of the zirconia top-coat containing newly formed metal oxides. This modification was found on the lee-side of the test probes. Five main differences can be summarized between TP 1 and TP 2.1 (Tab. 5-2):

1. The modified area at the bottom of the zirconia top-coat is distinctly thinner for TP 1 (50 – 100 μm) in contrast to TP 2.1 (50 – 250 μm).
2. The newly formed metal oxide along the grain boundaries within the zirconia top-coat of TP 2.1 contains more nickel and iron as in TP 1.
3. TP 1 contains noticeable amounts of sodium and potassium chloride salts within the bond-coat, while TP 2.1 shows only small amounts of them.
4. TP 2.1 exhibits a significant enrichment of iron within the bond-coat.
5. TP 2.1 shows a newly formed metal oxide layer between the steel substrate and the bond-coat, which is not observable for TP 1.

The test duration of TP 2.1 (23 days) was significantly longer than that of TP 1 (14 days) and TP 2.1 exhibits a thinner multilayer coating in contrast to TP 1. The thicker coating of TP 1 causes a longer diffusion time for aggressive species from the flue gas to reach potential reaction partners, represented by the metal bond-coat and the steel substrate. In combination with the shorter test duration of TP 1, a retarded corrosion can be assumed. Thus, the thicker modified area within the zirconia top-coat and the newly formed layer between steel substrate and bond-coat of TP 2.1 indicates a further progress of corrosion in contrast to TP 1. Additionally, the lower surface temperature of TP 2.1 promotes the condensation of solid phases, e.g. salts. This in turn can lead to the formation of low-melting (heavy metal containing) salt melts, which can enhance the corrosion as well.

Tab. 5-2: Summarized observations for the in-situ test probes.

sample		TP 1	TP 2.1
experiment duration		14 days	23 days
temperature		700 °C	450 °C
zirconia top-coat	thickness of the modified zirconia layer	50 - 100 µm	50 - 250 µm
	composition of the metal oxide within the modified zirconia layer	Cr, (±Ni), (±Fe)	Cr, Ni, (±Fe)
Ni-based bond-coat	salt amount within the bond-coat	significant amounts of NaCl & KCl	small amounts of NaCl & KCl
	iron amount within the bond-coat	non-existent	moderate amount
newly formed iron-oxide layer between bond-coat and steel substrate		non-existent	existent, +Na, +K

Based on these observations the following corrosion process can be concluded: As shown by XRD analysis, the deposit contains significant amounts of sodium and potassium chloride salts (halite and sylvite) together with sulfates (anhydrite) and zinc containing species. The combined occurrence of chloride and sulfate salts can lead to the formation of low melting salt melts, penetrating the coating through open pores and cracks. Due to aggressive conditions within chloride-sulfate salt melts YSZ tends to dissolve (Müller & Heuss-Aßbichler 2016). Based on the presence of about 300 – 2100 ppm zirconium within the deposits on top of the coating, a partial dissolution with subsequent removal of the dissolved zirconia can be assumed. Chlorine from the combustion gases as well as from the dissociation of the salts, presumably initiates a corrosion process of the metallic bond-coat as well as the steel substrate, known as “active oxidation” (Grabke et al. 1995). This corrosion process is based on the formation of metal chlorides. Due to the high vapor pressures of such chlorides they vaporize easily and are thus removed from their origin. When facing an increased oxygen partial pressure at or on their way to the coating surface, they are transformed to metal oxides, releasing the chlorine, which can participate again in the corrosion of the metal. The permanent presence of chlorine and oxygen within the flue gas of a WTE plant can lead to a continuing corrosion of metallic materials. The ongoing formation of metal oxides can cause a detachment of the coating from the substrate, as observable for some of the test probes described herein.

6 Conclusion

Parts of this chapter are modified after Müller & Heuss-Aßbichler (2016) and Müller and coworkers (2016).

Lab-scale experiments with coated steel cylinders were done under an extremely aggressive gas atmosphere to test their corrosion resistance. Samples with a multilayer coating of a nickel-based bond-coat and an YSZ top-coat show no detachment of the coating. For the experiment at 700 °C a partial densification of the zirconia top-coat was achieved. The results clearly show that this densification process can happen without any additional zirconium in the gas flow. This means that the range of the conditions leading to a densification proposed by Fehr and coworkers (2012), Masset and coworkers (2013) and Ye (2016) can be enlarged. Presumably the densification process is based on a gas phase transport of the zirconium in combination with grain growth through sintering, accompanied by a partial phase transformation from tetragonal to monoclinic zirconia. The latter one is accompanied by a volume increase of approximately 4 %, representing a sufficient amount to close microcracks in the YSZ top-coat.

The results of the salt melt experiments showed a dissolution of the zirconia, followed by a recrystallization of zirconia on top of the formerly attacked surface. The process of dissolution can be attributed to a shift of the electromotive force within the salt melt to more negative values. The dissociation of the salt compounds (KCl, K₂SO₄, ZnCl₂, ZnSO₄) in their molten state leads to a preferential loss of Zn²⁺. This process shifts the electromotive force to more negative values, causing the dissolution of ZrO₂. The molten salts also release Cl⁻ and SO₄²⁻ ions. Both, the reaction of Cl⁻ with water from the atmosphere and the transformation of SO₄²⁻ to SO₃ release O²⁻ ions. This enrichment of O²⁻ ions leads to an increasing basicity of the melt, responsible for the recrystallization of ZrO₂.

This observation has consequences with respect to an application of zirconia anti-corrosion coatings in WTE plants where salt melts are present. Two possible scenarios have to be considered: (a) zirconia may get dissolved and mobilized by the melt or (b) depending on the melt composition zirconia may recrystallize almost within the same area of the coating. In case (a) a removal of the dissolved zirconia would finally lead to a degradation and failure of the ceramic coating. However, for case (b) this process enables the coating system to act as a self-healing coating. Small cracks and open pores can be infiltrated by the zirconium-containing salt melt, followed by a recrystallization of ZrO₂ on the surface of the surrounding zirconia substrate, subsequently closing the gap. Since the operation temperature of these coatings in WTE plants will not rise above 850 °C, the presence of m-ZrO₂ is not critical with respect to a temperature-driven phase transformation to t-ZrO₂.

In-situ experiments inside a WTE plant with test probes coated with a multilayer coating of a nickel-based bond-coat and an YSZ top-coat show distinct corrosion phenomena. A detachment of the coating was observed for cooled test probes, which represent the actual conditions of use as e.g. superheater tube. A partial dissolution of the zirconia top-coat

enables an enhanced penetration of the coating by aggressive gases, leading to the formation of newly formed metal oxides within the YSZ top-coat and between bond-coat and steel substrate.

Studies from Wöllmer and coworkers (2015) have shown an improved corrosion resistance of solvothermally pretreated test probes. This pretreatment might follow a routine, described herein for the lab-scale experiments. The existence of a densified zirconia layer can reduce the diffusion of aggressive gases, hence reducing the corrosion of the steel substrate. Thus, a pretreatment of the ceramic top-coat seems to be a necessary step in order to enable the multilayer coating to act as a long-term corrosion resistant coating for application in WTE plants. Due to the small thickness of the APS-applied multilayer coating, this coating layout can be a cost-efficient alternative for currently used 2 – 3 mm thick nickel-based weld overlays. In particular membrane walls and superheater tubes come into focus of interest, since they are object of severe corrosion attack within a WTE plant.

7 Outlook

The results of the experiments revealed unexpected new insights into the densification process. This necessitates the construction of a new experimental setup, leading to a delay and rearrangement of the planned experiments. The following points are still open and need to be solved, before this densification process can be seen as a reliable method, improving the anti-corrosion properties of YSZ coatings on heat exchange tubes within WTE plants:

- 1) Performing a time series of one, two and three days under experimental conditions that led to a densification (TS-031, TS-055, TS-059), in order to investigate the densification rate and the evolution of the bond-coat as well as the steel substrate.
- 2) Experiments with various salt compositions. Sodium salts seem to be a promising candidate to enhance the densification process. The substitution of zinc salts would be worthwhile, with respect to costs and environmental issues.
- 3) In-situ experiments with pretreated test probes within a WTE plant, to investigate the long-term behavior of pretreated (densified) coatings under real operation conditions.

With respect to a technical application, it is favorable to lower the costs. This can be achieved through a substitution of the expensive yttria-stabilized zirconia by e.g. calcia-stabilized zirconia. These new material combinations, of course, would imply additional lab-scale and in-situ experiments to verify the densification process as well as the anti-corrosion properties of the coating. A first test with test probes, coated with mixtures of YSZ and Al_2O_3 as top-coat were already performed and yielded promising results, regarding their anti-corrosion performance and long-term stability under real operation conditions within a WTE plant (Wöllmer et al. 2015). Further tests need to be done to verify these results.

Since this densification is accompanied by an improved adhesion of the top-coat onto the bond-coat (Fehr et al. 2012, Masset et al. 2013, Ye 2016), this process can also be used to improve the mechanical and anti-corrosion properties of YSZ coatings for other applications, e.g. chemical industry or automotive industry. An application of densified ceramic coatings in gas turbines as e.g. thermal barrier coating (TBC) would be unfavorable, since a high porosity is required to act as a thermal insulating layer.

References

- Ahmadi-Pidani, R., Shoja-Razavi, R., Mozafarinia, R. & Jamali, H., 2012. Evaluation of hot corrosion behavior of plasma sprayed ceria and yttria stabilized zirconia thermal barrier coatings in the presence of $\text{Na}_2\text{SO}_4+\text{V}_2\text{O}_5$ molten salt. *Ceramics International*, 38, 6613-6620.
- Aleßio, H.-P., 2014. Korrosion ohne Chemie? Erläuterungen zum Hintergrund und zur Nutzung von Korrosionsdiagrammen. In: K. J. Thomé-Kozmiesky & M. Beckmann, Eds. *Energie aus Abfall*. Neuruppin: TK Verlag, 475.
- Aßbichler, D., Heuss-Aßbichler, S., Müller, D., Kunzmann, T., 2016. Volcanic sanidinites: an example for the mobilization of high field strength elements (HFSE) in magmatic systems. *Geophysical Research Abstracts*, 18, EGU2016-16894.
- Aßbichler, D., Müller, D. & Heuss-Aßbichler, S., 2017. Learning from nature: Solvothermal crystallization of zirconium in volcanic ejecta and its relevance for technical application. *Procedia Earth and Planetary Science*, 17, 570-573.
- Ayris, P. M., Cimarelli, C., Delmelle, P., Wadsworth, F. B., Vasseur, J., Suzuki, Y. J. & Dingwell, D. B., 2015. A novel apparatus for the simulation of eruptive gas-rock interactions. *Bulletin of Volcanology*, 77, 104-109.
- Azarmi, F. & Salimijazi, H. R., 2015. Grain growth and pore elimination in Inconel 625 deposited by APS. *Surface and Coatings Technology*, 268, 3-6.
- Badwal, S. P. S., 1992. Zirconia-based solid electrolytes: microstructure, stability and ionic conductivity. *Solid State Ionics*, 52, 23-32.
- Belevi, H., 2000. Factors that Control the Quality of Municipals Solid Waste Incineration Residues. In: R. Dhir, T. Dyer & K. Paine, Eds. *Sustainable Construction: Use of incinerator ash*. London: Thomas Telvord Publishing, 19-32.
- Bendix, D., Tegeder, G., Crimmann, P., Metschke, J. & Faulstich, M., 2008. Development of thermal sprayed layers for high temperature areas in waste incineration plants. *Materials and Corrosion*, 59, 389-392.
- Bilitewski, B. & Härdtle, G., 2013. Abfallwirtschaft. Berlin Heidelberg: Springer-Verlag.
- Bloom, H., 1967. The Chemistry of Molten Salts. New York: W.A. Benjamin.
- Bohé, A. E., Andrade Gamboa, J. J., Lopasso, E. M. & Pasquevich, D. M., 1996. Zirconium recovery from zircaloy shavings. *Journal of Materials Science*, 31, 3469-3474.
- Bohé, A. E. & Pasquevich, D. M., 1997. A Novel Method for the Synthesis of Zirconia Powder. *High Temperature and Materials Science*, 37, 143-158.

- Bornstein, N. S. & DeCrescente, M. A., 1971. The role of sodium in the accelerated oxidation phenomenon termed sulfidation. *Metallurgical Transactions*, 2, 2875-2883.
- Brandon, J. R. & Taylor, R., 1991. Phase stability of zirconia-based thermal barrier coatings Part I. Zirconia-yttria alloys. *Surface and Coatings Technology*, 46, 75-90.
- Breitschwerdt, S., 2015. Comparison of analytical methods to determine the porosity of ceramic coatings, MSc thesis, LMU Munich.
- Brinkiene, K. & Kezelis, R., 2004. Correlations between processing parameters and microstructure for YSZ films produced by plasma spray technique. *Journal of the European Ceramic Society*, 24, 1095-1099.
- Cai, J., Guan, Q., Yang, S., Yang, S. & Wang, Z., 2014. Microstructural characterization of modified YSZ thermal barrier coatings by high-current pulsed electron beam. *Surface and Coatings Technology*, 254, 187-194.
- Chen, Z., Mabon, J., Wen, J.-G. & Trice, R., 2009. Degradation of plasma-sprayed yttria-stabilized zirconia via ingress of vanadium oxide. *Journal of the European Ceramic Society*, 29, 1647-1656.
- Cherginets, V. L., 2005. Oxoacidity: Reactions of oxo-compounds in ionic solvents. *Chemical Kinetics*, 41, 350.
- Clarke, D. R., Oechsner, M. & Padture, N. P., 2012. Thermal-barrier coatings for more efficient gas-turbine engines. *MRS Bulletin*, 37, 891-898.
- Claussen, N., 1985. Strengthening Strategies for ZrO₂-toughened Ceramics at High Temperatures. *Materials Science and Engineering*, 71, 23-38.
- Coda, B., Aho, M., Berger, R. & Hein, K. R. G., 2001. Behavior of chlorine and enrichment of risky elements in bubbling fluidized bed combustion of biomass and waste assisted by additives. *Energy & Fuels*, 15, 680-690.
- Combes, R., Vedel, J. & Trémillon, B., 1970. Realisation D'Une Electrode Indicatrice D'Ions Oxyde Dans Les Sels Fondus Au Moyen D'Electrolytes Solides. *Analytical Letters*, 3, 523-529.
- Craig, M., Ndamka, N. L., Wellman, R. G. & Nicholls, J. R., 2015. CMAS degradation of EB-PVD TBCs: The effect of basicity. *Surface and Coatings Technology*, 270, 145-153.
- Deshpande, S., Sampath, S. & Zhang, H., 2006. Mechanism of oxidation and its role in microstructural evolution of metallic thermal spray coatings - Case study for Ni-Al. *Surface and Coatings Technology*, 200, 5395-5406.
- Deuerling, C., Maguhn, J., Nordsieck, H., Benker, B., Zimmermann, R. & Warnecke, R., 2009. Investigation of the Mechanisms of Heat Exchanger Corrosion in a

- Municipal Waste Incineration Plant by Analysis of the Raw Gas and Variation of Operating Parameters. *Heat Transfer Engineering*, 30, 822-831.
- Drazin, J. W. & Castro, R. H., 2015. Phase Stability in Nanocrystals: A Predictive Diagram for Yttria-Zirconia. *Journal of the American Ceramic Society*, 98, 1377-1384.
- Elliott, P., Tyreman, C. J. & Prescott, R., 1985. High Temperature Alloy Corrosion by Halogens. *Journal of Metals*, 37, 20-23.
- Essene, E. J., Henderson, C. E. & Livingstone, A., 2006. The missing sulphur in mattheddleite, sulphur analysis of sulphates and paragenetic relations at Leadhills, Scotland. *Mineralogical Magazine*, 70, 265-280.
- Evans, A. G. & Cannon, R. M., 1986. Toughening of Brittle Solids by Martensitic Transformations. *Acta Metallurgica*, 34, 761-800.
- Fang, Q., Sidky, P. S. & Hocking, M. G., 1999. Erosion and corrosion of PSZ-zirconia and the t-m phase transformation. *Wear*, 233, 615-622.
- Faulstich, M., Jörgens, L., Tartler, D., Fehr, K. T. & Heuss-Aßbichler, S., 2001. Vermeidung der Korrosion von Feuerfestmaterial in Abfallverbrennungsanlagen durch Additive, Harburg: Märker Umwelttechnik GmbH.
- Fehr, K. T., Ye, Y., Faulstich, M., Weih, C. & Wolf, G., 2012. Ein neues Verfahren zur Optimierung oxidkeamischer Schutzschichten. In: M. Faulstich, M. Geiger, H. Kukla & G. Wolf, Eds. *Moderne Beschichtungen zum Verschleißschutz von Werkzeugen*. Sulzbach-Rosenberg: DORNER PrintConcept GmbH & Co. KG.
- Fu, Y., Batchelor, A. W., Xing, H. & Gu, Y., 1997. Wear behaviour of laser-treated plasma-sprayed ZrO₂ coatings. *Wear*, 210, 157-164.
- Ganesan, P., Renteria, C. M. & Crum, J. R., 1991. Versatile corrosion resistance of Inconel alloy 625 in various aqueous and chemical processing environments. In: E. A. Loria, Ed. *Superalloys 718, 625 and various derivatives*. The Minerals, Metals & Materials Society, 663-680.
- Garvie, R. C., Hannink, R. H. & Pascoe, R. T., 1975. Ceramic steel?. *Nature*, 258, 703-704.
- Goebel, J. A. & Pettit, F. S., 1970. The influence of sulfides on the oxidation behavior of nickel-base alloys. *Metallurgical Transactions*, 1, 3421-3429.
- Grabke, H. J., Reese, E. & Spiegel, M., 1995. The effects of chlorides, hydrogen chloride, and sulfur dioxide in the oxidation of steels below deposits. *Corrosion Science*, 37, 1023-1043.
- Habibi, M. H. & Guo, S. M., 2015. The hot corrosion behavior of plasma sprayed zirconia coatings stabilized with yttria, ceria, and titania in sodium sulfate and vanadium oxide. *Materials and Corrosion*, 66, 270-277.

- Hannink, R. H., Kelly, P. M. & Muddle, B. C., 2000. Transformation toughening in zirconia-containing ceramics. *Journal of the American Ceramic Society*, 83, 461-487.
- Hauffe, K. & Hinrichs, J., 1970. Hochtemperaturkorrosion von Nickel in Chlor und Chlor-Sauerstoffgemischen. *Werkstoffe und Korrosion*, 21, 954-965.
- Hayashi, H., Saitou, T., Maruyama, N., Kawamura, K. & Mori, M., 2005. Thermal expansion coefficient of yttria stabilized zirconia for various yttria contents. *Solid State Ionics*, 176, 613-619.
- Heiroth, S., Frison, R., Rupp, J. L. M., Lippert, T., Barthazy Meier, E. J., Müller Gubler, E., Döbeli, M., Conder, K., Wokaun, A. & Gauckler, L. J., 2011. Crystallization and grain growth characteristics of yttria-stabilized zirconia thin films grown by pulsed laser deposition. *Solid State Ionics*, 191, 12-23.
- Hemberger, Y., Berthold, C. & Nickel, K. G., 2012. Wetting and corrosion of yttria stabilized zirconia by molten slags. *Journal of the European Ceramic Society*, 32, 2859-2866.
- Heuer, A. H., 1987. Transformation Toughening in ZrO₂-Containing Ceramics. *Journal of the American Ceramic Society*, 70, 689-698.
- Hunsinger, H. & Andersson, S., 2014. The potential of SO₂ for reducing corrosion in WtE plants. *Journal of Material Cycles and Waste Management*, 16, 657-664.
- Ihara, Y., Ohgame, H., Sakiyama, K. & Hashimoto, K., 1982. The Corrosion Behaviour of Fe-Ni Alloys in Hydrogen Chloride Gas and Gas Mixtures of Hydrogen Chloride and Oxygen at High Temperatures. *Transactions of the Japan Institute of Metals*, 23, 682-692.
- Ishitsuka, T. & Nose, K., 2002. Stability of protective oxide films in waste incineration environment - solubility measurement of oxides in molten chlorides. *Corrosion Science*, 44, 247-263.
- Jacobson, N. S. & Myers, D. L., 2011. Active Oxidation of SiC. *Oxidation of Metals*, 75, 1-25.
- Jena, P. K. & Brocchi, E. A., 1997. Metal Extraction Through Chlorine Metallurgy. *Mineral Processing and Extractive Metallurgy Review*, 16, 211-237.
- Karger, M., Vaßen, R. & Stöver, D., 2011. Atmospheric plasma sprayed thermal barrier coatings with high segmentation crack densities: Spraying process, microstructure and thermal cycling behavior. *Surface and Coatings Technology*, 206, 16-23.
- Kassebohm, B., 1989. Prevention of corrosion by improved incineration quality. *Werkstoffe und Korrosion (Materials and Corrosion)*, 40, 153-156.

- Krogstad, J. A., Krämer, S., Lipkin, D. M., Johnson, C. A., Mitchell, D. R. G., Cairney, J. M. & Levi, C. G., 2011. Phase Stability of t'-Zirconia-Based Thermal Barrier Coatings: Mechanistic Insights. *Journal of the American Ceramic Society*, 94, 168-177.
- Kroll, W., 1937. Verformbares Titan und Zirkon. *Zeitschrift für anorganische und allgemeine Chemie*, 234, 42-50.
- Landon, G. J. & Ubbelohde, A. R., 1956. Volume changes on melting ionic crystals. *Transactions of the Faraday Society*, 52, 647-651.
- Lee, H.-Y. & Baik, K.-H., 2009. Comparison of corrosion resistance between Al₂O₃ and YSZ coatings against high temperature LiCl-Li₂O molten salt. *Metals and Materials International*, 15, 783-787.
- Lee, Y. Y. & McNallan, M. J., 1987. Ignition of Nickel in Environments Containing Oxygen and Chlorine. *Metallurgical Transactions A*, 18A, 1099-1107.
- Leib, E. W., Vainio, U., Pasquarelli, R. M., Kus, J., Czaschke, C., Walter, N., Janssen, R., Müller, M., Schreyer, A., Weller, H. & Vossmeier, T., 2015. Synthesis and thermal stability of zirconia and yttria-stabilized zirconia microspheres. *Journal of Colloid and Interface Science*, 448, 582-592.
- Li, P., Chen, I.-W. & Penner-Hahn, J. E., 1994. Effect of dopants on zirconia stabilization - An X-ray absorption study: I, Trivalent Dopants. *Journal of the American Ceramic Society*, 77, 118-128.
- Lushnaya, N. P., Evseeva, N. N. & Vereshchetina, I. P., 1956. Physical properties of salt melts and the nature of their structural parts. *Russian Journal of Inorganic Chemistry*, 1, 35-41.
- Magel, G., Molitor, D., Bratzdrum, C., Koch, M. & Aleßio, H.-P., 2012. Wie kommt die Wärme ins Rohr? - Korrosion ist oftmals ein Symptom hoher Wärmestromdichte. In: K. J. Thomé-Kozmiensky & M. Beckmann, Eds. *Energie aus Abfall*. Neuruppin: TK Verlag, 373.
- Masset, P. J., Faulstich, M., Fehr, K. T., Weih, C., Wolf, G. & Ye, Y., 2013. Chemical densification of oxide based coatings for high temperature wear and corrosion resistance. *ECS Transactions*, 50, 109-116.
- Mauer, G., Sebold, D., Vaßen, R. & Stöver, D., 2012. Improving Atmospheric Plasma Spraying of Zirconate Thermal Barrier Coatings Based on Particle Diagnostics. *Journal of Thermal Spray Technology*, 21, 363-371.
- Merle-Méjean, T., Barberis, P., Ben Othmane, S., Nardou, F. & Quintard, P. E., 1998. Chemical Forms of Hydroxyls on/in Zirconia: An FT-IR Study. *Journal of the European Ceramic Society*, 18, 1579-1586.

- Montgomery, M., Hansson, A. N., Jensen, S. A., Vilhelmsen, T. & Nielsen, N. H., 2013. In-situ corrosion testing of various nickel alloys at Mabjerg waste incineration plant. *Materials and Corrosion*, 64, 14-25.
- Mukherjee, T. K. & Gupta, C. K., 1983. Base Metal Resource Processing by Chlorination. *Mineral Processing Technology Review*, 1, 111-153.
- Müller, D. & Heuss-Aßbichler, S., 2016. Behavior of yttria-stabilized zirconia in the presence of molten salts: Part 1 - Dissolution and recrystallization phenomena. *Journal of the European Ceramic Society*, 36, 3495-3503.
- Müller, D., Wöllmer, S., Aßbichler, D., Murer, M. J., Heuss-Aßbichler, S., Rieger, K., Hill, H., Härtel, C. & Masset, P. J., 2016. High temperature corrosion studies of a zirconia coating: Implications for waste-to-energy (WTE) plants, *Coatings*, 6, 36.
- Naguib, H. M. & Kelly, R., 1970. The crystallization of amorphous ZrO_2 by thermal heating and by ion bombardment. *Journal of Nuclear Materials*, 35, 293-305.
- Nishikata, A., Numata, H. & Tsuru, T., 1991. Electrochemistry of molten salt corrosion. *Materials Science and Engineering*, A146, 15-31.
- Oh, J. M., McNallan, M. J., Lai, G. Y. & Rothman, M. F., 1986. High Temperature Corrosion of Superalloys in an Environment Containing Both Oxygen and Chlorine. *Metallurgical Transactions A*, 17A, 1087-1094.
- Park, S. Y., Kim, J. H., Kim, M. C., Song, H. S. & Park, C. G., 2005. Microscopic observation of degradation behavior in yttria and ceria stabilized zirconia thermal barrier coatings under hot corrosion. *Surface and Coatings Technology*, 190, 357-365.
- Pasquevich, D. M., Lovey, F. & Caneiro, A., 1989. Structural and Microstructural Changes in Zirconia in Dilute Chlorine Atmosphere. *Journal of the American Ceramic Society*, 72, 1664-1667.
- Pawlowski, J., Fehr, K. T. & Faulstich, M., 2006. Untersuchungen zum Korrosionsverhalten von nitridgebundenen SiC-Platten in Müll- und Biomasseverbrennungsanlagen. *Müll und Abfall*, 8, 434-440.
- Presser, V., Keuper, M., Berthold, C. & Nickel, K. G., 2009. Experimental Determination of the Raman Sampling Depth in Zirconia Ceramics. *Applied Spectroscopy*, 63, 1288-1292.
- Presser, V. & Nickel, K. G., 2008. Silica on Silicon Carbide. *Critical Reviews in Solid State and Materials Sciences*, 33, 1-99.
- Rajendran, R., Raja, V. S., Sivakumar, R. & Srinivasa, R. S., 1995. Reduction of interconnected porosity in zirconia-based thermal barrier coating. *Surface and Coatings Technology*, 73, 198-200.

- Rao, S., Frederick, L. & McDonald, A., 2012. Resistance of Nanostructured Environmental Barrier Coatings to the Movement of Molten Salts. *Journal of Thermal Spray Technology*, 21, 887-899.
- Rapp, R. A., 2002. Hot corrosion of materials: a fluxing mechanism?. *Corrosion Science*, 44, 209-221.
- Rapp, R. A. & Zhang, Y.-S., 1994. Hot corrosion of materials: Fundamental studies. *JOM*, 46, 47-55.
- Readey, M. J. & Readey, D. W., 1986. Sintering of ZrO_2 in HCl Atmospheres. *Journal of the American Ceramic Society*, 69, 580-582.
- Reddy, N. & Gandhi, A. S., 2013. Molten salt attack on t' yttria-stabilised zirconia by dissolution and precipitation. *Journal of the European Ceramic Society*, 33, 1867-1874.
- Richter, F., 2010. Die physikalischen Eigenschaften der Stähle - Das "100-Stähle-Programm", Mühlheim an der Ruhr.
- Ruff, O. & Ebert, F., 1929. Beiträge zur Keramik hochfeuerfester Stoffe. 1. Die Formen des Zirkondioxyds. *Zeitschrift für anorganische und allgemeine Chemie*, 180, 19-41.
- Sammonds, P., McGuire, W. & Edwards, S., 2010. Volcanic Hazard from Iceland: Analysis and Implications of the Eyjafjallajökull Eruption, London: UCL Institute for Risk and Disaster Reduction.
- Sarkar, D., Mohapatra, D., Ray, S., Bhattacharyya, S., Adak & Mitra, N., 2006. Synthesis and characterization of sol-gel derived ZrO_2 doped Al_2O_3 nanopowder. *Ceramics International*, 33, 1275-1282.
- Schacht, M., Boukis, N., Dinjus, E., Ebert, K., Janssen, R., Meschke, F & Claussen, N., 1998. Corrosion of zirconia ceramics in acidic solutions at high pressures and temperatures. *Journal of the European Ceramic Society*, 18, 2373-2376.
- Schmidl, W., 2009. Erfahrungen mit thermisch gespritzten Schichten als Korrosionsschutz auf Wärmetauscherflächen in reststoffbefeueerten Dampfzeugern. In: K. J. Thomé-Kozmiensky & M. Beckmann, Eds. *Energie aus Abfall*. Neuruppin: TK Verlag, 593.
- Shankar, A. R., Mudali, U. K., Sole, R., Khatak, H. S. & Raj, B., 2008. Plasma-sprayed yttria-stabilized zirconia coatings on type 316L stainless steel for pyrochemical reprocessing plant. *Journal of Nuclear Materials*, 372, 226-232.
- Shojai, F. & Mäntylä, T. A., 2001a. Chemical stability of yttria doped zirconia membranes in acid and basic aqueous solutions: chemical properties, effect of annealing and ageing time. *Ceramics International*, 27, 299-307.

- Shojai, F. & Mäntylä, T. A., 2001b. Structural stability of yttria doped zirconia membranes in acid and basic aqueous solutions. *Journal of the European Ceramic Society*, 21, 37-44.
- Siebert, B., Funke, C., Vaßen, R. & Stöver, D., 1999. Changes in porosity and Young's Modulus due to sintering of plasma sprayed thermal barrier coatings. *Journal of Materials Processing Technology*, 92-93, 217-223.
- Simons, E. L., Browning, G. V. & Liebhafsky, H. A., 1955. Sodium sulfate in gas turbines. *Corrosion*, 11, 17-26.
- Spiegel, M., 1999. Salt melt induced corrosion of metallic materials in waste incineration plants. *Materials and Corrosion*, 50, 373-393.
- Spiegel, M., 2000. Influence of gas phase composition on the Hot Corrosion of steels and nickel-based alloys beneath a (Ca-Na-K)-sulfate mixture containing PbSO₄ and ZnSO₄. *Materials and Corrosion*, 51, 303-312.
- Spiegel, W., Herzog, T., Magel, G., Müller, W., Schmidl, W. & Albert, F. W., 2013. Korrosion in Abfallverbrennungsanlagen. In: *Dampferzeugerkorrosion*. Freiberg: SAXONIA Standortentwicklungs- und -verwaltungsgesellschaft, 9-95.
- Steinmetz, L., 2015. Investigation of Corrosion Resistance of Solvothermally Treated Samples under Defined Gas Atmospheres, MSc thesis, LMU Munich.
- Szkaradek, K. K., 2010. Laser melted ZrO₂-Y₂O₃ thermal barrier obtained by plasma spraying method. *Journal of Alloys and Compounds*, 505, 516-522.
- Szymanski, K., Hernas, A., Moskal, G. & Myalska, H., 2015. Thermally sprayed coatings resistant to erosion and corrosion for power plant boilers - A review. *Surface and Coatings Technology*, 268, 153-164.
- Tammann, G., 1926. Die Temperatur des Beginns innerer Diffusion in Kristallen. *Zeitschrift für anorganische und allgemeine Chemie*, 157, 321-325.
- Umweltbundesamt - UBA, 2016. Thermische Behandlung. <http://www.umweltbundesamt.de/themen/abfall-ressourcen/entsorgung/thermische-behandlung>, (last access 03.04.2016).
- Vaidya, A., Srinivasan, V., Streibl, T., Friis, M., Chi, W. & Sampath, S., 2008. Process maps for plasma spraying of yttria-stabilized zirconia: An integrated approach to design, optimization and reliability. *Materials Science and Engineering A*, 497, 239-253.
- Vehlow, J., n.a.. Die Entwicklung der Abfallwirtschaft. <https://www.itad.de/information/geschichte>, (last access 03.04.2016).
- Wagner, C., 1956. Oxidation of Alloys Involving Noble Metals. *Journal of the Electrochemical Society*, 103, 571-580.

- Wagner, C., 1958. Passivity during the Oxidation of Silicon at Elevated Temperatures. *Journal of Applied Physics*, 29, 1295-1297.
- Wang, N., Zhou, C., Gong, S. & Xu, H., 2007. Heat treatment of nanostructured thermal barrier coating. *Ceramics International*, 33, 1075-1081.
- Warnecke, R., 2003. Korrosion unter Berücksichtigung von Strömungsgeschwindigkeit und Reaktionsenthalpie. In: M. Born, Hrsg. *Rauchgasseitige Dampferzeugerkorrosion*. Freiberg: Saxonia Verlag, 57-78.
- Warnecke, R., 2014. Fünfzig Jahre und kein bisschen weise - Korrosion und Verfahrenstechnik in thermischen Abfallbehandlungsanlagen. In: K. J. Thomé-Kozmiesky & M. Beckmann, Hrsg. *Energie aus Abfall*. Neuruppin: TK Verlag, 441.
- Wöllmer, S., Förg, A., Schuster, S. & Masset, P. J., 2015. Solvothermal Modified Layers against High Temperature Corrosion. *Materials Science Forum*, 825-826, 621-627.
- Xu, Z., He, L., Mu, R., Huang, G. & Cao, X., 2010. Hot corrosion behavior of rare earth zirconates and yttria partially stabilized zirconia thermal barrier coatings. *Surface and Coatings Technology*, 204, 3652-3661.
- Ye, Y., 2016. Modification of thermally sprayed ceramic oxide coatings by chemical densification processing, doctoral thesis, LMU Munich.
- Yoshimura, M., Hiuga, T. & Somiya, S., 1986. Dissolution and Reaction of Yttria-Stabilized Zirconia Single Crystals in Hydrothermal Solutions. *Journal of the American Ceramic Society*, 69, 583-584.
- Zyuzin, D. A., Cherepanova, S. V., Moroz, E. M., Burgina, E. B., Sadykov, V. A., Kostrovskii, V. G. & Matyshak, V. A., 2006. X-ray, Raman and FTIRS studies of the microstructural evolution of zirconia particles caused by the thermal treatment. *Journal of Solid State Chemistry*, 179, 2965-2971.

Figures

Fig. 1-1: Schematic layout of a WTE plant.	7
Fig. 1-2: Extended Flingern's corrosion diagram.	8
Fig. 1-3: Schematic layout of a waste-to-energy plant.	9
Fig. 1-4: Sketch of the active oxidation process on the surface of oxidized metal substrates.	11
Fig. 1-5: Phase stability diagrams for nickel, iron and chromium.	12
Fig. 2-1: Thermodynamic phase stability diagram for the system $\text{Zr-O}_2\text{-Cl}_2$.	16
Fig. 2-2: E-pO ²⁻ - diagram showing the stability field of ZrO_2 .	17
Fig. 3-1: Sample layout for lab-scale experiments.	21
Fig. 3-2: Layout of a test probe for in-situ tests within a WTE plant.	22
Fig. 3-3: Schematic illustration of the old experimental setup.	26
Fig. 3-4: Schematic illustration of the new experimental setup.	26
Fig. 3-5: Uncooled test probe with deposits from the flue gas.	29
Fig. 4-1: Back-scattered electron (BSE) image of an untreated sample (TS-000).	35
Fig. 4-2: Element mapping of an untreated sample (TS-000).	35
Fig. 4-3: Element mapping of the transition zone between bond-coat and top-coat for chromium and oxygen of an untreated sample (TS-000).	36
Fig. 4-4: Photographs showing the samples treated for two (TS-005) and three (TS-003) days.	36
Fig. 4-5: Back-scattered electron (BSE) images of an untreated sample (TS-000).	39
Fig. 4-6: Qualitative element mappings from samples TS-004 (1 day), TS-005 (2 days) and TS-003 (3 days).	40
Fig. 4-7: BSE images of samples TS-023, TS-027 and TS-031.	42
Fig. 4-8: BSE images of samples TS-032, TS-051, TS-055 and TS-059.	43
Fig. 4-9: Element mappings for zinc, potassium, sulfur, zirconium, yttrium, aluminum, chromium, nickel, iron and oxygen (as available) of an untreated sample, TS-023 and TS-027.	44
Fig. 4-10: Element mappings for zinc, potassium, sulfur, zirconium, yttrium, aluminum, chromium, nickel, iron and oxygen (as available) of TS-031, TS-032 and TS-051.	45
Fig. 4-11: Element mappings for sodium, zinc, potassium, sulfur, zirconium, yttrium, aluminum, chromium, nickel, iron and oxygen (as available) of TS-055 and TS-059.	46
Fig. 4-12: Element mapping of the transition zone between bond coat and top coat for chromium and oxygen of a treated sample (TS-031).	47
Fig. 4-13: XRD analysis of the densified layer within the YSZ top-coat of sample TS-031.	49
Fig. 4-14: Diagram showing the zirconium versus sodium oxid content of whole rock analysis from sanidinities from the Laacher See volcano.	50
Fig. 4-15: Overview of the experiments with a combined gas phase and salt melt interaction.	53

Fig. 4-16: Element mappings for chromium, nickel and iron of TS-044, TS-045, TS-046.	54
Fig. 4-17: Element mappings for chromium, nickel and iron of TS-040, TS-041, TS-042.	55
Fig. 4-18: Profiles of the transition zones between top-coat / bond-coat and bond-coat / steel for chromium and nickel and bond-coat / steel for iron of TS-044, TS-045, TS-046.	56
Fig. 4-19: Profiles of the transition zones between top-coat / bond-coat and bond-coat / steel for chromium and nickel and bond-coat / steel for iron of TS-040, TS-041, TS-042.	57
Fig. 4-20: Profiles of the transition zones between top-coat / bond-coat and bond-coat / steel for chromium and nickel and bond-coat / steel for iron of TS-037, TS-038, TS-039.	58
Fig. 4-21: Phase stability diagrams for chromium with respect to partial pressures of chlorine (p_{Cl_2}) and oxygen (p_{O_2}) at temperatures of 500 °C and 700 °C.	60
Fig. 4-22: Schematic illustration of the proposed densification process for the ceramic top-coat.	62
Fig. 4-23: Graph showing the weight loss of the zirconia beads.	64
Fig. 4-24: BSE images showing (A) the attacked surface at the top and (B) the recrystallized surface on top of a previously attacked surface of a zirconia bead.	65
Fig. 4-25: Detailed view of the newly formed zirconia layer on the bead surface.	66
Fig. 4-26: Comparison of Raman spectroscopic surface analyses of untreated and dissolved (SE01) surfaces as well as the new grown zirconia shell (SE02).	67
Fig. 4-27: XRD analyses of the residual powder.	68
Fig. 4-28: FT-IR spectrum of the uncalcinated residual powder.	69
Fig. 4-29: ICP-OES analyses of residual salt melts.	70
Fig. 4-30: Section of the phase diagram of $KCl-K_2SO_4-ZnCl_2-ZnSO_4$.	70
Fig. 4-31: XRD analysis of the residual melt after three days under chlorine containing atmosphere at 600 °C.	71
Fig. 4-32: Schematic illustration of the evolution of the salt melt.	73
Fig. 5-1: Reflected light (VIS) and back-scattered electron (BSE) images of an uncooled test probe TP 1 (700 °C) and a cooled test probe TP 2.1 (450 °C).	76
Fig. 5-2: Back-scattered electron (BSE) image in combination with element mappings from the lee-side of the uncooled test probe.	77
Fig. 5-3: Condition of the coatings of the cooled test probes (TP 2.1, TP 2.2, TP 2.3) after 23 days within a WTE plant.	78
Fig. 5-4: Back-scattered electron (BSE) image in combination with element mappings from the lee-side of a cooled test probe (TP 2.1 - 450 °C for 23 days).	79

Tables

Tab. 3-1: Overview of the used materials for top-coat, bond-coat and steel substrate.	23
Tab. 3-2: Experimental conditions and porosity values of the YSZ top-coat for lab-scale experiments with steel cylinders, coated with a multilayer coating, under a defined gas-phase.	27
Tab. 3-3: Experimental conditions for lab-scale experiments with steel cylinders.	28
Tab. 3-4: Experimental conditions for the investigation of YSZ beads with a salt melt.	28
Tab. 3-5: Overview of the in-situ experiments (TP - test probe).	30
Tab. 4-1: Comparison of observations regarding the densification process between prior studies of Fehr and coworkers (2012) and Ye (2016) with results from this study.	38
Tab. 4-2: Comparison of TS-003 (old experimental setup) and TS-027 (new experimental setup).	41
Tab. 4-3: Overview of the experiments within the new experimental setup.	48
Tab. 4-4: Experimental conditions for the investigation of YSZ beads with a salt melt together with the percental mass loss of the YSZ beads.	64
Tab. 4-5: Chemical compositions of untreated zirconia beads and sample SE02, treated for two days in 20 mmol salt amount.	66
Tab. 5-1: Results of XRF analyses from surface deposits of an uncooled test probe.	77
Tab. 5-2: Summarized observations for the in-situ test probes.	80

Acknowledgment

This dissertation, of course, is not the product of one single persons work. In fact it is the result of teamwork. Various people thoughts, ideas, efforts and endurance led to a successful outcome. Most notably I thank Professor Dr. Soraya Heuss-Aßbichler and post mortem Professor Dr. Karl Thomas (Tommi) Fehr. Tommi gave me the opportunity to do my doctoral degree within the research project “TS-Protect”. He was like a walking mineralogical encyclopaedia and taught me to look for the smallest crystallites within a rock specimen – since the devil is in the details. Suddenly he passed away on March 18th, 2014, leaving a big gap – scientifically as well as humanly. With Soraya I found a new dissertation advisor. Thanks to her keen mind, profound mineralogical knowledge and big enthusiasm, the project got new impulse, leading to unexpected and enlightening results. Furthermore, I thank Professor Dr. Klaus G. Nickel and Dr. Christoph Berthold from the Department of Applied Mineralogy, University of Tübingen, Germany for critical questions and helpful advises. I am very grateful for their offer for a close cooperation and the possibility to use their analytical facilities.

Besides my supervisors, the most important team players are the project partners: Dr. Silke Wöllmer and Professor Dr. Patrick J. Masset from the Fraunhofer UMSICHT institute in Sulzbach-Rosenberg, Germany. Dr. Martin J. Murer from Firma Martin GmbH, Munich, Germany. Dr. Horst Hill from Deutsche Edelstahlwerke GmbH, Krefeld, Germany. Konrad Rieger from Zweckverband Müllverwertung Schwandorf, Schwandorf, Germany. Carsten Härtel from Rohrwerk Maxhütte GmbH, Sulzbach-Rosenberg, Germany. From the beginning on it was a fruitful and energetic cooperation. I appreciate a lot the unrestricted readiness to help and the insights to industrial processes.

For the possibility to perform my dissertation at the Department for Earth and Environmental Sciences, LMU Munich, Germany I thank Professor Dr. Donald Bruce Dingwell.

What would the last 3.5 years have been without good colleagues? Definitely not as successful and cheerful as without them. It was a great pleasure to cooperate with Donja Aßbichler, who is doing her doctoral degree in the same research project “TS-Protect”. Her blithe spirit and scientific input were a great contribution for the project. Many thanks to Dr. Judith Schwerin and Dr. Ulf Gattermann for helpful advises regarding XRD analyses, fruitful discussions and fresh coffee all around the clock. In particular I want to thank Judith for her permanent and selflessly support. Professor Dr. Peter Gille, Dr. Melanie John, Dr. Amanda Günther, Alexandra Huber, Dr. Rupert Hochleitner and Dr. Melanie Kaliwoda are acknowledged for helpful discussions about my project and scientific discourses about diverse topics in the field of (applied) mineralogy, like the extraction of (heavy) metals from slags and / or waste water, analyses of meteorites, rare minerals I had never heard of before (like Hydroniumpharmacoalumite, Preisingerite or Phyllostungstite) as well as single crystals of various intermetallic phases.

For EPMA sample preparation I thank Hilger W. Lohringer. Even for the most challenging samples he finds a solution to prepare a useful and measureable specimen. In

the same way I thank André Schöttler-Himmel for his IT support and the team of the workshop in our department for realizing every wish, regarding my experimental setup.

Thanks to Saint-Gobain for providing me Zirmil Y beads free of charge. Especially Egbert Kleinert (SEPR Keramik GmbH & Co. KG, Saint-Gobain Zirpro) is gratefully acknowledged for his efforts.

For the financial support I thank the German Federal Ministry of Education and Research (BMBF).

Finally, I thank my parents Annerose and Bernd Müller. They were always a safe harbor and supported me whatever I was doing. Thank you!

Declaration of authorship

I hereby declare that the submitted thesis “Densification of zirconia-based anti-corrosion coatings for application in waste-to-energy plants” is my own unaided work. All direct or indirect sources used are acknowledged as references. This thesis was not previously presented to another examination board.

Dirk Müller

Munich, 14th September 2016